INFORMATION TO USERS

This was produced from a copy of a document sent to us for microfilming. While the most advanced technological means to photograph and reproduce this document have been used, the quality is heavily dependent upon the quality of the material submitted.

The following explanation of techniques is provided to help you understand markings or notations which may appear on this reproduction.

1. The sign or "target" for pages apparently lacking from the document photographed is "Missing Page(s)". If it was possible to obtain the missing page(s) or section, they are spliced into the film along with adjacent pages. This may have necessitated cutting through an image and duplicating adjacent pages to assure you of complete continuity.

2. When an image on the film is obliterated with a round black mark it is an indication that the film inspector noticed either blurred copy because of movement during exposure, or duplicate copy. Unless we meant to delete copyrighted materials that should not have been filmed, you will find a good image of the page in the adjacent frame.

3. When a map, drawing or chart, etc., is part of the material being photographed the photographer has followed a definite method in "sectioning" the material. It is customary to begin filming at the upper left hand corner of a large sheet and to continue from left to right in equal sections with small overlaps. If necessary, sectioning is continued again—beginning below the first row and continuing on until complete.

4. For any illustrations that cannot be reproduced satisfactorily by xerography, photographic prints can be purchased at additional cost and tipped into your xerographic copy. Requests can be made to our Dissertations Customer Services Department.

5. Some pages in any document may have indistinct print. In all cases we have filmed the best available copy.

University
Microfilms
International

300 N. ZEEB ROAD, ANN ARBOR, MI 48106
18 BEDFORD ROW, LONDON WC1R 4EJ, ENGLAND

LIGHT SCATTERING INVESTIGATIONS OF THE CENTRAL PEAK AT THE FERROELECTRIC TRANSITION IN KH_2PO_4

BY

MARC DAVID MERMELSTEIN

A dissertation submitted to the Graduate Faculty in Physics in partial fullment of the requirements for the degree of Doctor of Philosophy, The City University of New York.

1979

This manuscript has been read and accepted for the Graduate Faculty in Physics in satisfaction of the dissertation requirement for the degree of Doctor of Philosophy.

February 5, 1979
date

Chairman of Examining Committee

February 5, 1979
date

Executive Officer

Supervisory Committee

The City University of New York

DEDICATION

I dedicate this effort, and
the good that it represents,
to my mother and father with
love.

ACKNOWLEDGEMENTS

I express my gratitude to Professor Herman Cummins for providing me with the opportunity and guidance to complete this work. Furthermore, I thank all the members of the light scattering group for their friendship and assistance. In particular, I am grateful to Dr. N. Lagakos and Dr. R. Bruce for their assistance in the laboratory during the early portions of this research, Mr. S.C. Hung for his contributions to the experimental results presented here, and to Mrs. Francis Tritt for typing portions of this manuscript.

Moreover, I express a special affection to Fran Trottman whose friendship and understanding made this achievement possible.

TABLE OF CONTENTS

List of Tables

List of Illustrations

I. Introduction

Since the initial discovery in 1971 by Riste et. al.[1,2] of a central peak in the neutron scattering spectrum of $SrTiO_3$, an extensive amount of experimental and theoretical research has been devoted to understanding its origin. In our laboratory an unresolvable central peak in the light scattering spectrum of paraelectric KH_2PO_4 was observed by Lagakos and Cummins in 1974.[3,4] In the course of performing high resolution interferometric investigations of this central peak, a new more interesting dynamic central peak of width $\sim$ 50MHz was found in the ferroelectric phase within .1°K of the transition. We interpret this feature as arising from the coupling of the ferroelectric soft mode to the thermal diffusion mode in the ferroelectric (but not in the paraelectric) phase through the temperature dependence of the order parameter, the spontaneous polarization $P_3(T)$. A preliminary report of this observation was published in 1977.[5] Since that time, more extensive measurements of the temperature and electric field dependence of this dynamic central peak's intensity and linewidth were performed and are reported in this thesis. The temperature and electric field dependence of the intensity agree well with the predictions of thermodynamic fluctuation theory, while the linewidth measurements are in good agreement with the predictions of a coupled-mode analysis.

In the following chapter an experimental and theoretical review is given of the 'central peak phenomena' beginning with Riste's first observation. Chapter III sketches the theories of the ferroelectric phase transition occuring in KH_2PO_4. Computer simulations of the thermodynamic theory were performed to facilitate a comparison with the experimental results of this thesis. Expressions for the light scattering spectrum and

integrated intensities are constructed, in Chapter IV, from the classical theory. Chapter V discusses the experimental apparatus and considerations particular to these experiments. New experimental results and interpretations concerning the central peak in paraelectric KDP are presented in Chapter VI. The new experimental results characterising the dynamic central peak are given in Chapter VII. These include more extensive measurements of the dynamic central peak intensity and linewidth temperature dependence. It has been found that the application of an electric field permits the observation of the dynamic central peak in the paraelectric phase. A pronounced electric field effect in the intensity is reported. These experimental results are subsequently interpretted in the following chapter. Chapter IX is the concluding chapter which summarizes the results of this thesis work and points the way to future experimentation.

II. History of the Central Peak

An Experimental and Theoretical Review

A. Introduction

In this chapter I will present an experimental and theoretical review of the central peak phenomena. By central peak I mean a quasielastic or elastic component in the order parameter fluctuation spectrum that occurs in the vicinity of a structural phase transition. The strength of a central peak will diverge as the transition is approached and its linewidth will decrease. Furthermore, the presence of this low frequency structure will affect the response of the soft mode that drives the transition.

This experimental review is focused primarily on neutron scattering, light scattering, and magnetic resonance techniques. Other experimental techniques are briefly mentioned. The theoretical review is divided into central peaks originating from some intrinsic property of the crystal and those due to an extrinsic mechanism such as lattice defects. Intrinsic theories proceed from anharmonic phonon models, thermodynamic models, and explicit non-linear models. Extrinsic defect models can be classified either by their static/dynamic character or their symmetry breaking properties. A recent experimental and theoretical review of central peaks has been published by Blinc. [6]

B. Experimental Review

1) Neutron Scattering

In 1971 Riste et al. [1,2] reported the first observation of a central peak in the neutron scattering spectrum of $SrTiO_3$ in the region of the

105°K structural phase transition. This phase transition is driven by the soft optic mode at the zone-corner R point. Energy scans of inelastically scattered neutrons at three temperatures just above the transition temperature are shown in figure 1, reproduced from reference (1).

As T_c is approached from above, the soft mode phonon energy decreases, the phonon linewidth increases, and the intensity of the central peak increases. These scans demonstrate the existence of a central peak in addition to the soft mode associated with the structural transition. However, Riste et. al. were not able to establish an energy width to this spectral feature and thereby establish its dynamic nature (although they conjectured that they were observing a central peak associated with heat diffusion).

Subsequently, Shirane and Axe discovered a similar central peak in the neutron scattering spectrum of the high temperature superconductor Nb_3Sn. At the transition temperature T_m=45°K the crystal structure changes from cubic to a slightly distorted tetragonal form. This transition is characterized by softening of an accoustic shear mode. Shirane and Axe found that upon cooling towards the transition the central peak continued to grow in intensity while the soft acoustic side bands first softened and then saturated, remaining as distinct shoulders on the main central peak. The intensity of this central peak exhibited a strong wave vector dependence but no observable intrinsic energy width.

A phenomenological spectral density function characterizing central peak formation, proposed by Shirane and Axe, can be obtained by considering the frequency dependent part of the one-phonon neutron scattering cross section:

$$(1)\quad S(\omega) = \frac{k_B T}{\hbar\omega}\ \mathrm{Im}\left[\omega_o^2 - \omega^2 - i\omega\Gamma\right]^{-1}$$

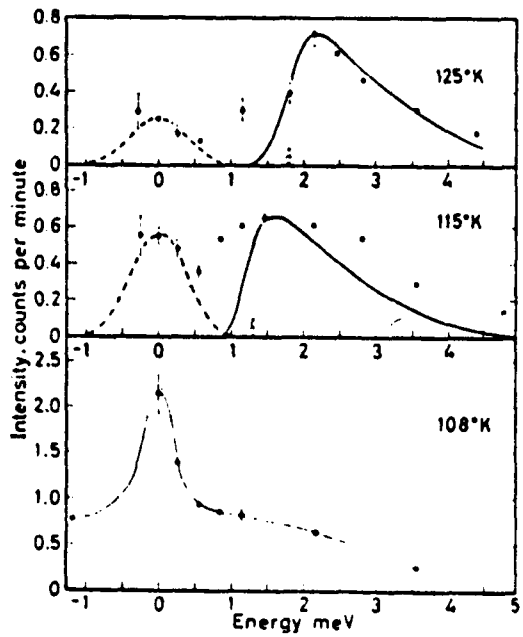

Energy scans at $q = 0$ for (1/2 1/2 3/2) for three different temperatures. At 125° and 115°K the full-drawn curves are calculated ones, normalized to observed intensity, assuming phonons of infinite lifetime and with energy denoted by arrows. The dashed curves indicate instrumental resolution as seen from incoherent background. At 108°K the curve drawn is only a guide to the eye.

fig. II-1

where ω_o is a temperature-dependent quasi-harmonic frequency and Γ is the phonon damping coefficient. Usually Γ is taken to be a frequency-independent constant. However, in general Γ will have a frequency dependence which reflects the changing density of excitations with which the soft phonon can interact. If the frequency dependence of Γ is assumed to be of the form:

$$(2) \quad \Gamma(\omega) = \Gamma_o + \delta^2(\tilde{\gamma} - i\omega)^{-1}$$

then insertion of the equation (2) into (1) yields the following spectral density function

$$(3) \quad S(\omega) = \frac{\frac{k_B T}{\hbar}\left[\Gamma_o + \frac{\delta^2\gamma}{\omega^2+\gamma^2}\right]}{\left(\omega_\infty^2 - \frac{\delta^2\gamma^2}{\omega^2+\delta^2} - \omega^2\right)^2 + \omega^2\left(\Gamma_o + \frac{\delta^2\gamma}{\omega^2+\gamma^2}\right)^2}$$

where $\omega_\infty^2 = \omega_o^2 + \delta^2$. $\int$ represents the coupling of the soft mode to some unspecified degree of freedom while ω_∞ and ω_o represent the high and low frequency response, respectively, of the soft mode. Equation (3) produces the three peaked lineshape characterizing central peak observations. This spectral density function will be discussed in more detail in the theoretical section of this review.

Shirane and Axe measured the ratio of the quasielastic neutron scattering cross section to the total scattering cross section as well as the soft mode frequency. This data, along with the consequences of the phenomenological spectral density function (3), lead to an experimental estimate for the coupling coefficient δ for Nb_3Sn, of $\delta = 0.14 \pm 0.04$meV. Knowing δ, equation (3) can predict the relation between the central peak

integrated intensity and the soft mode frequency ω_∞, which can be compared to experiment. The agreement with experiment was found to be quite satisfactory. An independent estimate of $\delta = (\omega_\infty^2 - \omega_o^2)^{\frac{1}{2}}$ was made. Values for ω_∞ were obtained from the neutron scattering experiment (high frequency probe) and values for ω_o were taken from ultrasonic measurements (low frequency probe). This estimate yielded δ= 0.012meV which compares quite well with the estimate from the neutron spectrum.

Although several predictions of this phenomenological theory compare quite well with experiment, the relaxation process that contributes a frequency dependence to the phonon damping has not been identified. Moreover, there is no dynamical evidence that such a process exists at all, i.e. there is no measurable energy width to this central peak.

More extensive neutron scattering studies were made of this central peak in $SrTiO_3$ and a similar feature was discovered in $KMnF_3$ by Shapiro et al. [8] Although these experiments were performed with higher energy resolution than that of previous neutron experiments, no energy width was detected. Topler et. al.[9] performed further neutron scattering experiments on $SrTiO_3$ with higher energy resolution than previous experiments and were unable to detect an energy width to this central peak. They measured an experimental upper limit to the energy width of 0.08 μeV.

The experiments on Nb_3Sn were extended by J. D. Axe and Shirane [10] in 1973. They interpretted their experiments in terms of the phenomenological theory which assumes an additional low-frequency relaxation mechanism for the soft acoustic phonon. They were again unable to detect an energy width to the central peak. It is of interest to note (with respect to this present work) that Axe and Shirane point out that for dis-

placive transformations, the coupling constant in the Rayleigh scattering cross section will be proportional to $(\frac{d\eta}{dT})^2$ where η is the appropriate order parameter for the transformation and could produce a central peak. However, such a coupling mechanism cannot account for a central peak in the high temperature phase where $\eta = 0$. Furthermore, it is pointed out that because no energy width to the central peak has been detected it is worthwhile to consider possible static mechanisms to explain the presence of a highly temperature dependent, unresolvable central component in the neutron scattering spectrum. Axe and Shirane proposed a specific static defect mechanism that will be discussed in the theoretical section.

Neutron scattering measurements in the vicinity of the ferroelectric transition (as well as far into the ferroelectric phase) of Pb_4Ge_3O (lead germanate) were performed by Cowley et. al. [11] They observed, near T_c, a broad overdamped soft mode and a central peak whose energy width corresponded to their instrumental resolution of 0.11 meV. Both of these features are little affected by electric fields up to 3300 v/cm. In addition to the soft mode and the central peak appearing near the transition, there is a quasielastic component far below T_c which increases in intensity roughly as $T_c - T$ and which is largely suppressed by an applied electric field. Cowley et. al. propose that this feature is associated with the static domain structure and that the central peak, whose intensity peaks near T_c, is caused by dynamic domain motion.

As a follow-up on the suggestion by Axe and Shirane [10] that this quasielastic feature may be due to defect-induced state strain fields (and a later refinement of this proposal by Halperin and Varma [12]), Hastings et. al. [13] performed a neutron scattering experiment on a series of $SrTiO_3$

crystals with known defect concentrations. They found a systematic enhancement of the central peak intensity with increasing defect concentrations. Furthermore they found T_c to decrease with increasing defect concentration, in agreement with the frozen defect model of Halperin and Varma. Hastings et al. proposed that defects can enhance the observed central peak occuring near a structural phase transition. However, it is pointed out that these results do not demonstrate that the central peak results solely from defect mechanisms.

In summary, the neutron scattering work has been successful in detecting central peaks in a number of materials undergoing structural phase transitions, suggesting the presence of a quasielectric or elastic structure in the order parameter fluctuation spectrum. No neutron scattering experiment has been able to establish an energy linewidth to the central peak and thereby provide crucial evidence for dynamic central peak formation. Light scattering is an experimental technique that provides greater resolution for the detection of a dynamic central peak and will be discussed below.

2) Light Scattering Investigations

The first observation of central peak development in a light scattering experiment was reported in 1971 by Steigmeir et. al. [14] Raman measurements were made of soft ferroelectric mode near the ferroelectric phase transition of SbSI. It was found that close to the Curie point, in the ferroelectric phase, a broad feature developed centered at the zero frequency shift, in the Raman spectrum, whose intensity increased approximately as $(T_c - T)^{-4/3}$. Steigmeier et al. do not believe that this intense

scattering results from domain wall scattering since the domain size dimensions for needle-like SbSI crystals is larger than the incident laser beam diameter. Steigmeier et al. suggested that this feature may be due to critical scattering of the Rayleigh peak.

In 1973 Steigmeier et al. [15,16] measured the temperature and angular dependence of the total scattered light intensity near the structural phase transition of $SrTiO_3$. The crystals used in these experiments were carefully annealed. They observed a drastic increase in the total scattered light intensity as the transition temperature was approached from above and below. Measurements were made for three scattering angles (3, 90 and 177 degrees) and were found to obey an Ornstein-Zernike-like expression. They interpretted their results as critical opalescence associated with dynamic fluctuations of the order parameter in the vicinity of the transition temperature. Steigmeier et al. proposed that the light scattering arises from direct optical coupling to phonon density fluctuations as opposed to indirect coupling via the soft mode phonon as discussed in the phenomenological theory for central peak development associated with the neutron work. No linewidth was reported.

Investigations by Lyons and Fleury [17,18] revealed a singular <u>dynamic</u> central peak in the depolarized light scattering spectrum of $SrTiO_3$. This feature exhibits a FWHM of ~20 GHz and is visible only very close to the structural transition. They interpret this dynamic central peak to result from the interaction between the T.A. phonon and the soft E_g phonon that is coupled to some unspecified relaxing degree of freedom. Lyons and Fleury [19] also reported the detection of two non-singular

resolvable quasielastic features in the light scattering spectrum of $KTaO_3$ as $SrTiO_3$ which they identify as entropy fluctuations and two-phonon processes. However these features can be expected in all substances and bear no intimate relation to the structural transition.

Lockwood et al.[20] reported Brillouin, Raman, and photon correlation light scattering investigations of a central peak in the vicinity of the 452°K ferroelectric phase transition in lead germanate. They observed a central peak whose intensity increases as T_c is approached from below and which falls off rapidly in the high temperature phase. Their measurements indicate no intrinsic linewidth in the spectral regions of 13 GHz to 80 MHz and 10 MHz to 10 Hz. Furthermore, they made a visual observation of the laser scattering column and observed the speckle pattern characteristic of static scattering. Therefore, it appears likely that the anomalous central peak intensity is static in origin and may arise from localized defects in the crystal. Lockwood et al. considered the defect-induced spatial variations in the local transition temperature as the cause of the elastic scattering. The local transition temperature can be expressed as the sum of a mean value plus a spatially dependent fluctuation.

$$(4) \quad T_c(\underline{r}) = \overline{T}_c + \delta T_c(\underline{r})$$

It is assumed that the electronic polarizability depends upon temperature in the following manner:

$$(5) \quad \alpha = \alpha_0 + \alpha_1 (T_c - T)^{1/2} \qquad T < T_c$$

The scattered intensity is then expressed as

$$(6) \qquad I_q \sim \int d^3r\, e^{i\underset{\sim}{q}\cdot\underset{\sim}{r}} \langle \alpha[T_c(\underset{\sim}{r})-T]\alpha[T_c(0)-T]\rangle$$

so that the temperature dependence of the anomalous static central peak is

$$(7) \qquad I \sim \frac{\alpha_1^2 \langle \delta T(r)\delta T(0)\rangle}{4(T_c-T)}$$

This intensity temperature dependence of $(T_c - T)^{-1}$ agrees well with their experimental results. This mechanism is discussed by Halperin and Varma [12] as scattering from local variations in the density of impurities and differs from the $(T_c - T)^{-2}$ temperature dependence of central peak scattering from static strains associated with frozen defects. [10,12]

Fleury and Lyons [21] measured a singular dynamic central peak associated with the ferroelectric transition in lead germanate. By using a molecular iodine cell, they were able to remove the strong static central peak measured by Lockwood et al.[14] and examined the dynamic spectrum. Their Raman and Brillouin measurements traced the evolution of the ferroelectric soft mode and the singular dynamic central peak in the vicinity of the phase transition. Far from T_c, in the ferroelectric phase, the soft mode is underdamped and decreases in frequency approximately as $\omega_s^2 \sim (T_o - T)$ while broadening slightly. Between 395 and 440°K, the soft mode is overdamped and the decrease of its half-width $\Gamma = \frac{\omega_s^2}{\gamma}$ is consistent with $(T_c - T)$. Within 10°K of T_c, the soft mode line shape ceases to change (FWHM$\sim$4.6cm^{-1}) and its intensity begins to decrease. At the same time a new depolarized dynamic central peak emerges with a FWHM of about $\sim$7.8GHz. The temperature at which this feature's intensity peaks is taken

to be the transition temperature. Above T_c the dynamic central peak intensity decreases rapidly so that by T_c + 5°K it is no longer detectable. Fleury and Lyons were unable to conclusively establish the microscropic origin of this dynamic central peak.

Measurements of the dynamic central peak in lead germanate were extended by Lyons and Fleury [22] and reported in a subsequent paper.

In 1974 Lagakos and Cummins [3] reported the observation of central peak development in the Brillouin spectra of the Xy shear mode and B_2 optic modes in KDP close to the ferroelectric transition. As the transition temperature is approached from above, the Brillouin spectra revealed the softening of the Xy shear mode Brillouin components and the development of a central peak whose intensity increases by more than 30 times within 1°K of the transition. This central peak exhibited no intrinsic linewidth. The Brillouin spectra were fit to a three coupled mode model consisting of the ferroelectric soft mode, a second optic phonon of the same symmetry as the soft mode, and the Xy shear mode. Included in the response function for the soft mode was a relaxing self energy of the form $\delta^2(1-i\omega\tau)^{-1}$ where $\delta = \alpha T$. This relaxing self energy was first suggested by Cowley and represents anharmonic coupling of the soft mode to pairs of acoustic phonons. This response function is of the same form as the phenomenological theory used in the neutron work. The coupled mode analysis for coordinated Raman and Brillouin experiments yields a lower bound for the relaxation time τ of 10^{-9} seconds while the coupling constant was estimated to be $\delta \sim 1 cm^{-1}$ at T_c. Lagakos and Cummins point out that because no width was determined for this central peak, it may be in fact due to static strain fields as proposed by Axe et al. [10]

Subsequently, Durvasula and Gammon [24] showed that this central peak in paraelectric KDP exhibited speckle interference fringes. This sparkle pattern is characteristic of a static scattering mechanism. Because the scattered light is depolarized, as it is for the Xy shear mode, Durvasula and Gammon interpreted this feature as resulting from strain decorations of static defects. Recently, Courtens [25] showed that this static central peak can be essentially removed from the spectrum by annealing the crystal at 140°C for a period of 18 hours. This shows that the central peak appearing in the paraelectric phase is not an intrinsic property of the crystal and is associated with annealable lattice defects.

Previous to Courtens work, Yagi et al. [26] reported that the central peak in the light scattering spectrum of $KH_3(SeO_3)_2$ is suppressed by successive temperature cycling, thereby also identifying its origin with lattice defects. Furthermore, they observed [27] a sample dependence to the central peaks occuring in the deuterated crystals $KD_3(SeO_3)_2$, which may be associated with differing deuterium concentrations. However, the central peaks in $KD_3(SeO_3)_2$ were not suppressed by temperature cycling.

Light scattering experiments were thus successful in clearly resolving linewidths to the central peaks occuring in $SrTiO_3$ and $Pb_4Ge_3O_{11}$. Also there is evidence for a dynamic central peak in SbSI although no linewidth measurement has been reported. Unresolvable central peaks in KH_2PO_4 and $Pb_4Ge_3O_{11}$ have been established to be elastic scattering. These central peaks and those of $KH_3(SeO_3)$ and $KD_3(SeO_3)_2$ appear to be associated with some static defect mechanism.

3) Magnetic Resonance Investigations

Magnetic resonance techniques measure the time averaged local order parameter by observing the crystal field induced splittings of the resonance lines. The local soft mode dynamics are probed by lifetime effects in the spectrum and by the temperature dependence of the spin-lattice relaxation time. The local central peak is observed via the frequency dependence of the spin-lattice relaxation time. Electron paramagnetic resonance, nuclear paramagnetic resonance, and nuclear quadrupole resonance techniques have all been used to investigate the local, low frequency order parameter fluctuations. As early as 1967 Blinc et al. [28] observed in the EPR spectrum of the AsO_4^{4-} paramagnetic center in KH_2AsO_4 slow protonic reorientations occuring 100°K above the transition temperature. Muller et al. [29,30] report having measured a central peak linewidth of 60 MHz at 2°K above the transition in $SrTiO_3$. Dispersion of the proton spin-lattice relaxation times demonstrated the existence of a dynamic central peak in the paraelectric phase of KH_2PO_4 and $KH_3(SeO_3)_2$. [31,32] For both crystals, the central peak width determined by NMR is of the order of 10^5 - 10^6 Hz. [75] As quadrupole perturbed NMR studies of KH_2AsO_4, CsH_2AsO_4, and $RbH_2A_5O_4$ have revealed dynamic central peaks in the 10^3 - 10^5 Hz range. [33,34]

In 1976 Muller et al. [35] measured the EPR spectrum showing local ferroelectric ordering in Cr^{5+} doped KH_2PO_4 and KH_2AsO_4 and their deuterated isomorphs for temperatures well into the paraelectric phase. From their experimental results for the ferroelectric cluster lifetimes, Muller et al. deduce a central peak linewidth of less than 20MHz.

In a subsequent publication, Muller and Berlinger [36] identified the

symmetry of the electronic wave function associated with Cr^{5+} (3d) impurity in KH_2AsO_4 and KH_2PO_4. Symmetry allowed rotations of the electronic charge density in the hydrogen bonded tetrahedra couple to the nearest protons or deuterons in their double well potentials and break the local symmetry. Hence, they believe that this impurity acts as a Halperin-Varma relaxing defect cell. Muller and Berlinger show that this rotational relaxation time is an order of magnitude greater than that of the slow ferroelectric cluster dynamics identified independently in an earlier publication.

Blinc [37] has recently given an extensive review of magnetic resonance investigations of the local central peak.

4) Miscellaneous Experimental Techniques

Other experimental techniques that have been used to investigate the central peak phenomena are Mossbauer spectroscropy, [38,39,40,41] ultrasonic attenuation, [42,43] and dielectric dispersion. [44,45,46,47] Alexander and Gammon [43] calculated the frequency dispersion of the ultrasonic attenuation coefficient α for KDP. They included in their model a relaxation degree of freedom which couples to the ferroelectric soft mode and found that a relaxation time τ of 4 nanoseconds was consistent with the ultrasonic data, in the paraelectric phase, for α vs ω^2 reported by Garland and Novotny. [48] Tornberg and Lowdes [45] have made radio frequency dielectric measurements of KDP and CsDA in the 5-80 MHz range. They observed a strong dielectric loss in the paraelectric phase of CsDA and a pronounced Debye relaxation process in the ferroelectric phase of both materials. The dielectric data were fit to the complex dielectric constant:

$$(8) \quad \varepsilon(\omega) = \varepsilon'(\omega) + i\varepsilon''(\omega) = \varepsilon(\infty) + \frac{A}{1+i\omega\tau} .$$

In KDP the reciprocal relaxation time τ^{-1} was found to <u>increase</u> from ~20 to 30 MHz as the temperature is increased from $T \approx 0.8T_c$ to T_c. The amplitude of this relaxational component also increases but appears to level off close to the transition. A comparison of this dielectric data with the dynamic central peak observed in the light scattering spectrum of ferroelectric KDP by Mermelstein and Cummins [5] was subsequently made by Widom et al. [46] They suggest that the same physical process is responsible for both effects.

C. Theoretical Review

1) Intrinsic Theories

(a) Anharmonic Phonon Models

In 1970 Cowley [23] first showed that the soft mode response function for a piezoelectric ferroelectric crystal could yield a three peaked spectrum. The spectrum shows sidebands corresponding to the soft mode plus a third quasielastic central peak. A simplified picture of the mechanism proposed by Cowley that yields a central peak is discussed by Axe and Shirane. [10] Of interest is the spectral density function for scattering from the soft mode close to the transition temperature. Anharmonic perturbation theory yields the following expression for the spectrum:

$$(9) \quad S(q,\omega) = \frac{1}{\pi}\left[n(\omega)+1\right] Im\left[\Omega^2(q) + \Pi(q,\omega,T) - \omega^2\right]^{-1}$$

where $n(\omega) = (e^{\hbar\omega/k_BT} - 1)^{-1}$ is the phonon occupation number and $\Omega(q)$ is the wave vector dependent harmonic frequency. $\Pi(q,\omega,\tau)$ is the phonon

self energy resulting from the phonon interactions of the anharmonic crystal and contains real and imaginary contributions, which, in the simplified quasiharmonic approximation, can be written as:

$$(10) \quad \pi(q,\omega,T) = \Delta_0(q,T) - i\omega\Gamma_0(T)$$

$\Delta_0(q,T)$ renormalizes the harmonic frequency allowing for the temperature dependence of the quasiharmonic frequency while $\Gamma_0(T)$ introduces damping via phonon-phonon scattering. Cowley suggested that the self energy $\pi(q,\omega,T)$ in (9) may include a relaxational contribution to the real and imaginery parts so that $\Delta(\omega)$ and $\Gamma(\omega)$ will be of the form

$$(11a) \quad \Delta(\omega) = \Delta_0 - \delta^2\gamma^2(\omega^2+\gamma^2)^{-1}$$

$$(11b) \quad \Gamma(\omega) = \Gamma_0 + \delta^2\gamma(\omega^2+\gamma^2)^{-1}$$

Cowley points out that such a relaxation contribution may arise from the anharmonic interactions of the soft mode with the bath of thermal phonons as the crystal passes from the collision free regime ($\omega_{s.m.}\tau_{th.} >> 1$) to the collision dominated regime ($\omega_{sm}\tau_{th} << 1$) where ω_{sm} and τ_{th} are the soft mode frequency and the thermal phonon relaxation time respectively. The spectral density function resulting from the self-energy (11) is found to be (q dependence will be suppressed):

$$(12) \quad S(\omega) = \frac{k_B T}{\pi} \frac{\Gamma_0 + \dfrac{\delta^2\gamma}{\omega^2+\gamma^2}}{\left(\omega_\infty^2 - \dfrac{\delta^2\gamma^2}{\omega^2+\gamma^2} - \omega^2\right)^2 + \omega^2\left(\Gamma_0 + \dfrac{\delta^2\gamma}{\omega^2+\gamma^2}\right)^2}$$

where $$(13) \quad \omega_\infty^2 = \Omega^2 + \Delta$$

and (14) $$\omega_\infty^2 = \omega_0^2 + \delta^2$$

ω_∞ is the renormalized quasiharmonic frequency as measured by a high frequency probe and ω_0 is the renormalized quaisharmonic frequency measured by a low frequency probe.

Equation (12) with the appropriate choice of parameters, yields the three peaked spectral lineshape. In the limit $\omega_\infty^2 \gg \delta^2$ it shows three distinct peaks with sidebands at $\pm\omega_\infty$. However, as $\omega_0(T)$ approaches zero, $S(\omega)$ shows an increasing central peak intensity with phonon side bands that soften and eventually saturate at $\omega = \pm\omega_{\infty_0} = \pm\delta$.

The total integrated intensity of the three peaked spectrum $S(\omega)$:

(15) $$I_{tot} = \int d\omega\, S(\omega) = \frac{k_B T}{\omega_0^2(T)}$$

and is determined by the low frequency response ω_0^{-2}. For typical parameter values $\Gamma_0 \ll \frac{\delta^2}{\gamma}$ and $\omega_\infty \gg \gamma$, $S(\omega)$ can be conveniently divided into a central peak contribution and a phonon contribution:

(16) $$S(\omega)_{tot} = S(\omega)_{cen} + S(\omega)_{side}$$

where

(17) $$S(\omega)_{cen} = \frac{k_B T}{\hbar}\left(\frac{\delta^2}{\omega_0^2\omega_\infty^2}\right)\left(\frac{\gamma'}{\omega^2 + \gamma'^2}\right) \quad \text{and} \quad \gamma' = \left(\frac{\omega_0}{\omega_\infty}\right)^2 \gamma$$

determines the central peak linewidth. Note that the central peak linewidth contains the renormalization coefficient $\left(\frac{\omega_0}{\omega_\infty}\right)^2$.

The phonon side bands are given by:

$$S(\omega)_{side} = \frac{k_B T}{\hbar} \frac{\Gamma_0}{(\omega_\infty^2 - \omega^2)^2 + \omega^2 \Gamma_0^2} \quad (18)$$

The integegrated intensities for $S(\omega)_{cen}$ and $S(\omega)_{side}$ are:

$$I_{cen} = \frac{\delta^2}{\omega_0^2 \omega_\infty^2} \quad (19)$$

$$I_{side} = \frac{1}{\omega_\infty^2} \quad (20)$$

which obey the sum rule:

$$I_{tot} = I_{cen} + I_{side} \quad (21)$$

Hence the central peak, as originally proposed by Cowley, is intimately connected with the soft mode of a structural phase transition. The softening of the soft mode frequency $\omega_0(T)$ will cause the intensity of the central peak to increase dramatically and its linewidth to decrease as the transition temperature is approached. Furthermore, the temperature dependence of the high frequency response of the soft mode will now be modified according to (14) due to its interaction with the crystal's low frequency dynamical structure. In his 1970 paper Cowley proposed several extensions to this relaxing self energy model. One such extension was for the case of a pyroelectric crystal where the ferroelectric mode is able to couple to temperature fluctuations in the crystal. Cowley points out that such coupling would allow the detection of second sound though its effect on the dielectric response. These theories were subsequently expanded in later papers. [49,50]

With the discovery of a central peak in the neutron scattering spectrum of $SrTiO_3$ by Riste in 1971, several anharnomic phonon theories were evoked to explain the observed central peak. [51,52,53,54,55,70] However all these theories reduce to the same spectral density function (12) proposed by Cowley. Ohnari and Takada [56] have recently calculated the dynamic central peak spectral density function resulting from anharmonic coupling of the thermal diffusion mode to the soft mode which can occur both above and below the transition as well as for the case of linear coupling through the temperature dependence of the order parameter in the ferroelectric phase.

(b) Thermodynamic Models

From a thermodynamic approach, Feder [1,57] points out that a central diffusion mode may be expected in the order paramter fluctuation spectrum in the critical region of a second order phase transition. The ratio of the integrated intensities of the total spectrum and the soft mode doublet are given in terms of the isothermal and adiabatic susceptibilities $\chi_T(q)$ and $\chi_S(q)$:

$$\frac{I_{tot}}{I_{side}} = \frac{\chi_T(q)}{\chi_S(q)} \tag{22}$$

(for $q = 0$ this reduces to the Landau-Placzek ratio). He argues that whenever $\frac{\chi_T}{\chi_S} > 1$, the soft mode picture cannot fully describe the order parameter fluctuation spectrum and a quasielastic central peak can be expected. For $T<T_c$, χ_T is expected to be greater than χ_S due to the temperature dependence of the order parameter. (This case is similar to that discussed by Heller [58] for an antiferromagnet). Howevever, Feder

also argues that this will be true for $T>T_c$ although the average value of the order parameter is zero. As the transition temperature is approached, $\chi_T/\chi_s \rightarrow \infty$ and the diffusive central peak will dominate the order parameter fluctuation spectrum.

(c) Explicit Non-Linear Models

The microscopic models for central peak development discussed above followed a perturbation treatment of the lattice anharmonicity. An alternative approach is to include the anharmonicity without approximation. Analytic investigations of strongly anharmonic one-dimensional models for structural transitions were performed by Krumhansl and Scrieffer [59] and by Aubry. [60] These models reveal the existence of mobile clusters or microdomains of local order (solitons) in addition to the usual phonon excitations. Diffusive motion of these microdomains is expected to give rise to a central peak both above and below T_c. Furthermore molecular dynamics computer simulations were performed for one [61] and two [62] dimensional models. These computer simulations exhibit the cluster dynamics, expressed by the analytic non-linear calculations, that give rise to central peak formation near T_c.

Blinc [63,32] has extended the pseudo-spin Ising model in a transverse field for the soft mode in KDP. When non-linear effects are included he finds that in addition to the usual soft mode, representing fluctuations tranverse to the mean field, there is a longitudinal fluctuation of the order parameter spectrum that yields a central peak for $T>T_c$. He understands the presence of this longitudinal component to be equivalent to the exis-

tence of long lived microdomains of ferroelectric ordering which appear in the high temperature phase.

2) Extrinsic Theory

All of the above theories have considered the existence of a central peak to be an intrinsic property of the crystal. However, it is also possible that the narrow central peak may be due to lattice imperfections. This possibility was first suggested by Axe and Shirane [10,64] who proposed a specific static mechanism that would result in an infinitely narrow central peak. Axe and Shirane considered the formation of static strain fields induced by the presence of point defects in an otherwise homogeneous impurity free crystal. Neighboring atoms will suffer a displacement, due to the point defects, which can be viewed as a linear response to a force field $\underset{\sim}{F}(\underset{\sim}{r})$ originating from the defect. It is convenient to Fourier transform the resulting displacements and express them in terms of a linear combination of phonon modes with wave vector q and branch index j. The amplitude of this impurity induced phonon distortion $\langle Q_{j,q} \rangle_{s.i.}$ (s.i. = static impurity) is expressed in the harmonic approximation by

$$\langle Q_{j,q} \rangle_{s.i.} = \frac{F_{q,j}}{\omega^2_{j,q}} \tag{23}$$

where $F_{q,j}$ is the projection of $\underset{\sim}{F}(\underset{\sim}{r})$ upon the phonon eigenvector $\hat{e}(q,j)$. The intensity of this static scattering can be calcualted from the corresponding expression for the integrated phonon scattering under the same conditions by simply replacing $\langle Q^2_{q,j} \rangle_{\text{thermal}}$ by $\langle Q^2_{q,j} \rangle_{s.i.}$ so that

$$(24) \qquad I^{s.i.}_{q,j}(Q) \sim |\langle Q \rangle_{q,j}|^2 = \frac{|F_{q,j}|^2}{\omega^4_{q,j}}$$

If the impurities are of the proper symmetry so that they are able to linearly couple to the soft mode (j = soft mode) then the above relation predicts a central peak, of zero width, whose intensity will diverge as $\omega^{-4}_{q,s.m}(T)$.

Levanyak et al. [65] considered the intensity of light scattered by localized defects in the vicinity of a second order phase transition. By investigating the defect-induced change in the free energy of the crystal, they find that defect induced distortions of the same symmetry as the order parameter (linear coupling) will scatter light according to $I \sim |T-T_c|^{-1}$ in the region of validity of the Landau theory. This relation is determined by the growth of the distorted volume surrounding the defect. As the characteristic length of this volume surrounding the defect (which is related to the correlation length) approaches the mean defect spacing, the intensity of the central peak is expected to saturate. Levanyuk et al. estimate that, for reasonable defect concentrations, this maximum intensity can greatly exceed that of scattering from non-critical thermal fluctuations. Defects that couple quadratically to the order parameter are expected to produce only a jump in the scattered intensity at the transition point.

Halperin and Varma [12] replaced the localized defect as discussed by Axe et al. and Levanyuk et al., by a uniform distribution of defects throughout the lattic (effective crystal approximation). The unit cell of such a lattice may suffer a static distortion that breaks the symmetry of the high temperature phase in which case the resultant (frozen defect) model is identical to that proposed by Axe et al. However, Halperin and

Varma also introduced the possibility that the distortion of the defect cell may hop back and forth between positions that break the symmetry in opposite senses: the 'relaxing defect cell'. Such a mechanism would introduce a linewidth to the central peak determined by the characteristic time of this symmetry breaking reversal. Furthermore, Halperin and Varma point out that in the low temperature phase, local variations in the density of defects will produce local variations in the transition temperature which may also induce additional elastic scattering.

Schmidt and Schwabl [66,67] and Hock and Thomas [68] have shown that defects can raise the local transition temperature T_c^{loc} allowing the condensation of a local soft mode that will break the local symmetry in the high temperature phase. The first authors considered linear coupling between the defect and the local soft mode while the later authors considered quadratic coupling. Quadratic coupling includes the case where the defect does not break the local symmetry in the manner of the soft mode as well as the case where the defect induced broken symmetry fluctuates rapidly compared to the soft mode fluctuations and thereby produces no net distortion. E. Courtens [69] suggested that the naturally occuring presence of deuterium impurities may be an example of such a 'soft impurity' and produce the central peak observed in paraelectric KDP. Although Courtens was able to thereby account for the temperature dependence of the static central peak intensity, subsequent experiments failed to show any correlation between defect concentration and central peak strength. [25]

III. Theory of the Ferroelectric Phase Transition in KDP

A. Introduction

In the first half of this chapter I will give a very cursory theoretical review of the ferroelectric phase transition occuring in KH_2PO_4. This discussion is by no means complete. It is offered to provide some feeling for the microscopic models evoked to characterize the properties of KDP. A more extensive discussion of this material can be found in Ph.D. thesis of Nick Lagakos. [4] The second half of this chapter considers the phenomenological free energy theory of the phase transition due to Landau [71] and Devonshire. [72] A particular choice of the free energy due to Benepe and Reese [73] will be pursued in some detail. In particular, several theoretical consequences of the free energy, which are of interest to the experimental results of this thesis, will be presented.

B. Structural Characteristics

At room temperature KDP exhibits tetragonal structure of symmetry group D_{2d}. At approximately 122°K KDP spontaneously distorts to the orthorhombic structure of symmetry group C_{2V}. This distortion is accompanied by the development of spontaneous polarization along the crystallographic c axis. The spontaneous polarization, P_s, is the order parameter for the transition. At atmospheric pressure P_s rises discontinously at the transition temperature T_c, characteristic of a first order phase transition.

The room temperature atomic structure [74] of KDP is shown in Figure 1. [75] Each phosphorous atom is surrounded by four oxygens at the corners of a tetrahedron forming a $(PO_4)^{3-}$ group. The crystal consists of chains,

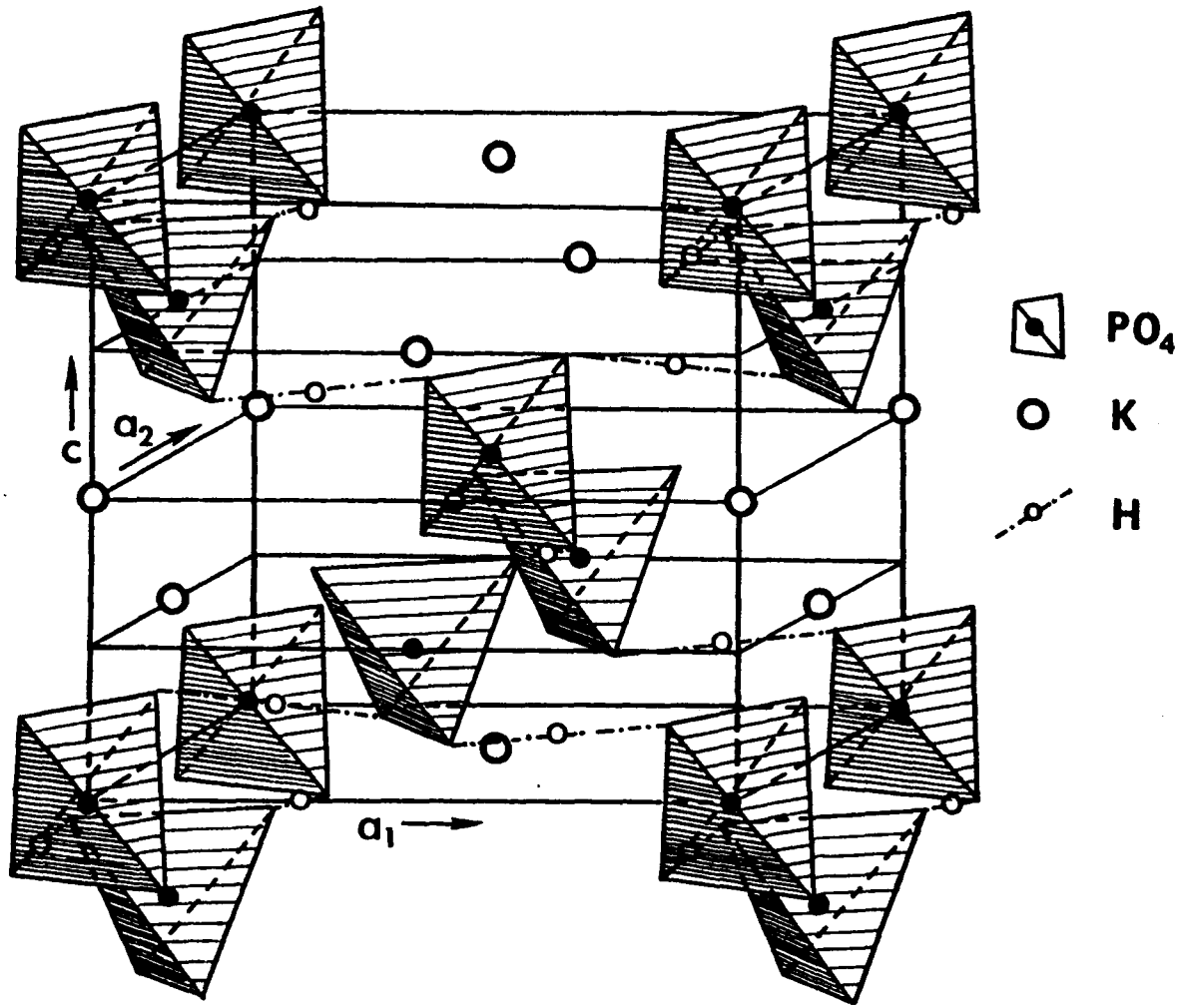

fig. III-1

along the c direction of alternating K^+ ions and $(PO_4)^{3-}$ ions. Adjacent chains are displaced along the c axis by c/4 and are linked by hydrogen bonds connecting the oxygen atoms at the top of a $(PO_4)^{3-}$ group to the oxygens at the bottom of a neighboring $(PO_4)^{3-}$ group. Each hydrogen bond lies very nearly perpendicular the c axis and there are four bonds for each PO_4 group. In the high temperature phase, the expectation value of the hydrogen's position lies at the center of the hydrogen bond between the two oxygens. However in passing through the transition, the hydrogens become ordered closer to one of the two oxygens. The framework of the oxygens remains essentially unchanged and the potassium and phosphorous atoms suffer a small displacement along the c axis in opposite directions. Since the hydrogen bonds are only about 0.5° out of parallelism with the [001] plane, the c component of the hydrogen shift can not account for P_s. Therefore, the spontaneous polarization is believed to arise from the displacement of the potassium and phosphorus ions.

C. Microscopic Models

1. Dipole Moments and Long Range Electrostatic Forces

In the vicinity of the transition temperature, several physical properties of the crystal exhibit anomalous behavior. However, all anomalies can be understood to result from the fundamental anomaly in the dielectric property of the clamped crystal. The static dielectric constant ε, measured along the c axis, exhibits a Curie-Weiss anomaly upon cooling towards the transition temperature:

$$(1) \qquad \varepsilon \simeq \frac{C}{T-T_o}$$

C is the Curie constant and T_o is the Curie temperature. Initial attempts to understand this dielectric anomaly considered the effect of the dipole moments associated with the atoms of the crystal. A simple relation, known as the Clausius-Mossotti equation, relates the dielectric constant ε to the atomic polarizabilities α and the number density N of dipole moments for a cubic crystal:

$$\varepsilon = \frac{1 + \frac{8\pi}{3} N\alpha}{1 - \frac{4\pi}{3} N\alpha} \tag{2}$$

If we choose a particular temperature dependence for N such that

$$1 - \frac{4\pi}{3} N\alpha = \frac{3}{C}(T - T_o) \tag{3}$$

then we can recover the Curie-Weiss law (1). However the comparison of this theory to the experimental results for KDP is very poor. Therefore, the sole inclusion of long-range electrostatic forces arising from the dipole moments cannot account for the observed ferroelectric properties of KPD.

2. Slater's Statistical Theory - Short Range Forces

Rather than consider the long-range forces due to the dipole moments throughout the lattic, Slater [76] considered the short-range forces associated with the hydrogen bonds and their effect upon the proton. On each hydrogen bond there are two equilibrium positions for the proton located symmetrically with respect to the center of the bond. Slater imposes two restrictions upon the proton's position:

a. There is one and only one proton on each bond.

b. There are only two protons near any one PO_4 group (the "ice rule")

These restrictions permit six possible configurations of the four protons around a PO_4 group. Slater then treats this problem utilizing the techniques of statistical mechanics. A counting of all possible proton configurations and their associated dipole moments, subject to the above restrictions, yields the thermodynamic probability function W from which the thermodynamic properties of the crystal can be determined. This treatment yields a phase transition at the transition temperature T_c:

$$(4) \qquad k_B T_c = \frac{e^s}{\ln 2}$$

and a dielectric anomaly:

$$(5) \qquad \varepsilon = \frac{N\mu^2}{k_B \ln 2} \frac{1}{T - T_c} \quad ,$$

e^s is an energy parameter and μ is the dipole moment associated with a particular proton configuration. This theory predicts a transition, at T_c, from the completely unpolarized state ($T>T_c$) to the completely polarized state for $T \leq T_c$, resembling the very rapid build-up of P_s observed in KDP. However, Slater's theory is unable to explain the drastic change (almost doubling) of the transition temperature in the deuterated crystal KD_2PO_4 (the isotope effect). This failure is viewed as the most serious objection to the theory. A review of the Slater theory, as modified by subsequent workers, is given by Silsbee et al. [77]

3. Proton Tunnelling - Isotope Effect

In 1959 Blinc was able to explain the large isotope effect by considering the quantum mechanical problem of a proton in the potential field

of the hydrogen bond. [78] He represented this field by a double well potential of unequal depths by:

$$(6) \quad V(x) = \begin{cases} \frac{1}{2} k (x+\ell)^2 & -\infty \leq x \leq b \\ \frac{1}{2} k (x-\ell)^2 + B & b < x \leq \infty \end{cases}$$

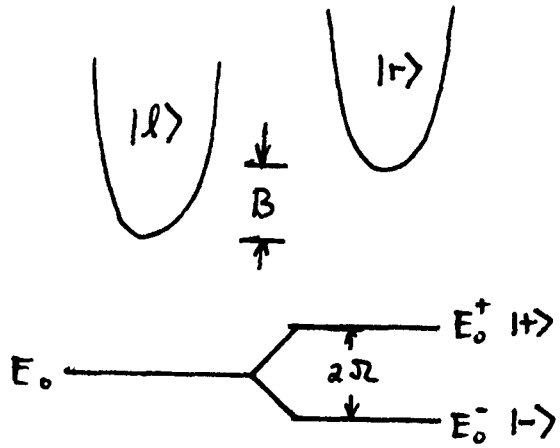

B is a measure of the interaction energy of the proton dipole moment with the local electric field resulting from the long-range dipolar forces. He also assumed that there is no short-range correlation between the positions of neighborhing protons. The quantum mechanical treatment of this problem shows that the energy eigenfunctions correspond to the proton tunnelling between the two wells ($1\pm\rangle = c_1|\ell\rangle \pm c_2|r\rangle$) and that the energy eigenvalue of a vibrational level will be split by an amount equal to the tunnelling integral 2Ω. The ferroelectric transition results from the competition between the long-range dipolar interactions B which tend to localize the proton in the lower well and the quantum mechanical tunnelling, which tends to localize the proton in either well with equal probability. The ferroelectric transition will occur when $B > 2\Omega$ where B and 2Ω are expressed in frequencies. Since the tunnelling frequency is mass dependent, Blinc was able to successfully acount for the pronounced isotope effect in the transition temperature.

4. Pseudospin Model

Short range interactions between adjacent tunnelling protons were subsequently included in the theory by P.B. de Gennes [79] and Brout, Muller, and Thomas. [80] The resultant collective excitations of the protons were discussed in terms of the pseudospin formalism where:

a. Each proton can occupy one of two states; $1\ell\rangle$ and $1r\rangle$ corresponding to the left and right minima of the double well potential, respectively, as introduced by Blinc.

b. Each proton is assigned a fictitious spin $\langle\hat{S}\rangle = \frac{1}{2}$ where $\langle\hat{S}_z\rangle = \frac{1}{2}$ corresponds to the proton in the left well and $\langle\hat{S}_z\rangle = -\frac{1}{2}$ corresponds to the proton in the right well.

c. The Hamiltonian for the pseudospin proton system is taken to be:

$$\hat{H} = \hat{H}_o + \hat{H}_1 \tag{7}$$

where

$$\hat{H}_o = 2\Omega \sum_i{}' \hat{S}_i^x \tag{7a}$$

$$\hat{H}_1 = \sum_{i,j}{}' J_{ij} \hat{S}_i^z \hat{S}_j^z \tag{7b}$$

Ω - tunnelling integral

J_{ij} - proton-proton interaction.

$\hat{H}_o$ represents the unperturbed Hamiltonian of a collection of non-interacting pseudospins (as disucssed by Blinc) which energetically favors the disordered symmetric state and $\hat{H}_1$ represents the proton interaction which energetically favors the ordered state. The Hamiltonian $\hat{H}$ can be schematically represented by:

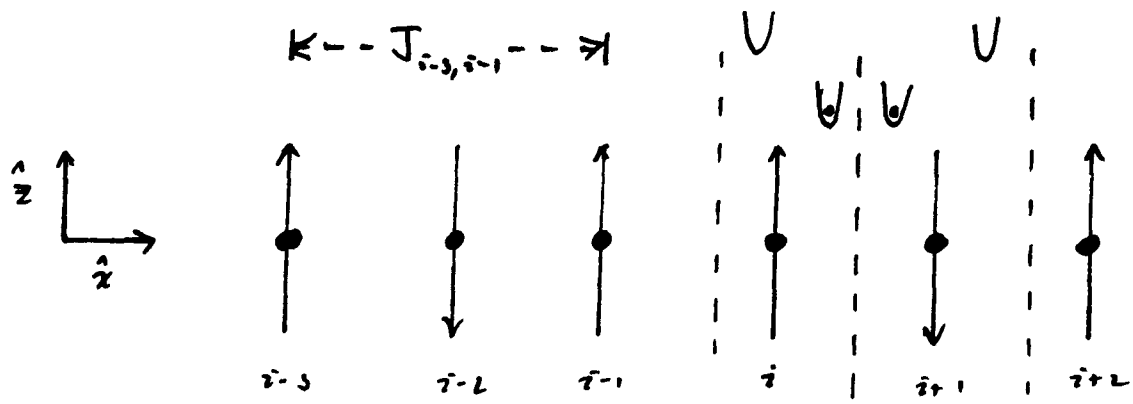

fig III-3

Interactions between the protons and other neighboring atoms as well as protonic vibrational states other than the ground state are neglected.

The expectation values of the spin operator $\langle \hat{S} \rangle$ are obtained in the Molecular Field Approximation (MFA). In particular, for the z components of spin

$$S_z = \frac{J_0 \langle \hat{S}_z \rangle}{M} \tanh \beta M \qquad (8)$$

where $$J_0 = \sum_{i,j}' J_{ij} \qquad \beta = \frac{1}{k_B T}$$

and M in the magnitude of the molecular field:

$$M = \left[4\Omega^2 + (2 J_0 \langle S^z \rangle)^2 \right]^{1/2}$$

Equation (8) yields a transition temperature T_c given by

$$1 = \frac{J_0}{\Omega} \tanh \beta_c M$$

and a temperature dependence for $\langle \hat{S}_z \rangle$ which is proportional to the order parameter P_s. The eigenfrequencies of the elementary excitations of this pseudo-spin system are calculated in the Random Phase Approximation (RPA). The eigenfrequencies are:

$$\omega_q^2 = 4\Omega (\Omega - J(q) \langle \hat{S}_x \rangle) + 4 J_0^2 \langle \hat{S}_z \rangle^2$$

This result predicts a soft mode behavior for the eigenfrequency of the q = 0 mode close to T_c.

$$\omega_o^2 \sim (T - T_c) \qquad T \rightarrow T_c^+$$

$$\omega_o^2 \sim 2 J_o \langle \hat{S}_z \rangle \qquad T < T_c$$

5. Proton - Phonon Coupling

In 1968 Kobayashi [81] proposed a dynamical model for the ferroelectric phase transition in KDP where the proton tunnelling mode (discussed above) couples strongly, through a Coulomb interaction, to the optical phonon corresponding to the vibration of the K^+ ion and the $(PO_4)^{3-}$ group along the c axis. As the proton system approaches its phase transition temperature, the frequency of one of the coupled modes, ω_-, is driven to zero. The ionic displacement for this soft ferroelectric mode is shown in Figure 4. It is the "freezing out" of this ferroelectric soft mode and the resultant displacement of the K^+ and $(PO_4)^{3-}$ ions which are responsible for the development of the spontaneous polarization along the c axis. This picture of the transition is closely related to the one proposed by Cochran. [82]

Kobayashi's coupled proton pseudospin and optical phonon model was extended by Takada et al. [83] to include the piezoelectric coupling to the transverse acoustic phonon (X_y shear mode). This coupling forces the softening of the C_{66} elastic constant (associated with the X_y shear mode) inducing the ferroelectric transition at a temperature greater than the transition temperature of the uncouple soft ferroelectric mode.

D. Thermodynamic Theory

1. Introduction

In a separate approach to the theory of the ferroelectric phase tran-

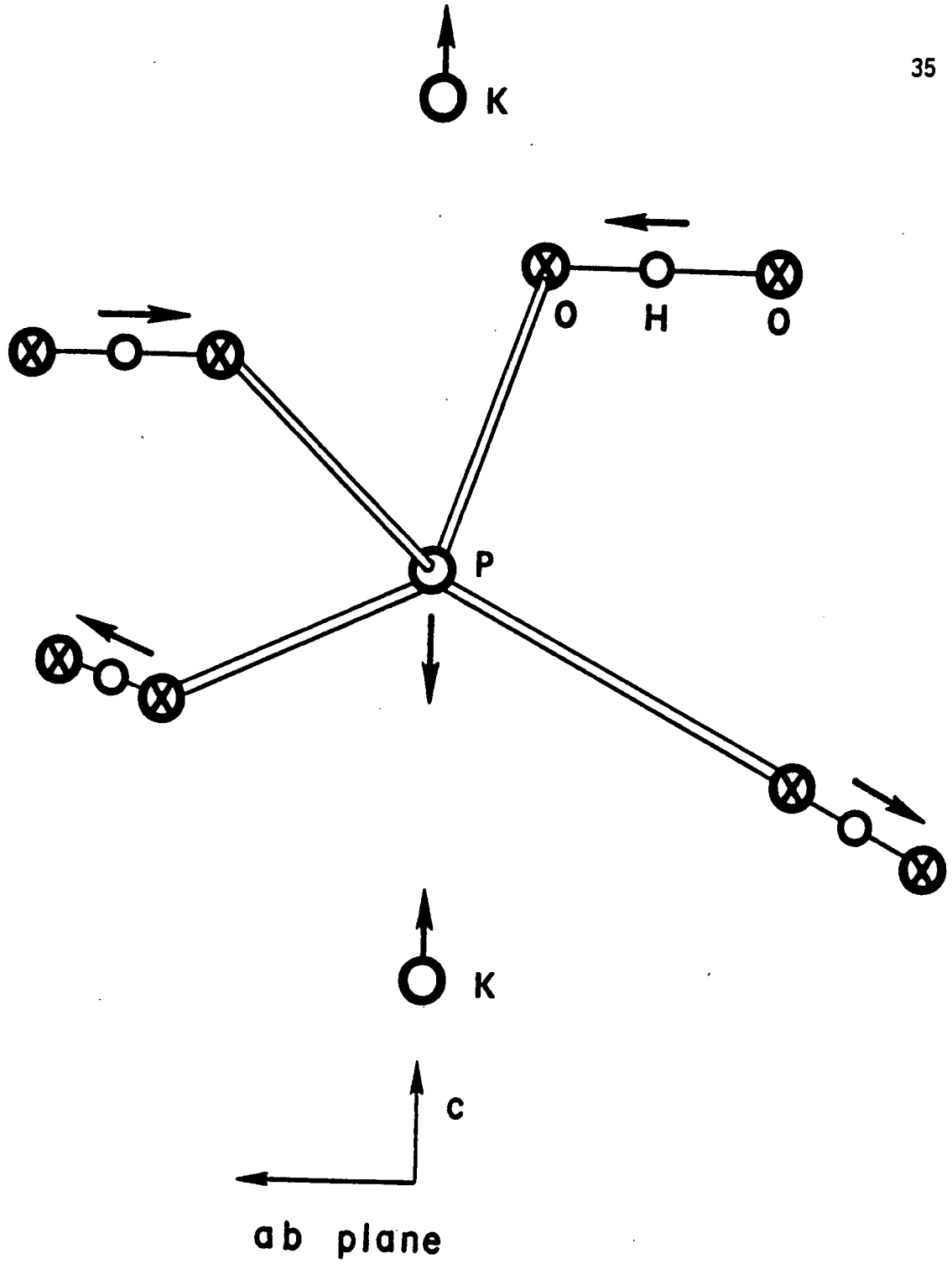

fig. III-4

sition, the Helmholtz free energy, A, for the crystal can be expanded phenomenologically in terms of the X_y shear strain x_6 and the polarization along the z axis P_z. [72,74] This expansion for KDP can be conveniently divided into the sum of three terms:

$$(9) \quad A(x_6, P_3) = A_0(P_3) + \left[\tfrac{1}{2} C_{66}^{P} x_6^2 - a_{36}^{T} x_6 P_3\right] + A_1(T)$$

$A_0(P_3)$ is the free energy for the polarization of a rigid lattice. The bracketed terms represents the contribution to A resulting from the piezo electric coupling of the polarization to the strain. $A_1(T)$ contains contributions to A due to lattice degrees of freedom that do not participate in the transition. Terms of odd powers in P are not permitted by symmetry.

$A_0(P_3)$, the pure polarization contribution to A, can be expressed as an expansion in P:

$$(10) \quad A_0 = \tfrac{1}{2}\alpha P^2 + \phi(P)$$

where

$$(11) \quad \phi(P) = \tfrac{1}{4} B P^4 + \tfrac{1}{6} C P^6 + \tfrac{1}{8} D P^8 + \cdots$$

$\phi(P)$ is known as the "saturation function" and contains higher order terms of P. α is assumed to have the following linear temperature dependence:

$$(12) \quad \alpha = \alpha_0 (T - T_0^X)$$

where T_0^X is the clamped Curie temperature. For the stree free crystal, the strain and polarization are related by: [74]

$$(13) \quad x_6 = \frac{a_{36}^{T}}{C_{66}^{P,T}} P_3$$

Hence, the Helmholtz free energy can be written as:

$$A(P) = \frac{1}{2}\alpha_0 (T - T_0^{\sigma}) P^2 + \phi(P) + A_1(T) \qquad (14)$$

where T_0^{σ} is the free Curie temperature and

$$T_0^{\sigma} - T_0^{x} = \frac{\alpha^2 T}{\alpha_0 C^{P,T}}$$

In the following discussions I will use a particular choice of the saturation function $\phi(P)$, due to Benepe-Reese. [73]

$$\phi(P) = \frac{1}{4} b P^4 + \frac{1}{8} \delta P^8 \qquad (15)$$

where,

$\alpha = 3.867 \times 10^{-3}\ K^{-1}$
$b = -4.4 \times 10^{-12}\ cm^4/esu^2$
$\delta = 2.96 \times 10^{-27}\ cm^{12}/esu^6$

2. Equilibrium Properties

(a) Transition Temperature

The Helmholtz free energy A, as determined by (6) and (7), is plotted in Figure (5) for several temperatures close to the free Curie temperature $T_0^{\sigma} = 122.000°K$. The equilibrium value of the polarization is that value which corresponds to an absolute minimum of the free energy. For above the transition that absolute minimum will occur at P = 0 corresponding to the paraelectric phase. As the transition is approached, side lobes will develope in the free energy, due to the negative quartic coefficient (see Figure 5), and descend with decreasing temperature. When the free energy at the local minimum about P = 0 and in the local minimum in the lobes are equal, the equilibrium value of the polarization will jump discontinuously

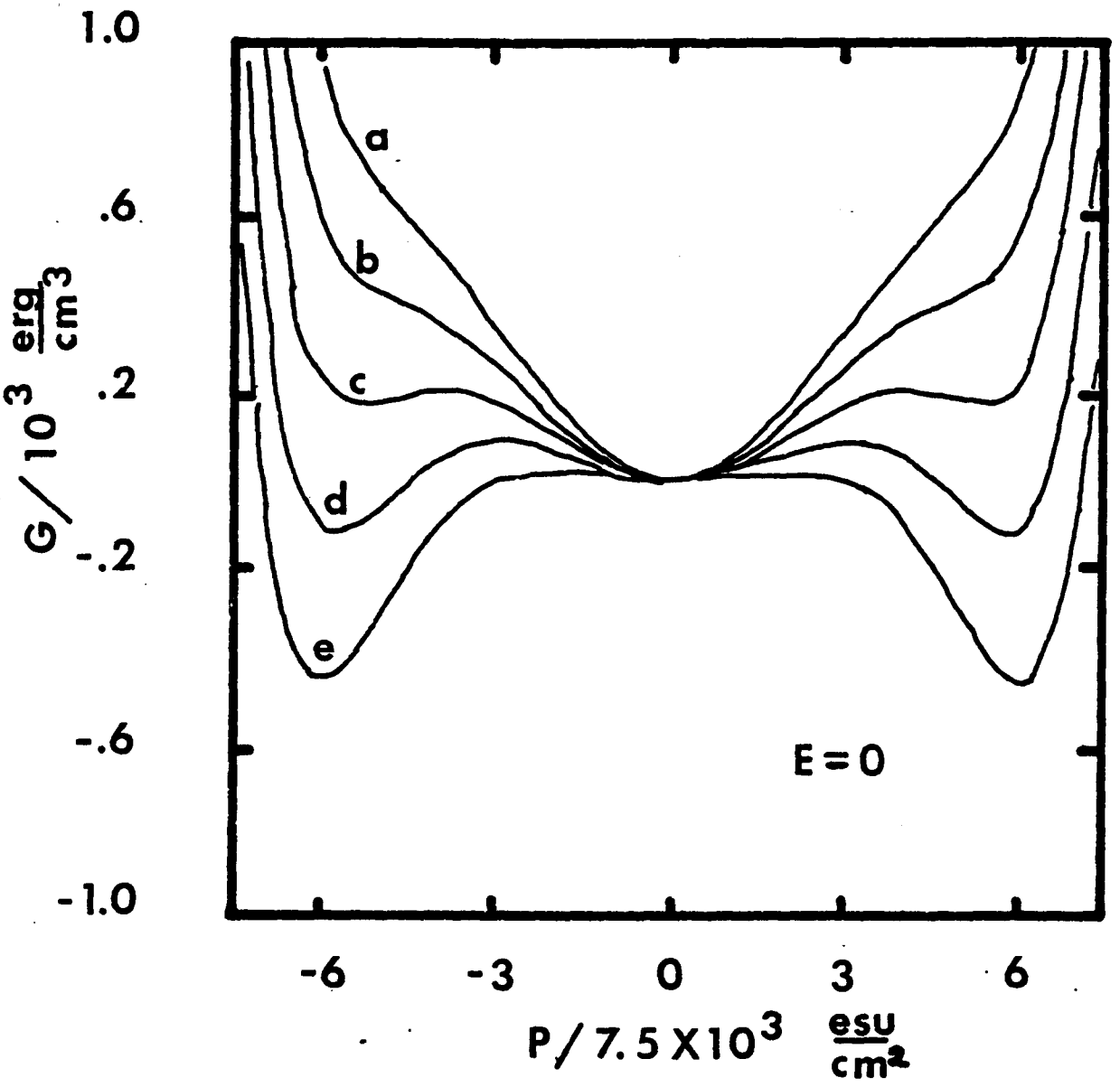

fig. III-5 Helmholtz free energy as function of polarization (with Benepe-Reese parameters) for several temperatures close to the transition temperature T_c. (a:122.025 ^{o}K, b:122.020^{o}K, c:122.015^{o}K,d:122.010 ^{o}K, and e:122.005 ^{o}K)

from $P = 0$ to $P = \pm P_o$. The temperature at which this occurs is the transition temperature T_c. P_o and T_c are found to be (for the Benepe-Reese free energy):

$$P_o^4 = -\frac{a}{3}\frac{b}{\delta} \tag{16}$$

$$T_c = T_o^\sigma + \frac{a}{3\alpha_o}\left(\frac{b^3}{6\delta}\right)^{1/2} \tag{17}$$

Substituting in the Benepe-Reese free energy parameters in (16) and (17), I find

$$P_o = 5.6 \times 10^3 \ \frac{esu}{cm^2} \tag{16'}$$

$$T_c = T_o^\sigma + 0.012 \ ^\circ K \tag{17'}$$

Inspection of Figure 5 indicates that the transition will occur between curves c and d, in agreement with eg. (17')

b. Spontaneous Polarization

A computer program was utilized to determine the absolute minimum (and therefore the polarization) of the free energy as a function of temperature and electric field. The development of spontaneous polarization, at zero electric field, is shown in Figure 6. This simulation yields:

$$P_o \simeq 5.6 \times 10^3 \ \frac{esu}{cm^2} \qquad T_c \simeq T_o^\sigma + 0.012 \ ^\circ K$$

in agreement with the analytic results.

c. Electric Field Effects

If an electric field E is applied along the z axes of the crystal,

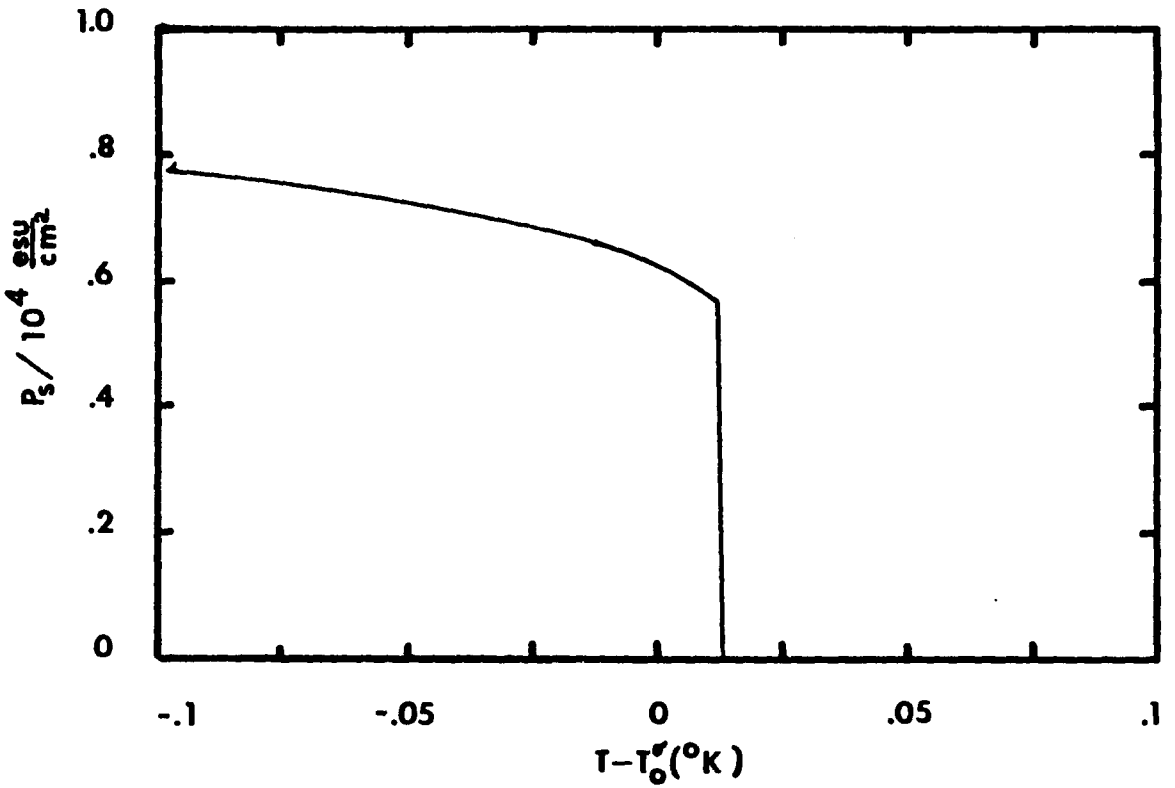

fig. III-6 Spontaneous Polarization

it is necessary to include a term -PE in the free energy A(P). The electric field is given by:

$$E = \frac{\partial A}{\partial P}$$

or

$$E = \alpha_o (T - T_o^{\sigma}) P + \frac{\partial \phi}{\partial P} \quad . \tag{18}$$

Equation (18) is the equation of state of the crystal.

The temperature dependence, as determined by this computer simulation, of the polarization for electric fields of E = 0, 50, 100, 200, 300, 500, 750 and 1000 $\frac{V}{cm}$ is illustrated in Figure 7.

Alternatively, the electric field dependence of the polarization for constant temperatures of ΔT = -0.025, 0, .025, .050, .075, and .100°K (with $\Delta T = T - T_o^{\sigma}$) are shown in Figure 8. Notice that in Figure 7 there is a discontinuous jump in P for electric fields below a critical field (to be defined below) and that in Figure 8 there is a discontinuous jump in P for temperatures below a critical temperature (also to be defined below) but above the transition temperature. Second harmonic generation and birefringence measurements [87] for KDP as well as polarization measurements in an applied electric field [88,89] support these predicted electric field effects.

d. Critical Point at Ambient Pressure

The free isothermal dielectric susceptibility is given by

$$\frac{4\pi}{\varepsilon^{\sigma,T}} = \left(\frac{\partial E}{\partial P}\right)_{\sigma,T}$$

Use of the B-R free energy yields (see Brody [74] for calculation of fluctu-

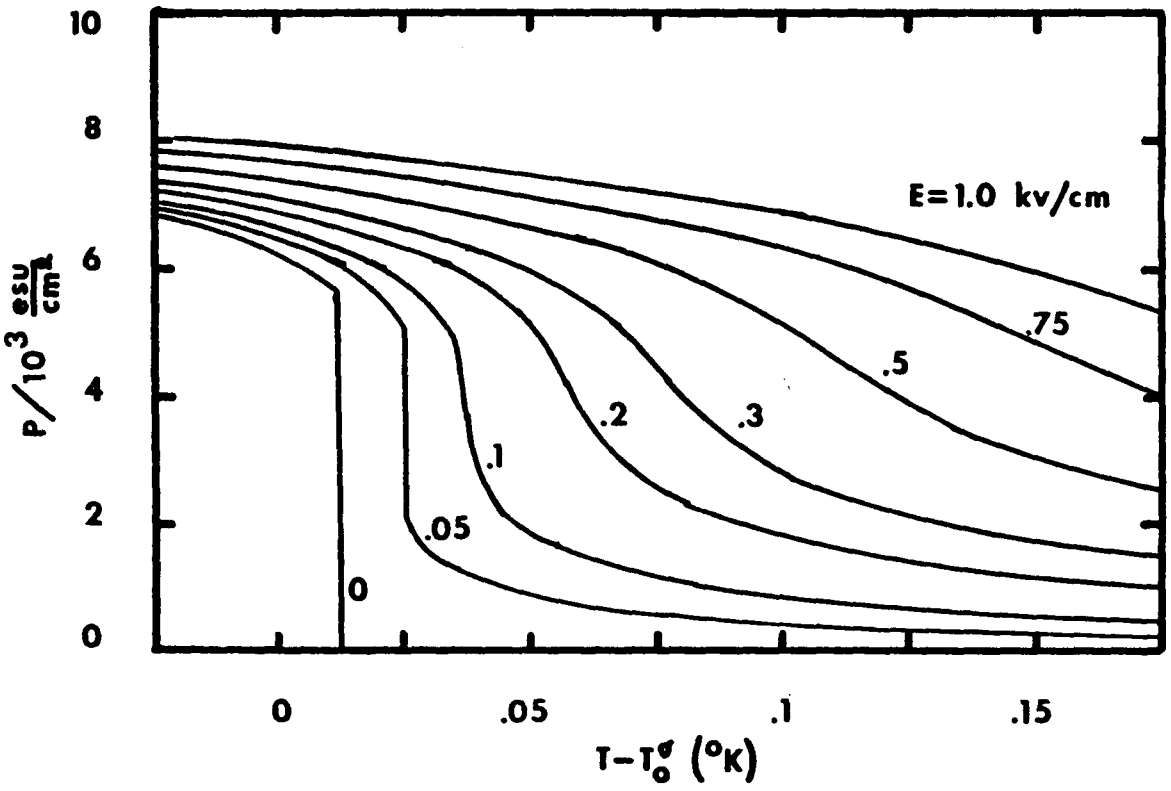

fig. III-7 Temperature Dependence of the Polarization at non-zero Electric Fields in the vicinity of the Transition Temperature T_c.

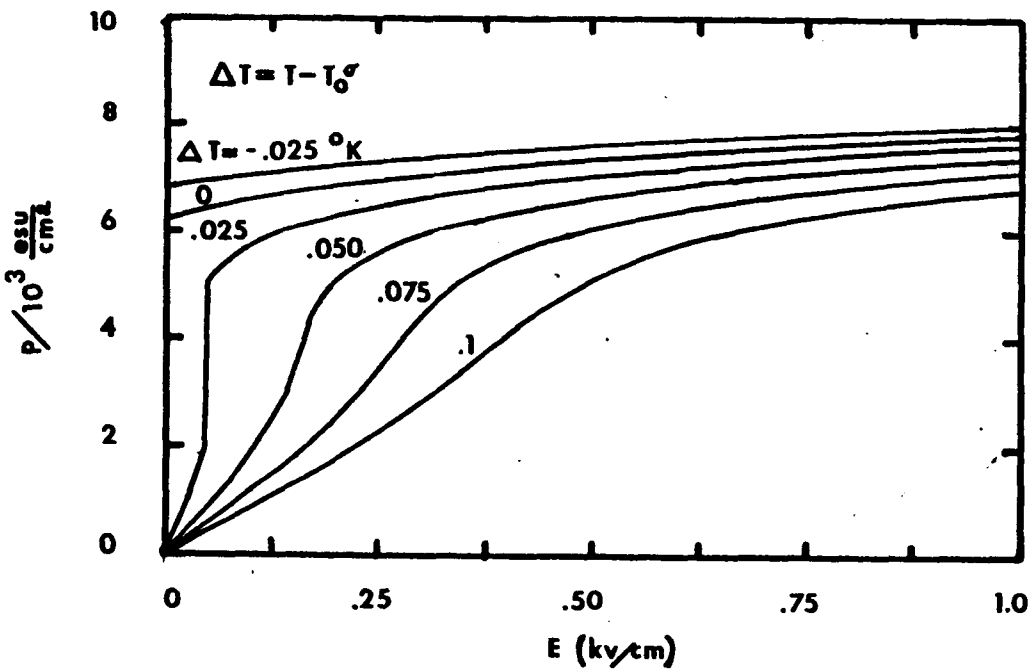

fig. III-8 Electric Field Dependence of the Polarization at constant Temperature in the Vicinity of the Transition.

uations in the thermodynamic variables)

$$\frac{4\pi}{\varepsilon^{\sigma,T}} = \alpha_0(T-T_0^{\sigma}) + 3bP^2 + 7\tilde{d}P^6 \qquad b<0 \quad 1^{st}\text{ order} \tag{19}$$

In the paraelectric phase with E = 0, there is no net polarization P. Therefore $\varepsilon^{\sigma,T}$ simply obeys a Curie-Weiss law approaching a singularity at the free Curie temperature T_0^{σ}. However, for the 1st order transition T_c is greater than T_0^{σ} (eq. 16) so that $\varepsilon^{\sigma,T}$ never becomes singular. In the presence of an electric field, $P \neq 0$ in the paraelectric phase (see Figures 2 and 3). Figure 9 is a plot of $\frac{4\pi}{\varepsilon}$ as a function of polarization as determined by equation (19). The dashed lines represent the three terms in equation (19) and the solid line is $\frac{4\pi}{\varepsilon}$ which is equal to their sum. Because $b<0$, it is possible to choose a critical temperature T_{cr} and critical polarization P_{cr} (and therefore a critical electric field) such that the susceptibility is infinite at the critical point and positive everywhere. These physical constraints are expressed mathematically by

$$(i) \quad \varepsilon^{-1}\Big|_{P_{cr},T_{cr}} = 0 \qquad \text{(singularity)}$$

$$(ii) \quad \frac{\partial \varepsilon^{-1}}{\partial P}\Big|_{P_{cr},T_{cr}} = 0 \qquad \text{(extremum)}$$

$$(iii) \quad \frac{\partial^2 \varepsilon^{-1}}{\partial P^2}\Big|_{P_{cr},T_{cr}} \geq 0 \qquad \text{(absolute minimum)}$$

These constraints, along with the equation of state, yield the following for the critical polarization, temperature and electric field.

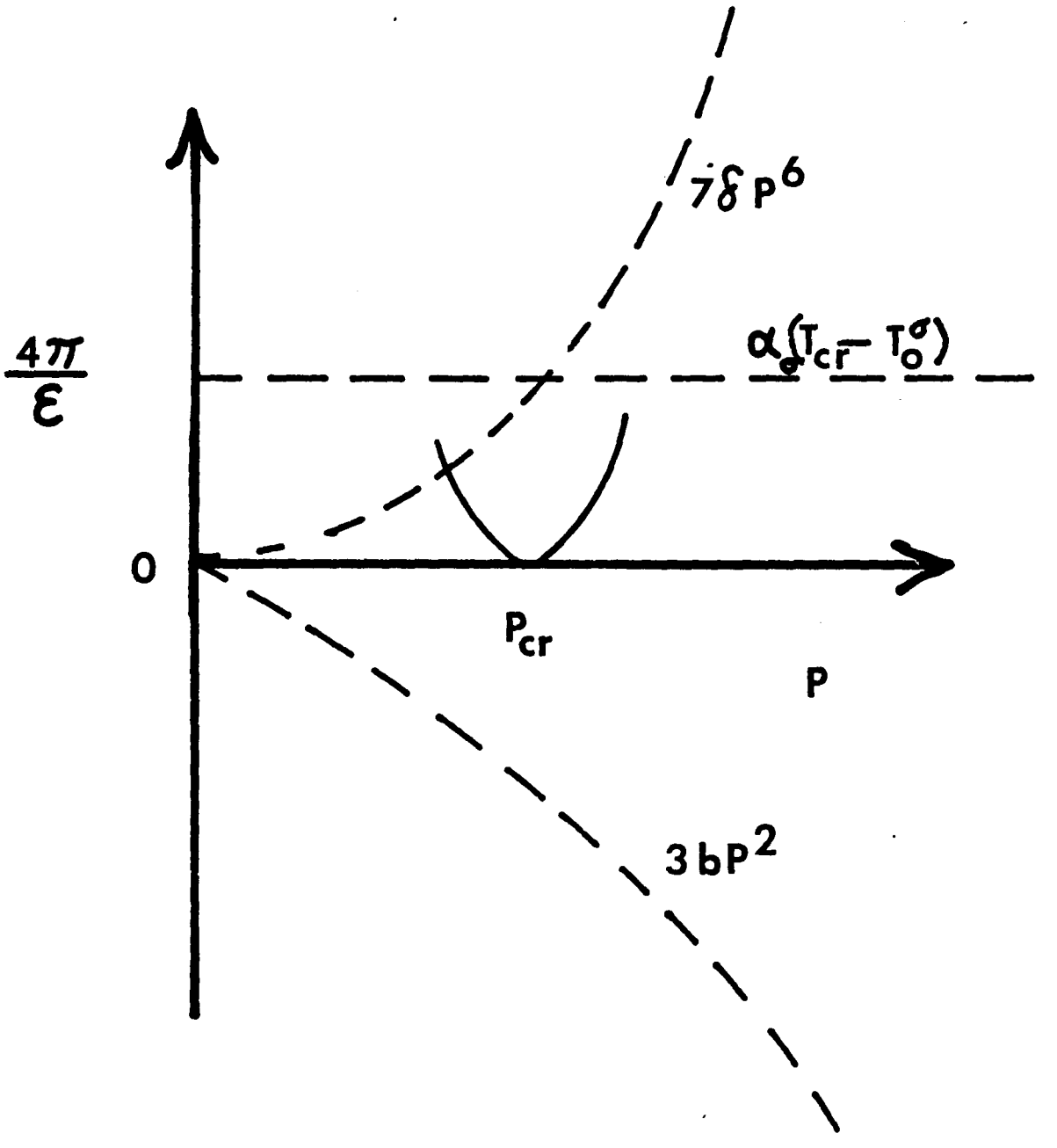

fig. III-9 Singularity of the static suceptibility $\varepsilon^{\sigma,T}$ at the critical point (see equation 19).

$$P_{cr}^4 = -\frac{b}{7\delta}$$

$$T_{cr} = T_0^\sigma - \frac{2b}{\alpha_0}\left(-\frac{b}{7\delta}\right)^{1/2}$$

$$E_{cr} = -\left(\frac{8b}{7}\right)\left(\frac{-b}{7\delta}\right)^{3/4}$$

Substitution, of the B-R free energy parameters, yields

$$P_{cr} = 3.82 \times 10^3 \frac{esu}{cm^2}\ , \quad T_{cr} = T_0^\sigma + 0.033\,^\circ K\ , \quad E_{cr} = 83.9\ V/cm\ .$$

Hence, $\varepsilon^{\sigma,T}$ will be singular, at ambient stress, for $(T,E) = (T_{cr}, E_{cr})$ and therefore exhibit a temperature dependence characteristic of a 2nd order transition.

These results are conveniently presented in a phase diagram. In figure 10, I have sketched the phase diagram for KDP in the electric field-temperature plane [85] (corresponding to atmospheric pressure). The thermodynamic state of the crystal is specified by the electric field and temperature (E, T). The hatched line corresponds to the phase transition as it occurs in the electrically shorted crystal (E = 0). As the crystal is cooled through the transition temperature T_c, there is a discontinous jump, from zero, in the spontaneous polarization and the crystal becomes ferroelectric. This behavior of the order parameter is shown in figure 6. For $E<E_{cr}$, cooling of the crystal will cause an induced first order transition when the state of the crystal crosses the solid line of induced transitions. This process is illustrated by path (i). The temperature dependence of the net polarization (combined spontaneous and induced polarizations) and the associated jump is illustrated in figure 7 for E = 50 V/cm < E_{cr}. Similarly, if the crystal is initially in the paraelectric

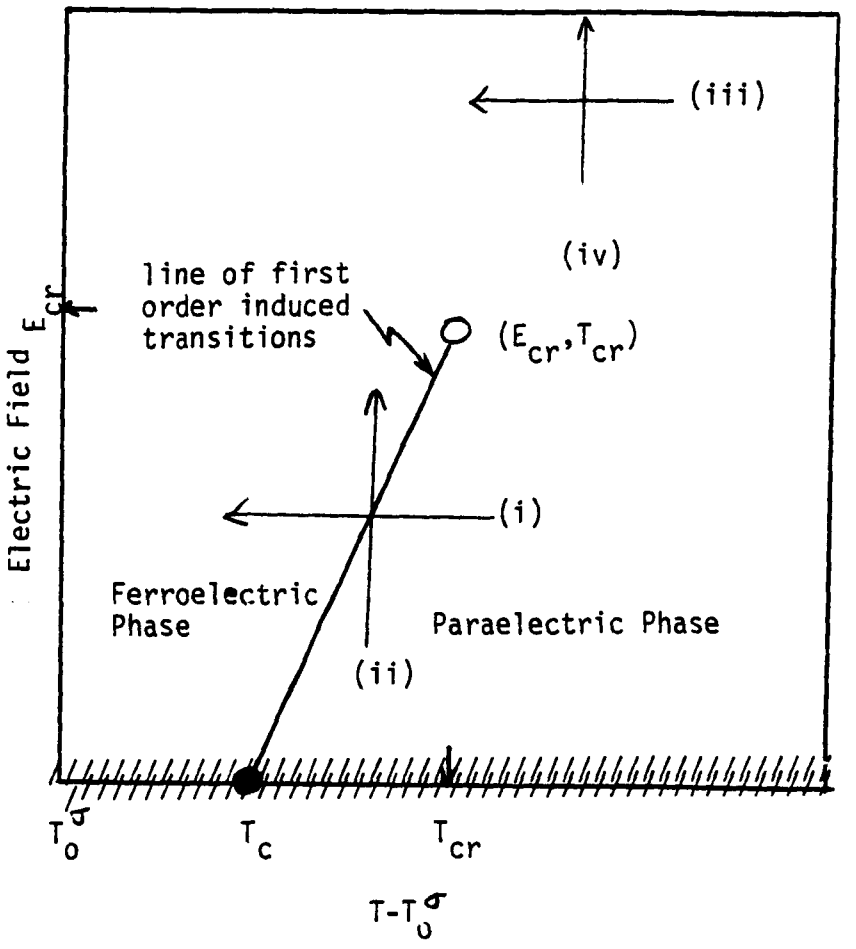

fig. III-10 Electric field- Temperature plane phase diagram for first order ferroelectric transition.

phase close to T_c, an increase of the electric field, at constant temperatures, will cause the state point to cross the line of induced 1st order transitions and the net polarization will experience a discontinuous jump. This is illustrated in fig. [10] for $T_c < T < T_{cr}$ by path (ii). At the critical point (E_{cr}, T_{cr}) these discontinuous jumps in the net polarization will disappear and $P(E_{cr}, T_{cr})$ will be points of inflection in figures 7 and 8. For temperatures and/or electric fields greater than their critical values, there is no longer an unambiguous distinction between the ferroelectric and paraelectric phases since the net polarization varies smoothly as a function of temperature and electric field. For example, the polarication along path (iii) is illustrated in figure 3 for $E > E_{cr}$ and the polarization along path (iv) is illustrated in figure 4 for $T > T_{cr}$. This phase diagram is particularly useful to this thesis work since I have performed light scattering experiments in several regions of this phase space. The experimental results can be directly related to the appropriate thermodynamic properties.

e. Thermodynamic Response Functions

Fluctuations in the thermodynamic state variables (polarization, strain, temperature, etc.) can be expressed in terms of the Helmholtz free energy given by eg. (6) (see Brody 1974). Several of the response functions, associated with the fluctuations in the thermodynamic variables, that are of interest to the present light scattering experiments are discussed below:

(1) $\varepsilon^{\sigma,T}$ Free Isothermal Dielectric Susceptibility

The dielectric susceptibility has been discussed above. The

electric field dependence of $\varepsilon^{\sigma,T}$ in the vicinity of the critical point is illustrated in Figure 11. Note that the singularity in $\varepsilon^{\sigma,T}$ is evident near $(T, E) = (T_{cr}, E_{cr})$.

(2) $C_{66}^{E,T}$: Isothermal Elastic Constant

The isothermal elastic constant can be written as:

$$C_{66}^{E,T} = \left(\frac{\partial \sigma}{\partial x_6}\right)_{E,T}$$

or

$$(20) \qquad C_{66}^{E,T} = C^{P,T}\left\{\frac{\alpha_0(T-T_0^{\sigma}) + 3bP^2 + 7\delta P^6}{\alpha_0(T-T_0^{x}) + 3bP^2 + 7\delta P^6}\right\}$$

where $C^{P,T} = 7.0 \times 10^{10} \frac{\text{dynes}}{\text{cm}^2}$ is the elastic constant at constant polarization and $T_0^x = 117.7°K$ is the clamped Curie temperature. The electric field dependence of $C_{66}^{E,T}$, as predicted by (20), is shown in Figure 12. $C_{66}^{E,T}$ is expected to exhibit critical behavior, first decreasing ($E<E_{cr}$) and then increasing ($E>E_{cr}$) as E is increased.

(3) $C_{66}^{E,S}$: Adiabatic Elastic Constant

The adiabatic elastic constant is

$$C_{66}^{E,S} = \left(\frac{\partial \sigma}{\partial x_6}\right)_{E,S}$$

or

$$(21) \qquad C_{66}^{E,S} = C^{P,T}\left\{\frac{\alpha_0(T-T_0^{\sigma}) + 3b'P^2 + 7\delta P^6}{\alpha_0(T-T_0^{x}) + 3b'P^2 + 7\delta P^6}\right\}$$

where $b' = b + \frac{1}{3}\Delta_0$.

Δ_0 is related to the adiabatic correction term (see Brody [84] 1974) and is

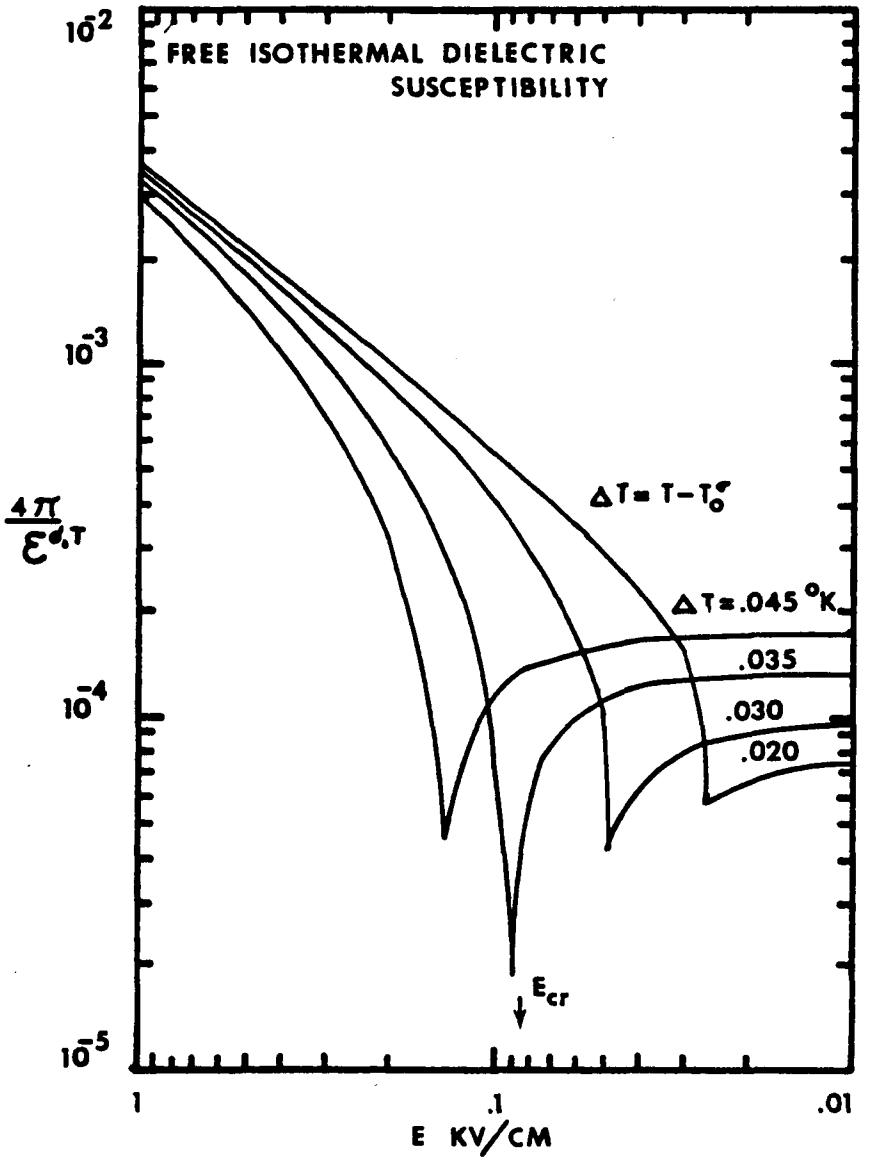

fig. III-11 Electric Field Dependence of the Free Isothermal Dielectric Susceptibility

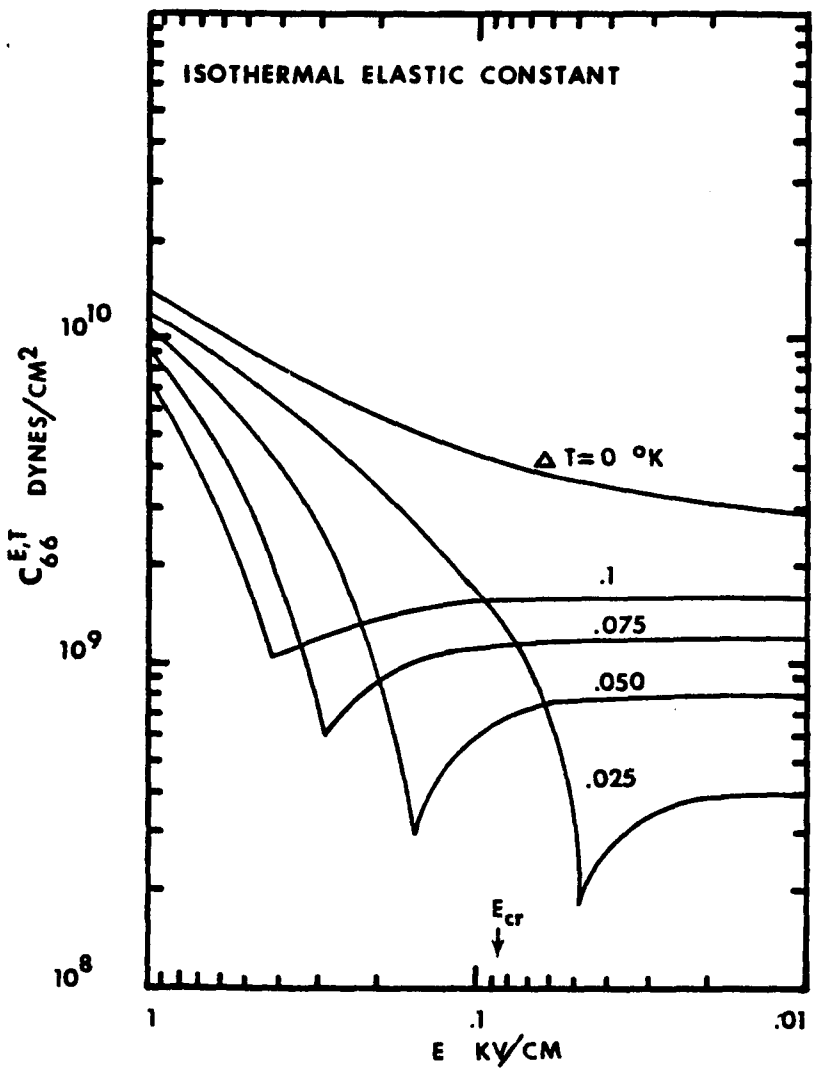

fig. III-12 Electric Field Dependence of the Isothermal Elastic Constant $C_{66}^{E,T}$. $\Delta T = T - T_o^o$

given by

$$\Delta_o = \frac{\alpha_o^2 T}{\tilde{C}}$$

$\tilde{C}$ - specific heat per unit volume due to degrees of freedom not participating in the phase transition

For $\tilde{C} = 1.03 \times 10^7 \frac{erg}{cm^3 - °K}$ and T = 120°K I find:

$$\Delta_o = 1.74 \times 10^{-10} \frac{cm^4}{esu^2}$$

and

$$b' = +5.36 \times 10^{-11} \frac{cm^4}{esu^2}$$

Because b'>0, $C_{66}^{E,S}$ is not expected to exhibit critical behavior (as does $C_{66}^{E,T}$). Figure 13 illustrates the electric field dependence of $C_{66}^{E,S}$ as determined by (12). Notice that $C_{66}^{E,S}$ increases with E for all E, and exhibits a discontinuous jump for $T_c \leq T < T_{cr}$.

(4) $\tilde{p}^{\sigma,E}$: Pyroelectric Susceptibility

The pyroelectric susceptibility is defined as

$$\tilde{p}^{\sigma,E} = \left(\frac{\partial P}{\partial T}\right)_{\sigma,E}$$

The free energy yields the following expression for $\tilde{p}^{\sigma,E}$:

$$(22) \qquad \tilde{p}^{\sigma,E} = -\varepsilon^{\sigma,T} \frac{P}{C}$$

where $\varepsilon^{\sigma,T}$ is given by (11) and C is the Curie constant. For the shorted crystal in the parelectric phase, $\tilde{p} = 0$. The temperature dependence of $\tilde{p}^{\sigma,E}$ predicted by (14) is shown in Figure (14) The electric field dependence for

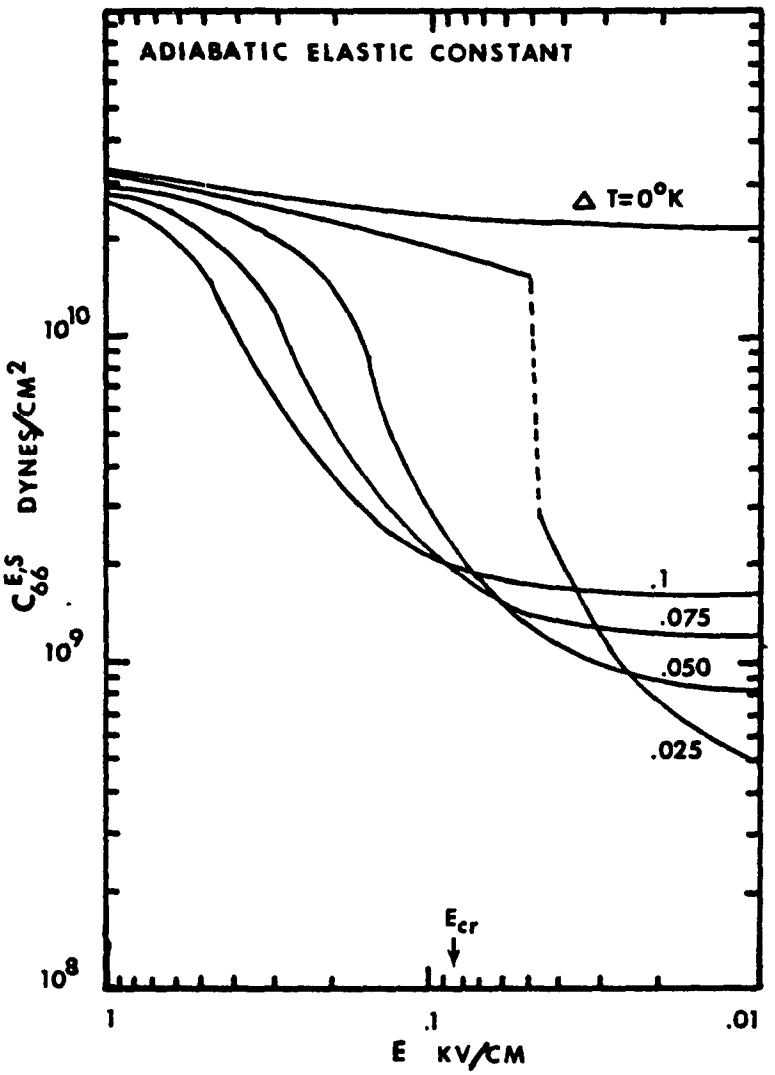

fig. III-13 Electric Field Dependence of the Adiabatic Elastic Constant $C_{66}^{E,S}$. $\Delta T = T - T_o^{\sigma}$.

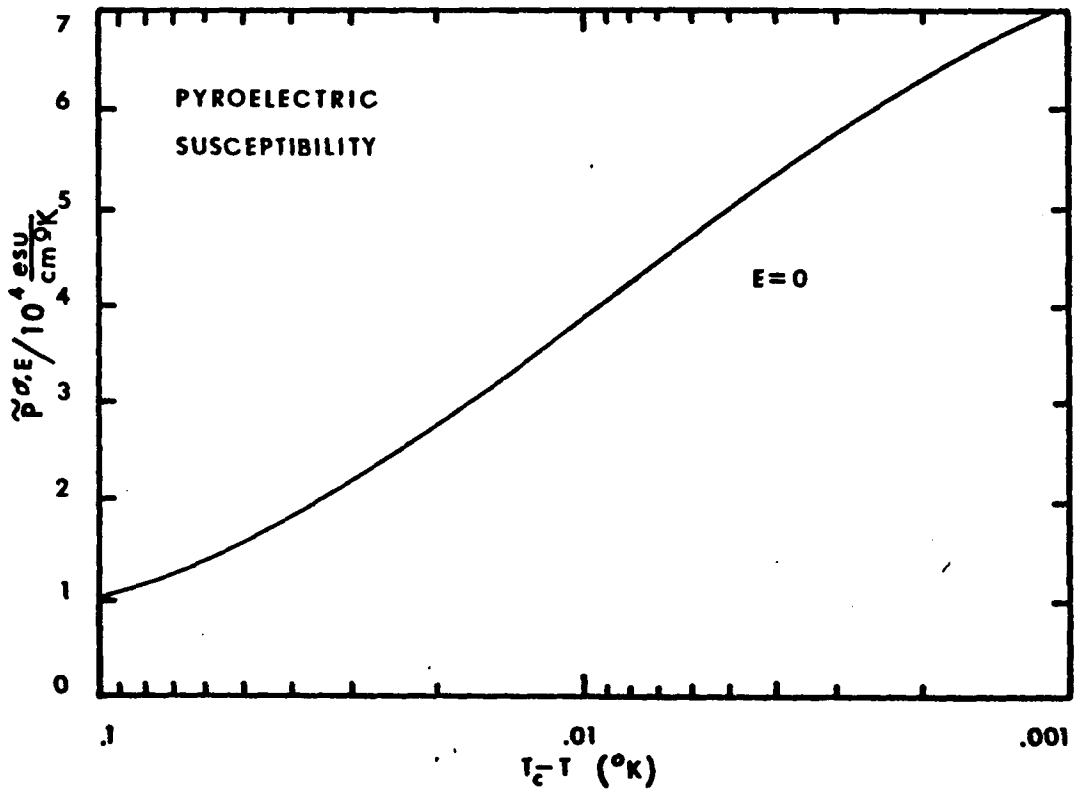

fig. III-14 Temperature Dependence of the Pyroelectric Susceptibility

the pyroelectric coefficient is shown in Figure (15). $\tilde{p}^{\sigma,E}$ will exhibit critical behavior determined by $\varepsilon^{\sigma,T}$.

(5) Thermal Dilatation Coefficient

The thermal dilatation coefficient is defined by:

$$\tilde{q}^{\sigma,E} = \left(\frac{\partial x}{\partial T}\right)_{\sigma,E}$$

and is related to the pyroelectric susceptibility by:

$$\tilde{q}^{\sigma,E} = \frac{a^T}{C^{P,T}}\,\tilde{p}^{\sigma,E} \tag{23}$$

(6) Excess Specific Heat

The specific heat at constant stress and electric field is given by: [85]

$$C_{\sigma,E} = T\left(\frac{\partial S}{\partial T}\right)_{\sigma,E} \tag{24}$$

where S is the entropy. The entropy can be obtained from the Helmholtz free energy A(T, x . P) and is given by:

$$S = -\left(\frac{\partial A}{\partial T}\right)_{x,P} = -\left(\tfrac{1}{2}\alpha_0 P^2 + S_1\right) \tag{25}$$

S is the entropy associated with degrees of freedom not participating in the transition. Hence

$$C_{\sigma,E} = C_0 - \tfrac{1}{2}\alpha T\left(\frac{\partial P^2}{\partial T}\right)_{\sigma,E} \tag{26}$$

where $C_0 = T\left(\frac{\partial S_1}{\partial T}\right)_{\sigma,E}$ is the background specific heat.

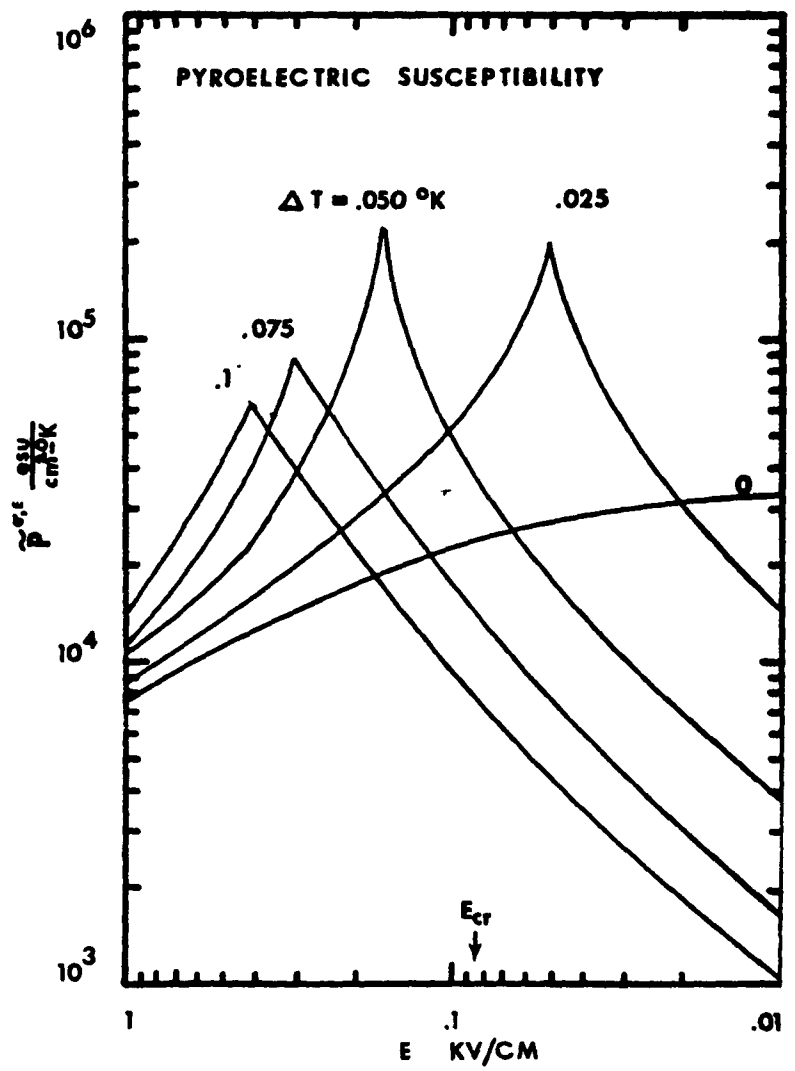

fig. III-15 Electric Field Dependence of the Pyroelectric Susceptibility. $\Delta T = T - T_0$.

Using (22) for the pyroelectric coefficient, the specific heat can be written as:

$$C_{\sigma,E} = C_0 + \left(\frac{\gamma\pi}{\varepsilon^{\sigma,E}}\right) T \left(\tilde{\rho}^{\sigma,E}\right)^2 \tag{27}$$

E. Conclusion

In summary, this chapter has touched upon some of the major points in the development of the microscopic theory of the ferroelectric transition in KH_2PO_4. Examination of the phenomenological thermodynamic theory has allowed the determination of several thermodynamic response functions of experimental interest. In particular the electric field dependence of several thermoynamic properties has been investigated.

IV. Light Scattering Theory

A. Scattered Electric Field

In this chapter I will present the classical theory of light scattering from a condensed medium in the dipole approximation. [86]

Consider a plane wave incident on a volume element d^3r', whose index of refraction is n. The electric field is represented by a monochromatic wave of polarization $\hat{e}_o$, wave vector $\underset{\sim}{k}_o$, and frequency ω_o.

$$(1) \qquad \underset{\sim}{E}_o = \hat{e}_o E_o e^{-i(\underset{\sim}{k}_o \cdot \underset{\sim}{r}' - \omega_o t')}$$

Light will be scattered by the presence of inhomogeneities in the optical dielectric constant tensor of the medium which are induced by a variety of thermal processes (such as sound waves, thermal diffusion, etc.) The local dielectric constant tensor can be expressed as: $\underset{\approx}{\varepsilon}(\underset{\sim}{r},t) = \varepsilon_o \underset{\approx}{1} + \delta\underset{\approx}{\varepsilon}(\underset{\sim}{r},t)$. The fluctuating contribution to $\underset{\approx}{\varepsilon}$ produces an excess polarization given by:

$$(2) \qquad P(\underset{\sim}{r},t) = \frac{1}{4\pi} \delta\underset{\approx}{\varepsilon}(\underset{\sim}{r},t)\, \underset{\sim}{E}_o(\underset{\sim}{r},t).$$

In the dipole approximation, such a fluctuating excess polarization will

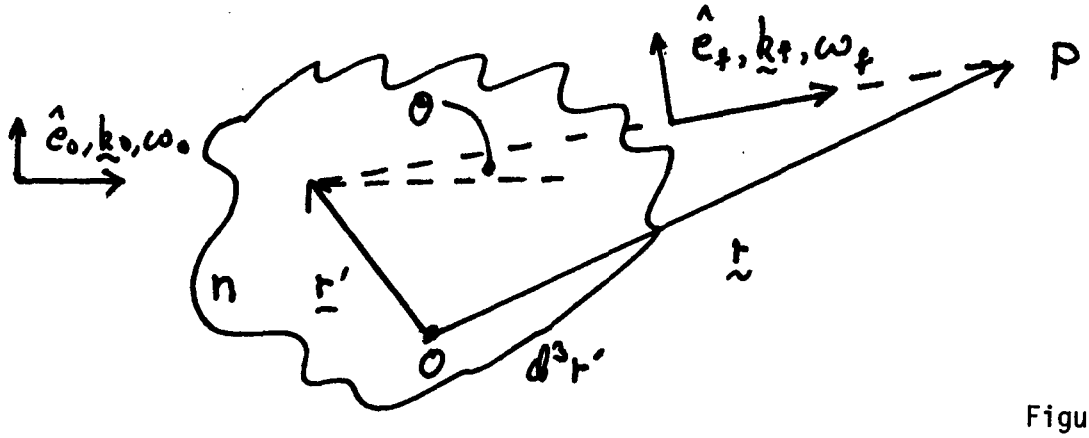

Figure IV -1

produce a scattered electric field at the far field point P (where r >> r') given by:

$$(3)\quad E_s(\underset{\sim}{r},t) = \frac{\pi E_0}{\lambda^2 r}\, e^{i(\underset{\sim}{k}_f\cdot\underset{\sim}{r}-\omega_0 t)} \int_V \delta\varepsilon_{f_0}(\underset{\sim}{q},t)$$

where $\delta\varepsilon_{f_0}(\underset{\sim}{q},t) = \hat{e}_f\cdot\delta\underset{\approx}{\varepsilon}(\underset{\sim}{q},t)\cdot\hat{e}_0$, $\hat{e}_f$ and $\underset{\sim}{k}_f$ are the polarization and wave vector of the scattered wave, respectively, and $\underset{\sim}{q} = \underset{\sim}{k}_0 - \underset{\sim}{k}_f$ is the momentum transfer expressing the Bragg condition for scattering.

B. Intensity Spectrum

The Wiener-Khintchine theorem yields the intensity spectrum of the scattered light in terms of the autocorrelation function of the scattered electric field:

$$(4)\quad I_s(\underset{\sim}{q},\omega,r) = \frac{1}{2\pi}\int dt\, e^{i\omega t}\left\langle E_s^*(\underset{\sim}{r},0)\,E_s(\underset{\sim}{r},t)\right\rangle$$

Substitution of (3) into (4) yields the spectrum in terms of fluctuations in the dielectric constant tensor:

$$(5)\quad I_s(\underset{\sim}{q},\omega,r) = \left[\frac{\pi^2 I_0 V^2}{\lambda^4 r^2}\right]\frac{1}{2\pi}\int_{-\infty}^{+\infty} dt\, e^{i(\omega+\omega_0)t}\left\langle \delta\varepsilon_{f_0}^*(\underset{\sim}{q},0)\,\delta\varepsilon_{f_0}(\underset{\sim}{q},t)\right\rangle$$

where $I_0 = |E|^2$ and $\delta\varepsilon(\underset{\sim}{q},t)$ is the spacial Fourrier transform of $\delta\varepsilon(\underset{\sim}{r},t)$.

. Fluctuations in ε due to thermal processes in the medium can be expressed by:

$$(6)\quad \delta\varepsilon_{f_0}(\underset{\sim}{q},t) = \sum_i P_i\, A_i(\underset{\sim}{q},t)$$

where P_i are the optical coupling coefficients and $A_i(q,t)$ are the fluctuating physical quantity of wave vector q. The intensity spectrum can now be expressed as:

$$(7)\quad I_s(\underset{\sim}{q},\omega,r) = \frac{\pi^2 I_0 V^2}{\lambda^4 r^2} \sum_{i,j} P_i P_j (A_i A_j)_\omega .$$

$(A_iA_j)\omega$ is the spectral density of the fluctuations in $A_i(q,t)$ and is given by:

$$(8)\quad (A_iA_j)_\omega = \frac{1}{2\pi} \int_{-\infty}^{+\infty} dt\, e^{i(\omega+\omega_0)t} \langle A^*(\underset{\sim}{q},0)\, A(\underset{\sim}{q},t) \rangle$$

This spectral density is given by the classical fluctuation dissipation theorem in terms of the imaginary part of the susceptibility of the coordinates A_i in the limit $\omega << k_BT/\hbar$

$$(9)\quad (A_iA_j)_\omega = \frac{k_BT}{\pi\omega} Im\, \chi_{ij}(\omega)$$

where χ_{ij} is the response of coordinate A_i to a unit driving force conjugate to coordinate A_j. The χ_{ij} are obtained from the system's equations of motion. Hence, the spectrum of scattered light can be expressed as:

$$(10)\quad I_s(\underset{\sim}{q},\omega,r) = \left[\frac{\pi^2 I_0 V^2}{\lambda^4 r^2}\right]\left[\frac{k_BT}{\pi\omega}\right] \sum_{i,j} P_i P_j Im\, \chi_{ij}(\omega)$$

C. Integrated Intensity

The integrated intensity is obtained by integrating (5) over frequency:

$$(11)\quad I_s(q,r) = \int_{-\infty}^{+\infty} d\omega\, I_s(q,\omega,r)$$

Use of the definition of the delta function:

$$2\pi\delta(t) = \int_{-\infty}^{+\infty} d\omega\, e^{i\omega t} \tag{12}$$

yields,

$$I_s(\underset{\sim}{q}, r) = \frac{\pi^2 I_o V^2}{\lambda^4 r^2} \left\langle \left| \hat{e}_s \cdot \delta\underset{\approx}{\varepsilon}(q) \cdot \hat{e}_o \right|^2 \right\rangle \tag{13}$$

It is convenient to define the Rayleigh ratio R as the scattering cross section per unit volume, or $R = \frac{I}{I_o V r^2}$, so that the integrated intensities can be expressed as:

$$R = \frac{\pi^2 V}{\lambda^4} \left\langle \left| \hat{e}_s \cdot \delta\underset{\approx}{\varepsilon}(\underset{\sim}{q}) \cdot \hat{e}_o \right|^2 \right\rangle \tag{14}$$

Note that the integrated intensity is proportional to the mean square fluctuation of the dielectric constant.

V. Experimental Considerations

In this chapter I will discuss the experimental apparatus pertinent to the results presented in this thesis.

A. Optical Layout

(1) Overview.

A schematic diagram of the optical layout is presented in figure 1. The argon-ion laser is run in single mode operation by use of an intra-cavity etalon. The laser beam is focused into the dewar by lens L1 whose focal length is chosen so that the beam focuses at the center of the crystal. Before the beam enters the sample cell it passes through a Glan-Thompson prism, oriented to pass light vertically polarized with respect to the optical table. The prism is needed to correct for strain induced bire-fringence in the dewar windows which tends to depolarize the entering laser beam at low temperatures. Light scattered at 90° is collected by lens L2. The polarization of the scattered light is selected by the polaroid analy-ser and the aperture is determiend by the adjustable iris. The scattered light is frequency analysed by either a pressure scanned plane parellel Fabry-Perot interferometer or a piezo-electrically driven confocal spher-ical Fabry-Perot interferometer. The former instrument is used to study the Brillouin spectra while the latter is used to study the quasi-elastic spectrum (the interferometers are discussed in more detail below). The light is focused by lens L3, through a laser line filter and pinhole of selectable diameter. The intensity of the light is measured by an I.T.T. FW-130 photmultiplier tube maintained at 1750 volts D.C. The electrical pulses emitted by the photomultiplier are processed by a preamplifier-discriminator module . The rate at which the photoelectons are emitted

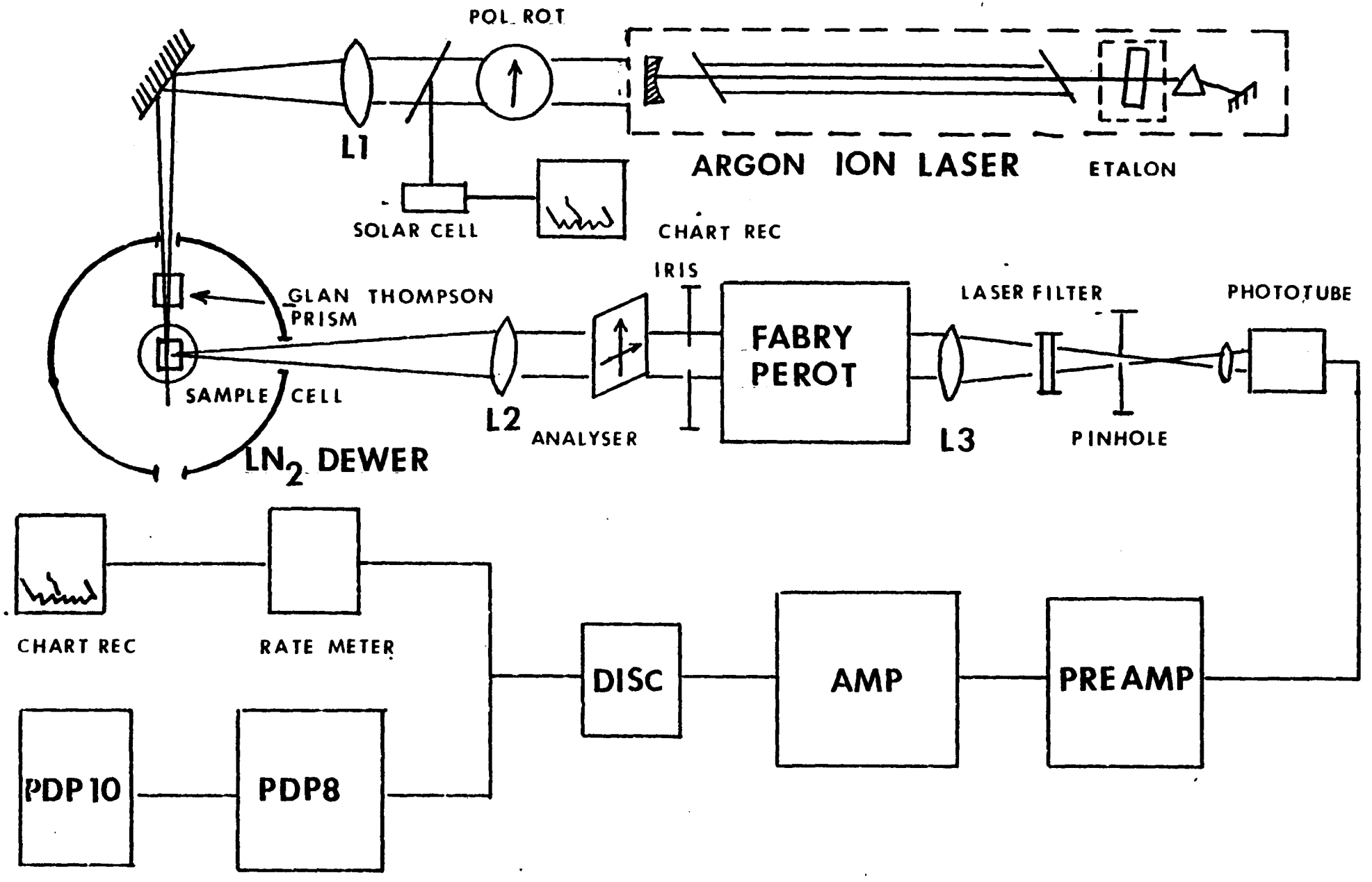

fig. V-1 Optical Layout

(proportional to the scattered light's intensity) is measured either by a rate meter, whose output is then recorded on a strip chart recorder, or by the PDP 8 minicomputer, which has been programmed to function as a multichannel analyser. The spectrum measured by the PDP 8 is then stored in memory and may be transferred to the PDP 10 computer for storage and analysis.

(2) Lasers.

In these experiments, two argon-ion lasers were used: a Spectra-Physics model 165 laser and Coherent Radiation model 52 laser. All experiments were performed with λ = 5145 Å. It was found that the Spectra-Physics laser exhibited greater intensity and mode stability while the Coherent Radiation laser showed a more narrow line width.

In making quasielastic ($\Delta\nu_{FWHM} \simeq$ 5MHz) measurements of the light scattering spectrum it is important for the laser to maintain good frequency stability. Frequency destabilizing events to be considered are multimoding, mode hopping, and frequency jitter. Mode separation is typically $\simeq$ 150 MHz. Therefore, if more than one mode is oscillating at a given moment, each will appear as a separate feature in the quasielastic spectrum. Mode hopping produces an abrupt change in both frequency and intensity. Therefore, it is important to maintain good single mode stability.

Single mode operation is obtained by adjusting the tilt of an intracavity etalon. The S.P. laser uses an airspaced etalon, for which this adjustment is sufficient to maintain mode stability for periods as long as an hour, after the laser has warmed up. However, the C.R. laser uses a solid etalon which needs to be temperature controlled to prevent changes in the optical path length due to the temperature dependence of the etalon's index of refraction. Temperature stability of about .01° C is required to

prevent mode hopping. [90] Therefore the etalon is housed in an oven with heaters and thermister temperature sensors. The etalon is maintained at a constant temperature (.01° C) by a Fisher proportional temperature controller (model No. 22). After the C.R. laser has warmed up for 2-3 hours, mode stability for an hour can be achieved. At this point the intensity stability is typically 1 to 3 percent.

Frequency jitter is the modulation of the laser frequency (on the order of 10 MHz) due to fluctuations in the laser cavity length. These fluctuations are induced by acoustic vibrations originating from mechanical perturbations. A chief source of these perturbations is believed to be the turbulent flow of water around the plasma tube. [91] (M. Vaughan (R.R.E Malvern) has reported stability $\sim$ 1 MHz by mounting mirrors separately, isolated from tube and water.)

An experimental estimate of the characteristic time τ and amount of frequency shift associated with the jitter (τ, being the time period during which the laser frequency will hop at least one time) was made by observing the laser intensity profile on a Tektronix 7514 storage oscilloscope. The laser spectrum was scanned by the Tropel spherical Fabry-Perot driven by the Coherent Optics Model 475 linear ramp generator. The signal was detected by a photodiode. 'Snapshots' of the laser profile were taken at different sweep times T. We can distinquish three different cases for these measurements: (1) $\frac{\tau}{T} > > 1$. The sweep rate is fast enough so that it is not likely that the laser frequency will hop during a sweep. The oscilloscope would then measure an instantaneous and narrow laser profile. (2) $\frac{\tau}{T} \simeq 1$. In this case it is probable that the laser frequency will hop during a sweep and the laser profile will exhibit a significant distortion. (3) $\frac{\tau}{T} < < 1$. The laser frequency will hop many

times during a sweep of the oscilloscope and the oscilloscope will display a long time averaged, broadened laser profile.

Photographs representative of many measurements, taken for various sweep times T, are shown in figure 2. The time scale (sec/cm) is given in each photograph and the frequency scale is 10 MHz per cm. Figure (a), at the fastest time scale, exhibits a very sharp profile, while figure (e), at the slowest time scale, exhibits significant distortion. The transition, corresponding to case 2 occurs between (c) and (d). Hence, we may estimate τ to be approximately $\tau = 750\mu s \pm 250\mu s$.

The above measurements were made for the Coherent Radiation laser with a 2 watt plasma tube. A typical number representing the extent of the frequency excursion is seen to be approximately 10 MHz.

(3) Interferometers

(a) General Description.

Two interferometers were used in these experiments. A pressure scanned plane parallel Fabry-Perot with a 2 cm spacer was used to scan the Brillouin spectrum. This instrument operated with a finesse typically between 30 and 40 and a free spatial range of 7.5 GHz.

The quasi-elastic spectrum was scanned by a spherical Fabry-Perot. This interferometer has a mirror separation of 25 cm and free spectral range of 300 MHz. The mirrors are coated to be 97% reflecting at 4880 - 5145 Å, yielding a reflectivity limited finesse of approximately 50. The frequency scan is achieved by a mirror mounted on a piezo-electric pusher and driven by a ramp voltage generator.

(b) Optical Layout

The optical layout showing the FPS and associated lens is given in

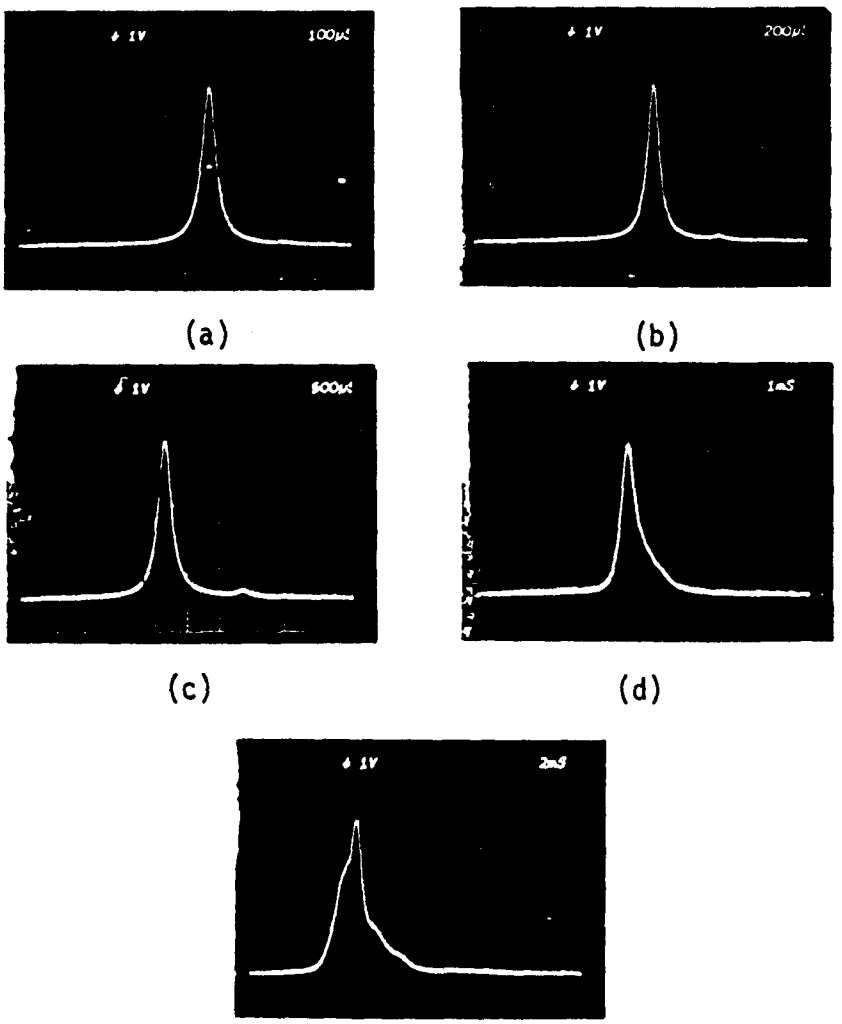

fig. V-2

figure 3.

(c) Throughputs.

The thorughputs of the FPS and FPP (2 cm) were measured separately and collectively. The throughput of the FPS was measured by focusing the laser beam (λ = 5145 Å) into the center of the inteferometer. The voltage across the piezoelectric pusher was adjusted for maximum transmission and the power of the transmitted light, P_{max}, was determined by a Coherent Radiation light meter No. 212. The FPS was then removed and the power of the direct beam, P_o, was measured.

The throughput, $T = \frac{P_{max}}{P_o}$, was found to be: $T_{FPS} = .27$. The throughput of the FPP was measured in a similar manner and found to be $T_{FPP} = .33$.

The relative throughputs of the FPS and FPP were determined by measuring the peak count rate for scattering from Polystyrene. The laser was operated at 5145 Å with 75 mW of power. The scattered light was attenuated by a #4 neutral density filter and the pinhole was set to .7mm. The collection aperture for the FPS was 3 mm and the aperture for the FPP was 1.0 cm (typical values). The relative peak count rate was found to be:

$$I_R = \frac{I_{FPS}^{max}}{I_{FPP}^{max}} = .46.$$

B. Thermal Considerations

The ferroelectric phase transition in KDP occurs at approximately 122°K. The quasielastic features, near T_c, under study are highly temperature dependent. Therefore, it is important to maintain excellent temperature control and stability. In the following paragraphs, I will discuss the

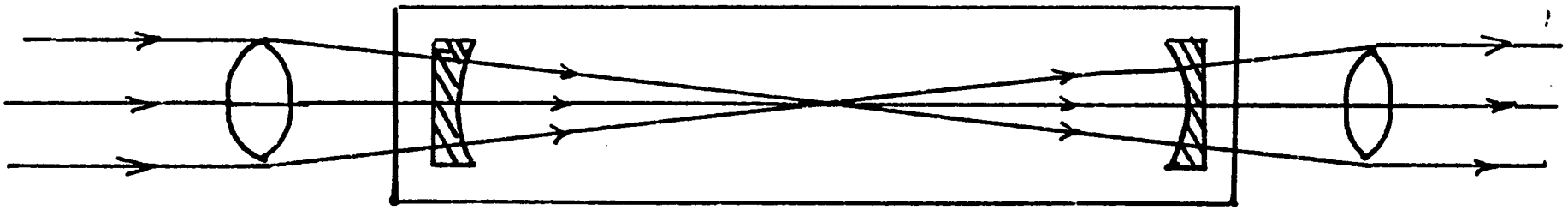

TROPEL FPS 25 CM

fig. V-3

the experimental considerations related to these two points.

(1) Dewar.

The appropriate temperatures are achieved by a homemade dewar. The details of this dewar can be found in the thesis by Brody.[92] Liquid nitrogen is used as a coolant. It is convenient to keep the crystal at the desired temperature for long periods of time (several days) so that a series of experiments can be performed. To this end a 100 liter (Cryofab) liquid nitrogen dewar was purchased and connected to the sample dewar through a cryogenic solenoid valve (Cryofab). The solenoid is powered by a Cryo-miser model L-21C liquid nitrogen level sensor. The level of the liquid nitrogen is determined by the position (height) of the two sensors (thermistors) and the range is determined by the sensor separation. 100 liters of liquid nitrogen will keep the dewar cooled at T_c for at least 24 hours.

The temperature stability is highly sensitive to the level of the nitrogen and is therefore dependent upon the sensor separation. A sensor separation of 2 mm and location of 6 cm from the top of the dewar was found to be consistent with a temperature stability of 1 m °K over a period of an hour. Cycling time for this sensor spacing is typically 20-30 minutes.

(2) Temperature Control.

The dewar has two sets of heating resistors, a 100Ω set and a 175Ω set. The 175Ω resistors were connected to a variac to provide additional heating power during the cooling down period when there is a great deal of thermal momentum. The 100Ω heater is connected to the ouput of an Artronix model 5301 temperature controller. Details concerning the opera-

tion of this unit can be found in the 'Engineering Service and Maintenance Technical Manual'. Experience has shown that 1 m° K stability over a period of an hour can be achieved by running the Artronix in the proportional mode with the 'power out' setting at maximum, and the gain control relatively high, at approximately the 10 o'clock position. Compatibility between the three dewar temperature sensors (see Brody's thesis) and the temperature range switches are given in the tables in the manual. In the vicinity of T_c, an increment in the temperature set control by the smallest division corresponds to a change in temperature of approximately 50 m° K. A ten turn 10Ω trimmer pot was connected in series with the temperature set control to facilitate fine adjustments in temperature. Increments of 20 units of the trimmer pot will change the temperature of the crystal by approximately 5 m° K.

(3) Temperature Measurement.

The temperature measurement apparatus is discussed by Lagakos. [4] The platinum resistance thermometer was moved to the interior of the sample cell, seated in the bakelite mounting for the crystal, in order to give a more accurate representation of the crystal's ambient temperature. The resistance of the thermometer and therefore, the temperature, is determined by a Julie potententiometer UPB-100, as discussed by Lagakos. A chart recorder was connected across the null detector meter to monitor small (1 m °K) fluctuations in temperature.

(4) Sample Cell.

The sample cell is the same as that used by Lagakos. However, it was necessary to develop a technique for mounting the windows so that upon cooling the contracting (brass) sample cell would not strain the windows and depolarize the laser light. The windows were mounted by epoxying

an invar ring to the window seat and then epoxying the window to the invar ring. The invar and glass have very low coefficients of thermal expansion so that the strains originating at the glass-invar interface are minimized. The forces produced by the contracting brass are buffered by the invar ring, thereby reducing the effect on the quartz window. Armstrong 271 epoxy is used and best results are obtained by curing at 200°F in an oven for half an hour. This procedure is illustrated in figure V-4. The complete temperature controlling apparatus is shown in figure V-5.

(5) Laser Heating of the Focal Volume.

A further important thermal consideration of the experiment is the heating of the focal volume in the crystal by the laser. In appendix A a calculation is done to determine the temperature gradients in the crystal produced by the laser beam. The calculation estimates that for a 100 mW laser beam in KDP near T_c, the temperature gradient across the focal volume is less than 1 m ^{o}K. This is primarily due to the transparency of the crystal. Therefore, although the quasi-elastic features near T_c are extremely temperature dependent, they may be observed with substantial laser powers without significant thermal perturbation. Other results of the calculation are compared directly to experiment.

c)Materials

The crystals used in these experiments are tabulated below. All crystals were cut, by a wet string saw, for scattering from the $\hat{x}$ phonon Crystal polishing and sample preparation are essentially the same as dis-

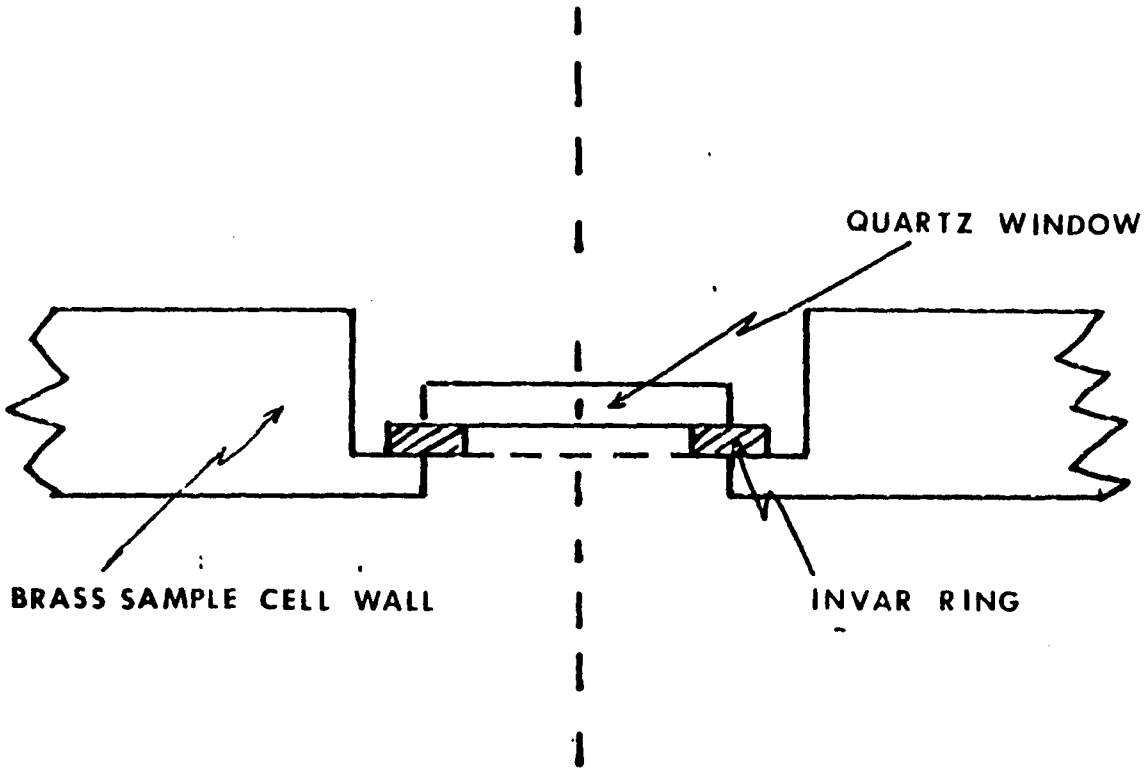

fig. V-4

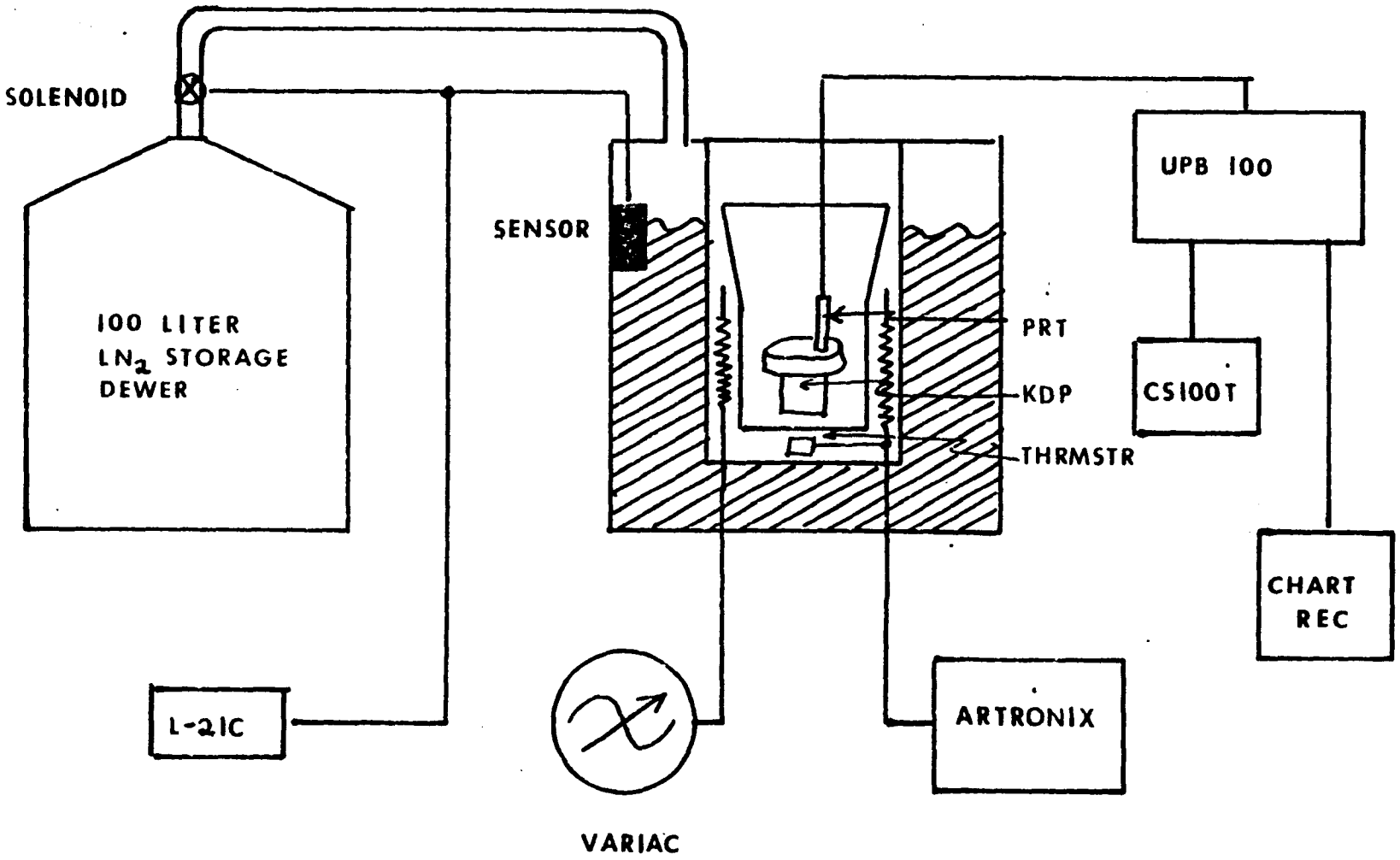
SOLENOID
100 LITER
LN2 STORAGE
DEWER
SENSOR
PRT
KDP
THRMSTR
UPB 100
CS100T
CHART
REC
L-21C
VARIAC
ARTRONIX

fig. V-5

cussed by Lagakos.[4] Silver paint (G.C Electronics, Division of Hydrometals, Inc., Rockford, Illinois) electrodes were used for KDP9 and KDP13.

Table I

CRYSTAL	MANUFACTURER	ORIENTED	OPTICAL QUALITY	COMMENTS
KDP5	Isomet Corp. Oakland, N.J. (1971) No longer manufactures KDP.	X-rayed in house	poor, high density of visible inclusions, small cracks	Used in SCP sample dependent experiment, exhibits strongest SCP
KDP7	Isomet Corp. (1972)	X-rayed by manufacturer and in house	good, few visible inclusions	Used in CP experiments by Lagakos (3) and Mermelstein (5). Destroyed in 1977.
KDP9	Interactive Rad. Northvale, N.J. (1977)	X-rayed by manufacturer	fair, some visible inclusions	Third cystal used in SCP sample dependence experiments. SCP of medium strength. Destroyed in 1978.
KDP13	Lasermetrics Inc. Teaneck, N.J. (1977)	X-rayed by manufacturer	excellent, exceptionally clean scattering column	Used in SCP and DCP experiments of this thesis.

Chapter VI - Static Central Peak - Experiment and Interpretation

A. Experiment

1) Experimental setup

Brillouin spectra were taken in the x + z(y, x + z) - x + z scattering geometry with the 2 cm plane parallel Fabry-Perot interferometer (FPP). The laser was run single mode at 5145 Å. Laser power during these experiments was approximately 220 mW and was stable to better than 5%.

2) Data reduction

The Brillouin spectra, digitally recorded in a 512 point array by the PDP 8 minicomputer, were subsequenlty analyzed by a computer assisted curve-fitting procedure (to be discussed below). The measured spectrum was fit to the convolution of a parameterized transmission function of the FPP, $T(\nu)$, with a parameterized theoretical spectral density function, $S(\nu)$, representing the static central peak (SCP) and the transverse acoustic (T.A.) phonon.

The transmission function was gnerated from the Airy function: [93]

$$(1) \qquad T(\nu) = \frac{1}{1 + F \sin^2 \frac{\varphi(\nu)}{2}}$$

where F is a parameter related to the reflectivity-limited finesse and $\phi(\nu)$ is the phase factor determining the interferometer's resonance condition. Previous experiments have shown that the central peak in the paraelectric phase exhibits no intrinsic linewidth. [24] Therefore, the paraelectric central peak was used to determine the para-

meter F of the instrumental lineshape.

3) Brillouin Lineshape

The spectral density function for the SCP plus phonon is represented by

$$S(\nu) = S_s(\nu) + S_p(\nu) + B \qquad (2)$$

$S_s(\nu)$ is the spectral density function for the SCP and is given by

$$S_s(\nu) = A_s(T)\, d(\nu)$$

The coefficient $A_s(T)$ contains the diverging temperature dependence. The phonon spectral density function, $S_p(\nu)$, is correctly obtained from a coupled mode analysis describing the piezoelectric coupling of the ferroelectric soft mode and the Xy shear mode (T.A. phonon). [94,25] However, reasonable fits to the Brillouin lineshape which provide approximate representations of the integrated intensities, were obtained by representing $S_p(\nu)$ by a damped harmonic oscillator response function:

$$S_p(\nu) = A_p\, Im\left[\nu_o^2 - \nu^2 + i\nu\Gamma_o\right]^{-1}$$

where ν_o is the quasiharmonic frequency and Γ_o is the damping coefficient. The elastic constant for the Xy shear mode, C_{66}, is related to the parameter ν_o by:

$$C_{66} = \frac{\rho\omega_o^2}{q^2}$$

where: $\omega_o = 2\pi\nu_o$, the mass density is $\rho = 2.34$ gm/cm^3 and the square of the momentum transfer is $q^2 = 6.71 \times 10^{10}$ cm^{-2}. The integrated intensities of the SCP and phonon peaks were taken to be proportional to the areas under $S_s'(\nu)$ and $S_p'(\nu)$ respectively, for one free spectral range, where $S'(\nu)$ is the convoluted spectrum $S(\nu) \otimes T(\nu)$.

4) Curve-fitting Procudure

Several Brillouin spectra were analyzed by convoluting the parameterized spectral density function S (ν) with the parameterized transmission function T (ν) and adjusting the parameters to produce a best non-linear least squares fit. This was done with the Tauros program. However, this procedure was found to require an excessive amount of computer time. Therefore, the majority of the spectra were fit by a simpler computer-assisted curve-fitting procedure. Initial guesses to the parameters values were made. A visual comparison was then made between the resultant convoluted spectrum and the experimental spectrum. The parameters were readjusted to improve the fit. In this manner best values for the parameters were obtained that differed by less than 10% from those obtained with the Tauros nonlinear least-square fitting routine. Several Tauros runs, on selected spectra with different initial parameter values, were made in order to estimate the error associated with the parameter values obtained from the curve-fitting procedure.

B. Experimental Results

1) Temperature dependence

Figure 1 shows the intensities observed in the Brillouin spectra of a KDP crystal. Shown are the integrated intensities of the Rayleigh line and longitudinal phonon that appear in the polarized scattering and the central peak and transverse acoustic phonon that appear in the depolarized scattering. The intensities are plotted (on a log-log scale) as a function of $T - T_o^{\sigma}$ over the temperature range $T_c < T - T_o^{\sigma} < 100°K$. T_o^{σ} is the free Curie temperature and T_c is the transition temperature.

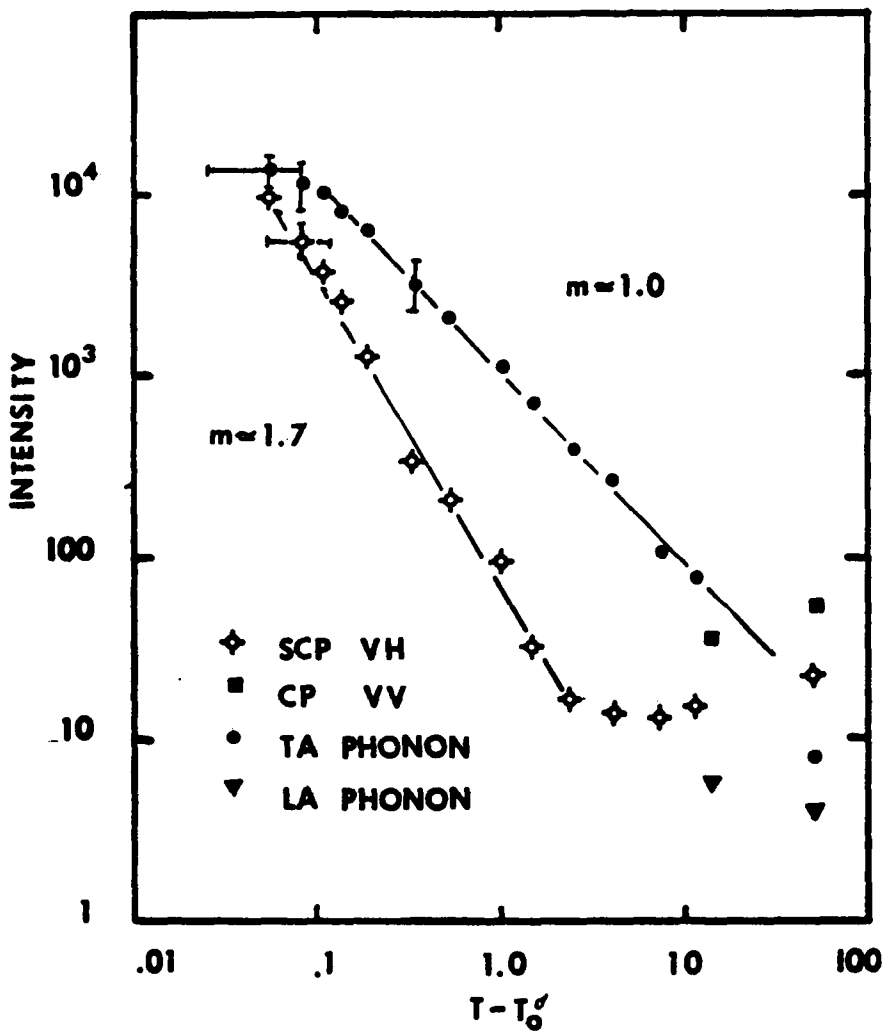

fig. VI-1 Integrated Intensities of the polarized and depolarized components of the Brillouin Scattering spectrum. In particular, the temperature dependence of the paraelectric Static Central Peak and the X_y shear mode intensities are shown. Intensities are in arbitrary units and measured relative to constant laser intensity.

The transition temperature was identified with .025°K precision as the temperature at which the Brillouin components suddenly move out from the central component, signalling the transition to the ferroelectric phase. The difference between T_o^σ and T_c, for the first order transition, is taken from the dielectric data of Western et al. [95] They found: $T_c - T_o^\sigma = 0.041 \pm 0.010°K$. (There is considerable discrepancy in the literature for this difference.)

For $T - T_o^\sigma \gtrsim 10°K$, the Rayleigh peaks for both the polarized and depolarized scattering are seen to increase as T increases. The relative intensities of these features with respect to the phonon modes and their apparent T^2 temperature dependence suggest that they may be due to normal dielectric coupling to the entropy fluctuations. [5] The L.A. phonons show some small, unexpected increase in intensity. For $T - T_o^\sigma < 10°K$ careful data exhibiting the growth in intensities of the Xy shear mode and static central peak are shown. For a large portion of the temperature range, both intensities grow as $(T - T_o^\sigma)^{-m}$ where $m \simeq 1.0$ for the T.A. phonon and $m \simeq 1.7$ for the SCP.

2) Electric field dependence

The electric field dependence of the SCP in the paraelectric phase was measured utilizing the spherical Fabry-Perot. Details of this experiment are discussed in Chapter VII in the section concerning the electric field dependence of the dynamic central peak. Electric field measurements of the SCP were previously done by Lagakos. However, the FPP interferometer used in his experiments was unable to separate the inelastic and elastic central peaks. [4, 96] Figure 2 is a plot of the SCP intensity as a function of electric field for several temperatures

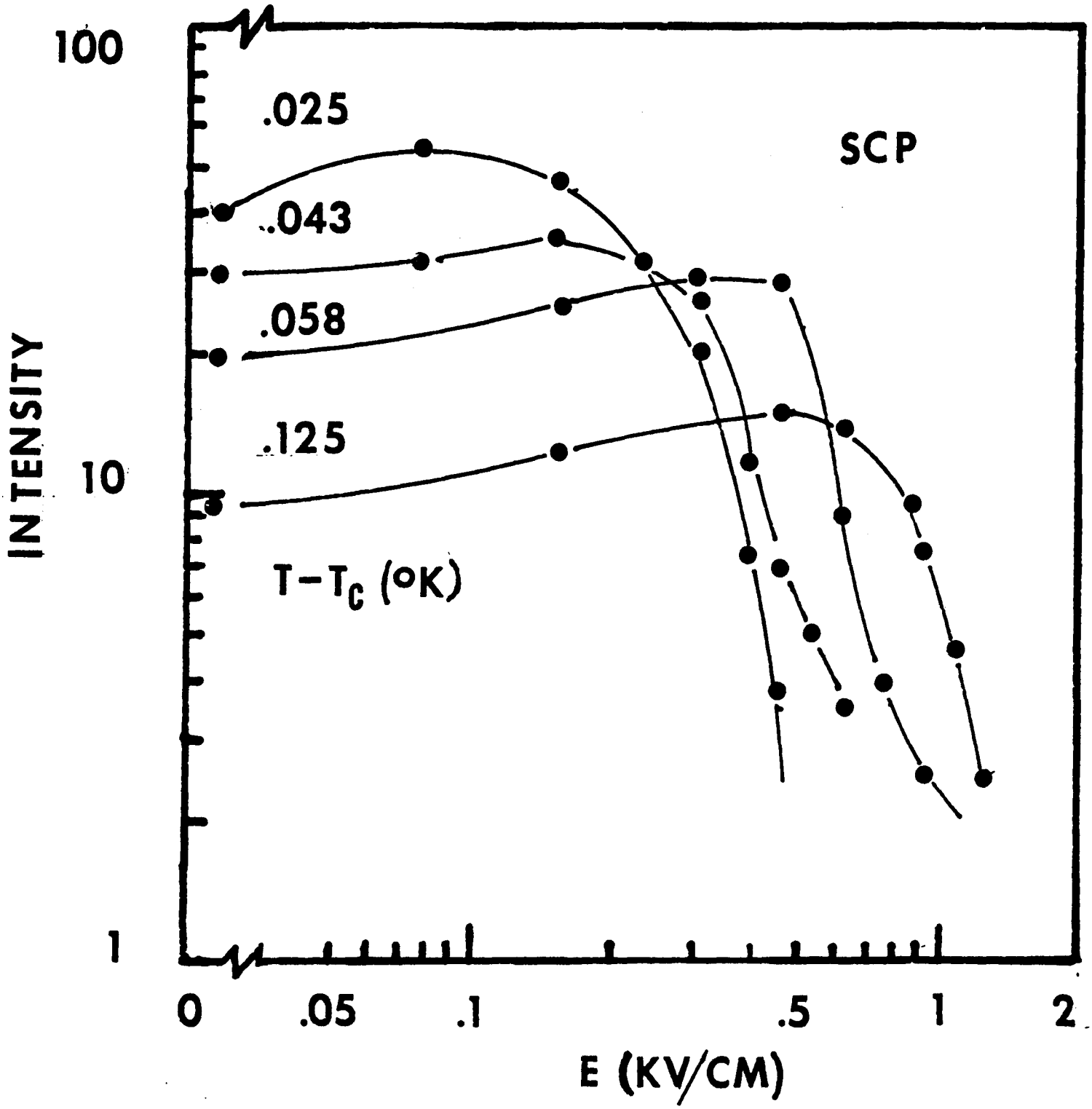

fig. VI-2 Electric Field dependence of the SCP integrated intensity for $T > T_c$. Integrated intensities are measured in arbitrary units and are relative to a constant laser intensity.

close to T_c. Notice that the intensity first increases with increasing electric field and then rapidly falls off. The peak intensity occurs at smaller electric fields for temperatures closer to T_c.

3) Sample dependence

Experiments on three crystals purchased from different firms exhibited a sample dependence in the intensity of the SCP. Data from two experiments are shown in figures 3 and 4. Both experiments were performed with identical experimental conditions. Figure 3 shows the T.A. phonon Brillouin intensity for KDP5 and KDP13 as a function of temperature. The measured transition temperature, at a laser power of 220 mW, for KDP13 was $T_c^{(13)} = 121.561 \pm .026°K$ and for KDP5 was $T_c^{(5)} = 121.661 \pm .030°K$ (for laser power corrections to T_c, see Appendix A). For $T > 121.8°K$ both crystals exhibit approximately the same Brillouin intensity for a given temperature, supporting the self-consistency of the two experiments. Near 121.7°K there appears to be some deviation in the Brillouin intensity. Fig. 4 is a semi-log plot of the SCP intensity vs temperature for the two crystals. Since the SCP intensity increases by approximately three orders of magnitude in the range $0 < T - T_c < 2°K$, the high temperature contribution to its total intensity is negligible close to T_c. Fig. 4 clearly shows that the SCP in KDP5 is significantly stronger than that of KDP13.

C. Interpretation

1) Axe Model

The experimental results concerning the SCP are interpreted in

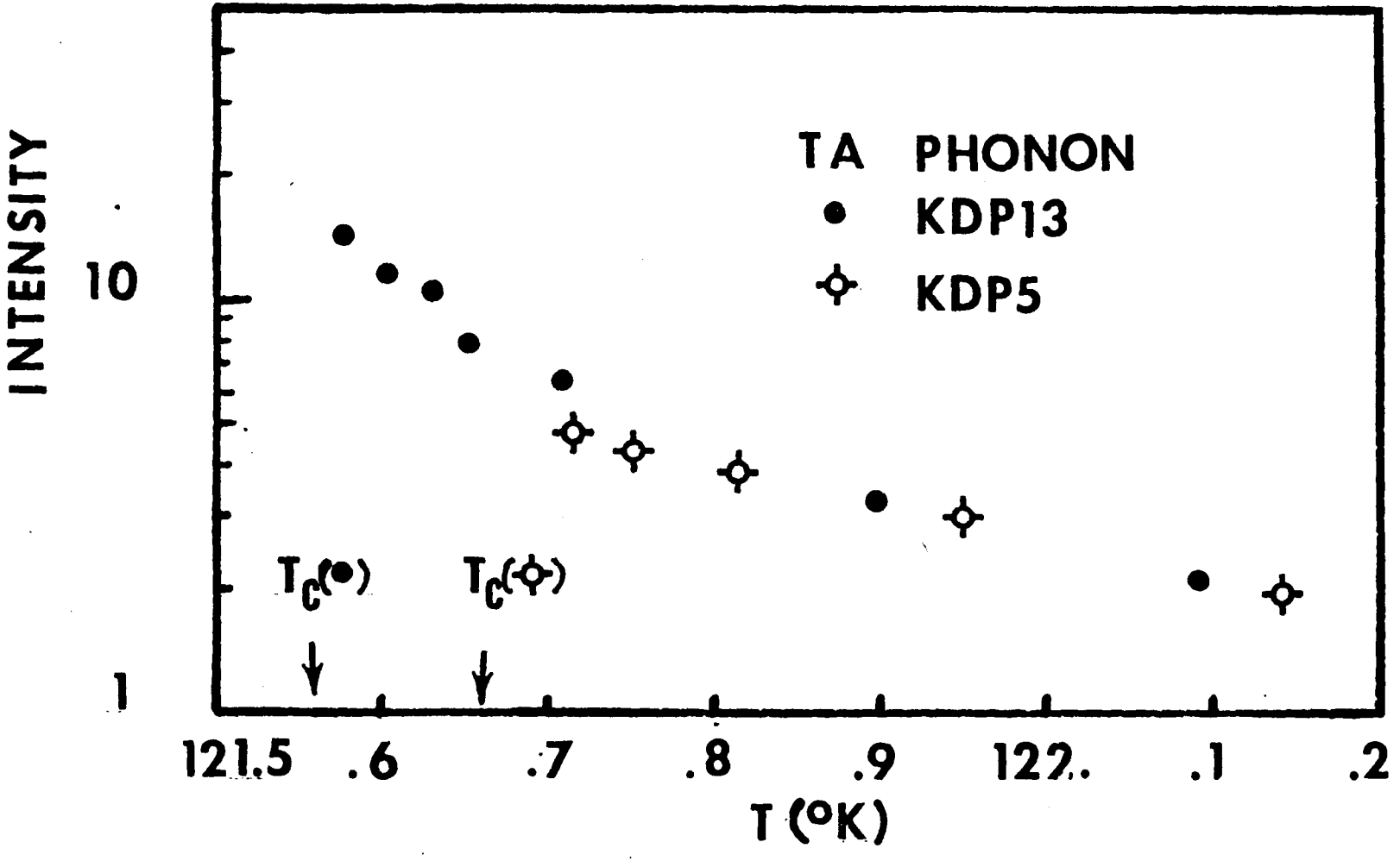

fig. VI-3 Integrated Intensities of the T.A. phonon in samples KDP13 and KDP 5. Intensities are in arbitrary units and are measured relative to the laser intensity.

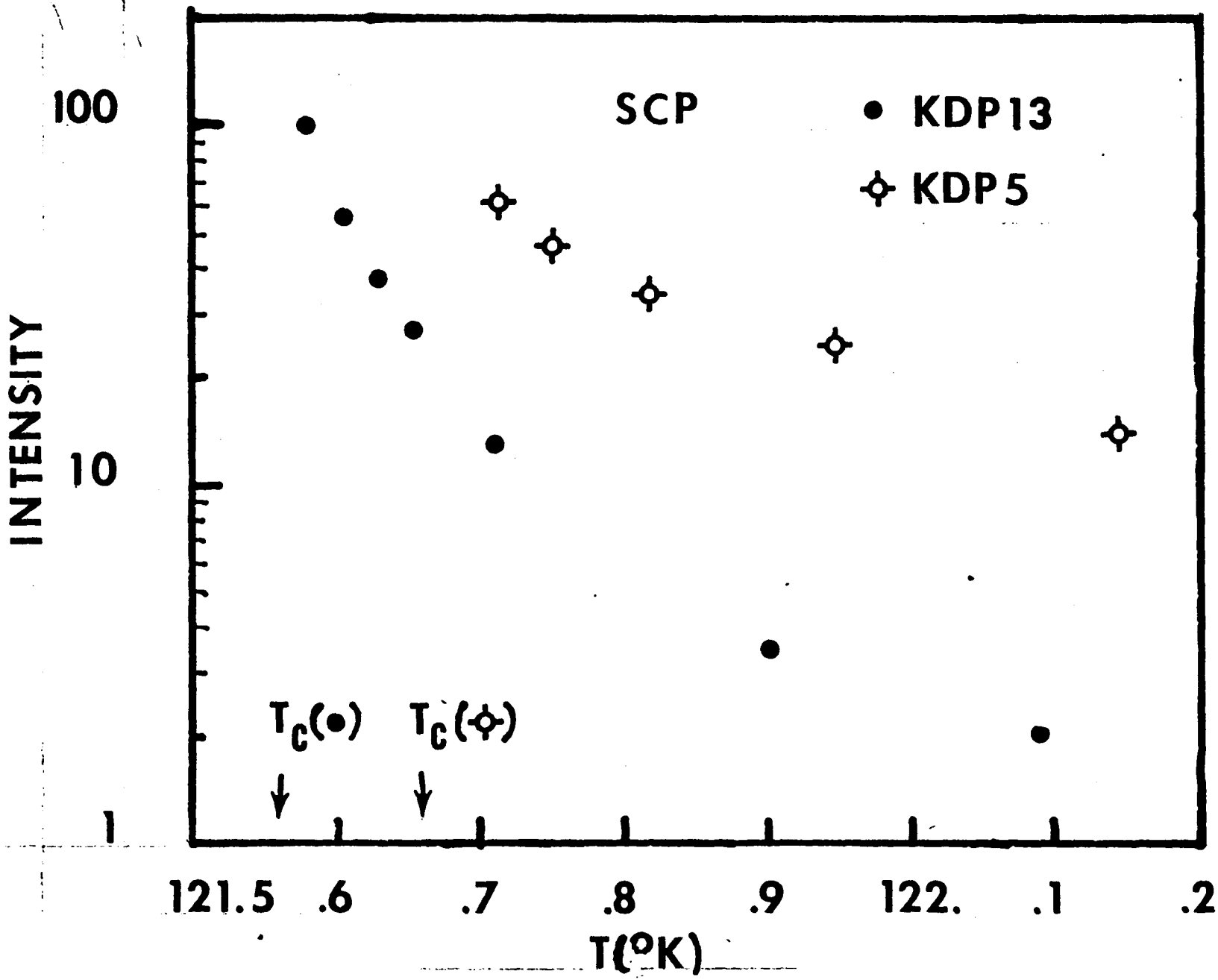

fig. VI-4 Integrated intensities of Static Central Peak in paraelectric phase for KDP13 and KDP5. Intensities are in arbitrary units and are measured relative to the laser intensity.

terms of the defect model due to Axe et al.[64,10] and the equivalent 'frozen defect' model of Halperin and Varma, [12] as discussed in chapter II. The presence of defects, in an otherwise perfect lattice, may induce static distortions in the x_6 shear strain. The amplitude of the strain is related to the Fourier component of the impurity-induced force field F_6 (q) by

$$(3) \qquad \langle x_6(q) \rangle = \frac{F_6(q)}{C_{66}^{E,T}}$$

where $C_{66}^{E,T}$ is the isothermal elastic constant associated with the Xy shear mode. The elastic constant is taken to be isothermal (rather than adiabatic) because any temperature gradient induced by a static distortion will be relieved by heat conduction, independent of the thermal phonon relaxation time.

(a) Temperature dependence

The intensity of the SCP is expected to grow as: $I_s \propto |\langle x_6 \rangle|^2$ so that its development is primarily governed by $C_{66}^{E.T}$:

$$(4) \qquad I_s \propto \frac{|F_6(q)|^2}{(C_{66}^{E,T})^2}$$

Equation (4) predicts that $I_s\ (C_{66}^{E,T})^2$ will be constant as a function of temperature. The Brillouin measurements determine the adiabatic elastic constant. However, $C^{E,T}$ and $C^{E,S}$ are expected to be the same in the paraelectric phase. [92] Fig. 5 is a plot of $I_s\ (C_{66}^{E,T})^2$ vs $(T - T_o^{\sigma})$ where I_s and $C_{66}^{E,T}$ are taken from the computer fit to the Brillouin

spectrum. Over the bulk of the temperature range this plot yields a horizontal line verifying the SCP temperature dependence predicted by (4)

(b) Electric field dependence

The electric field dependence of the isothermal elastic constant has been discussed in Chapter III (see figure III-12) and by Brody.[92] Application of an electric field in the paraelectric phase, close to the critical temperature, will initially cause an increase in the isothermal static susceptibility $\varepsilon^{\sigma,T}$. The isothermal elastic compliance $(C_{66}{}^{E,T})^{-1}$ will also exhibit a corresponding increase and the crystal will soften. As the electric field is increased further, the static susceptibility as well as the elastic compliance will decrease and the crystal will harden. These results, along with eq. (4) predict that the SCP intensity will first increase with increasing electric field, peak at the critical electric field and critical temperature, and then decrease. This behavior is shown in the experimental results of Fig. 2. The SCP electric field data indicate that:

$$T_{cr} - T_c < .043°K$$

$$E_{cr} < 154 \text{ V/cm}$$

More isothermal curves of I_s vs E closer to T_c are required to obtain a more accurate measurment of the critical temperature and electric fields as determined by $C_{66}{}^{E,T}$.

2) Non-linear Axe Model

(a) Elastic potential energy

Eq. (1) predicts that close to the transition temperature the

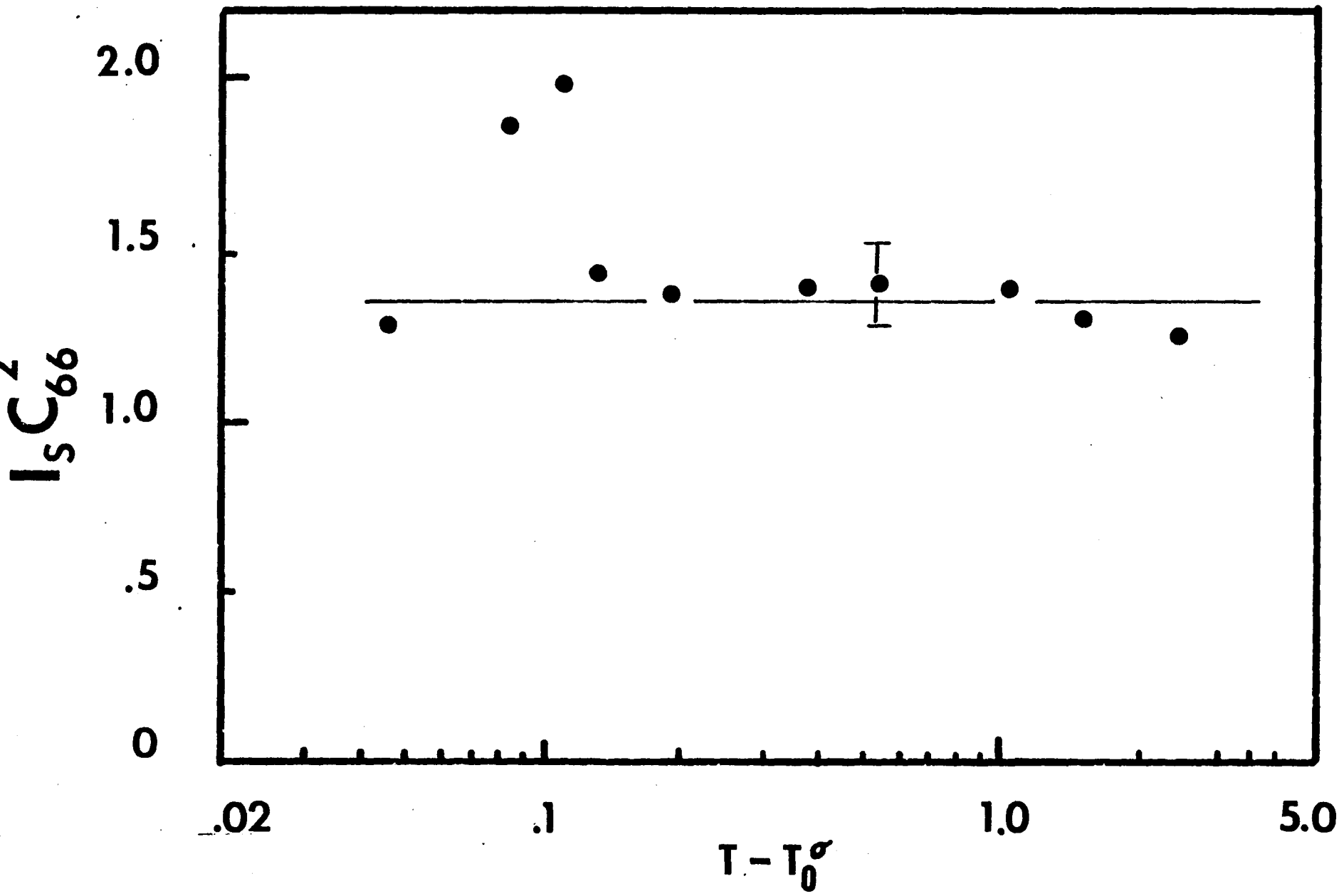

Fig. VI-5

static distortion in the strain coordinate will become very large. In this case it may be necessary to include the first anharmonic contribution to the phonon potential energy allowed by the crystal symmetry. The phonon potential energy would then be

$$V = \frac{1}{2} c_0 x^2 + \frac{1}{4} c_1 x^4 \tag{5}$$

where c_0 represents the harmonic elastic constant and c_1 represents the lowest order anharmonic contribution to the elastic potential energy. In equilibrium, the defect-induced force F can then be written as:

$$F = c_0 x + c_1 x^3 \tag{6}$$

Far from T_c, the non-linear contribution to the restoring force is expected to be negligible, in which case

$$\langle x \rangle \simeq \frac{F}{c_0} \tag{7}$$

However, close to T_c, c_0 approaches zero so that the non-linear effects dominate. We then have

$$\langle x \rangle \simeq \left(\frac{F}{c_1} \right)^{1/3} \tag{8}$$

Therefore, the static central peak intensity, which is proportional to $\langle x \rangle^2$, is expected to be determined by the softening of the C_{66} elastic constant as T_c is approached, and is then expected to saturate due to non-linear contributions to the restoring force. Other saturation mechanisms may be significant near T_c, such as interference of strain fields from neighboring defect sights.

(b) Effective Elastic Constant

The effective elastic constant c', which determines the acoustic

phonon frequency ω(T.A.), is determined from

$$(9) \qquad c' = \left(\frac{\delta F}{\delta x}\right)_{x=\langle x\rangle} = c_0 + 3c_1\langle x\rangle$$

Use of equations (7) and (8) yield

$$(10) \qquad c' = \begin{cases} c_0 + \dfrac{3c_1F}{c_0} & T > T_c \\ c_0 + 3(c_1^2F)^{1/3} & T \simeq T_c^+ \end{cases}$$

Although the linear elastic constant c_0 is nearly equal to zero at T_c (for a first order transition), the renormalized elastic constant c' will saturate at 3 $(c_1^2F)^{1/3}$.

These saturation effects were looked for in our experiments but were not seen. Presumably this is because the first-order transition occurs before c_0 becomes sufficiently small for the nonlinear terms to become significant.

D. Conclusion

In conclusion, the SCP in paraelectric KDP has been characterized in terms of its temperature and electric field dependence. The results have been compared to the static defect model of Axe et al. and of Halperin and Varma. It was found that a defect-induced static distortion in the x_6 shear strain can account for both the temperature and electric field dependence. A sample dependence to the SCP strength has been measured

in commercially available crystals. This observation is supportive of defect interpretations. Possible nonlinear effects to the SCP growth and the C_{66} elastic constant have been considered, however their presence has not been observed to within experimental error. Recently, Courtens [25] has shown that the SCP peak can be removed by annealing, strongly suggesting that this feature originates from lattice imperfections.

VII. Dynamic Central Peak - Experiment

A. Introduction

In 1977 a dynamic central peak (DCP), of width ~ 50MHz was observed in the depolarized light scattering spectrum of KH_2PO_4. The DCP peak, for zero electric field, is seen only in the ferroelectric phase within ~0.1 K of the transition. In this chapter I will present more extensive data characterizing the temperature and electric field dependence of the DCP intensity and linewidth. Our preliminary report of this new peak was published in Phys. Rev. B16, 2177 (1977). [5]

B. Experiment

1) General Procedure

The experimental configuration is the same as that employed to study the SCP and T.A. phonon, as discussed in chapter VI. However, the spectrum was analyzed with the 25 cm piezoelectrically scanned spherical Fabry-Perot interferometer (FPS). This interferometer has a free spectral range of 300 MHz and resolution of approximately 5 MHz.

2) Data Reduction

The FPS spectra, digitally recorded by the PDP-8E minicomputer, were analyzed by convoluting an experimentally measured instrument profile with a parameterized theoretical function and adjusting the parameters to produce a best nonlinear least-squares fit to the experimental data.

Our previous experiments established that for zero electric field the DCP appears only in the ferroelectric phase. [5] Furthermore, the static central peak, appearing in the paraelectric phase close to the transition is believed to result from a static defect mechanism [24] and

therefore exhibits no intrinsic linewidth. Therefore, it is convenient to experimentally determine the FPS instrument profile by measuring the strong SCP in the paraelectric phase close to T_c.

The parameterized theoretical spectral density function, $S(\nu)$, which we used to represent in the light scattering spectrum observed with the FPS is:

$$(1)\quad S(\nu) = A(T)\delta(\nu) + \frac{B\Gamma_c}{\nu^2+\Gamma_c^2} + B'$$

where ν is the frequency in Hertz.

The first term of (1) represents the temperature dependent SCP which also appears in the ferroelectric phase. B' is a temperature dependent background which includes the Brillouin components. The second term is a Lorentzian of halfwidth Γ_c representing the new DCP.

3) Temperature Dependence of the DCP Intensity and Linewidth

(a) Procedure

In this experiment the temperature dependence of the DCP intensity and linewidth, for zero electric field, was measured. The DCP appears in the temperature region: $0 \lesssim T_c - T \lesssim 0.1°K$ and its intensity is strongly temperature dependent close to T_c^-. Therefore the crystal was cooled to approximately $0.2°K$ below T_c and allowed to come to thermal equilibrium. The temperature was subsequently increased slowly (typically by 0.005 to 0.010 K increments) towards T_c. After each temperature incredment the crystal was allowed to come to thermal equilibrium as indicated by the thermometer. This would take typically 20-30 minutes. Once the temperature stabilized, three FPS spectra were taken over a period of about 10 min. to insure that the crystal had reached thermal equilibrium. This procedure was continued as T was gradually increased up through the transition. The transition temperature T_c was

taken to lie between the temperatures corresponding to the last spectra exhibiting the DCP and the first spectra with no DCP. The two principle features of the DCP spectra which lend themselves to analysis are the DCP intensity and linewidth. They are discussed below.

(b) Intensity

Figure 1 is a log-log plot of the DCP intensity as a function of $T_c - T$. Shown are the results of two separate experiments (78AS and 78AV) performed on the same crystal (KDP13) under identical experimental conditions. The intensities shown are in arbitrary units and are measured relative to a constant laser intensity as measured by a solar cell and strip chart recorder. Several nonlinear least-squares fitting runs, with different initial parameter values, were made on each of three spectra corresponding to a single temperature. The best fits for each of the three spectra were retained. The intensity error bars correspond to the standard deviation of the integrated intensities for these three fits.

The temperature error bars primarily result from the uncertainty in the determination of the transition temperature T_c. For experiments 78AS and 78AV the transition temperatures were determined with a precision of ±0.005°K and ±0.010°K respectively. Other contributions to the temperature error bars are due to the temperature controlling electronics and nitrogen dewar (see Chapter V) and laser heating effects (see Appendix A). The DCP intensity is seen to exhibit a logarithmic dependence. The intensity grows as $I_D \sim (T_c - T)^{-m}$ with $m \simeq 1.1$ for $0 \lesssim T_c - T \lesssim 0.1°K$.

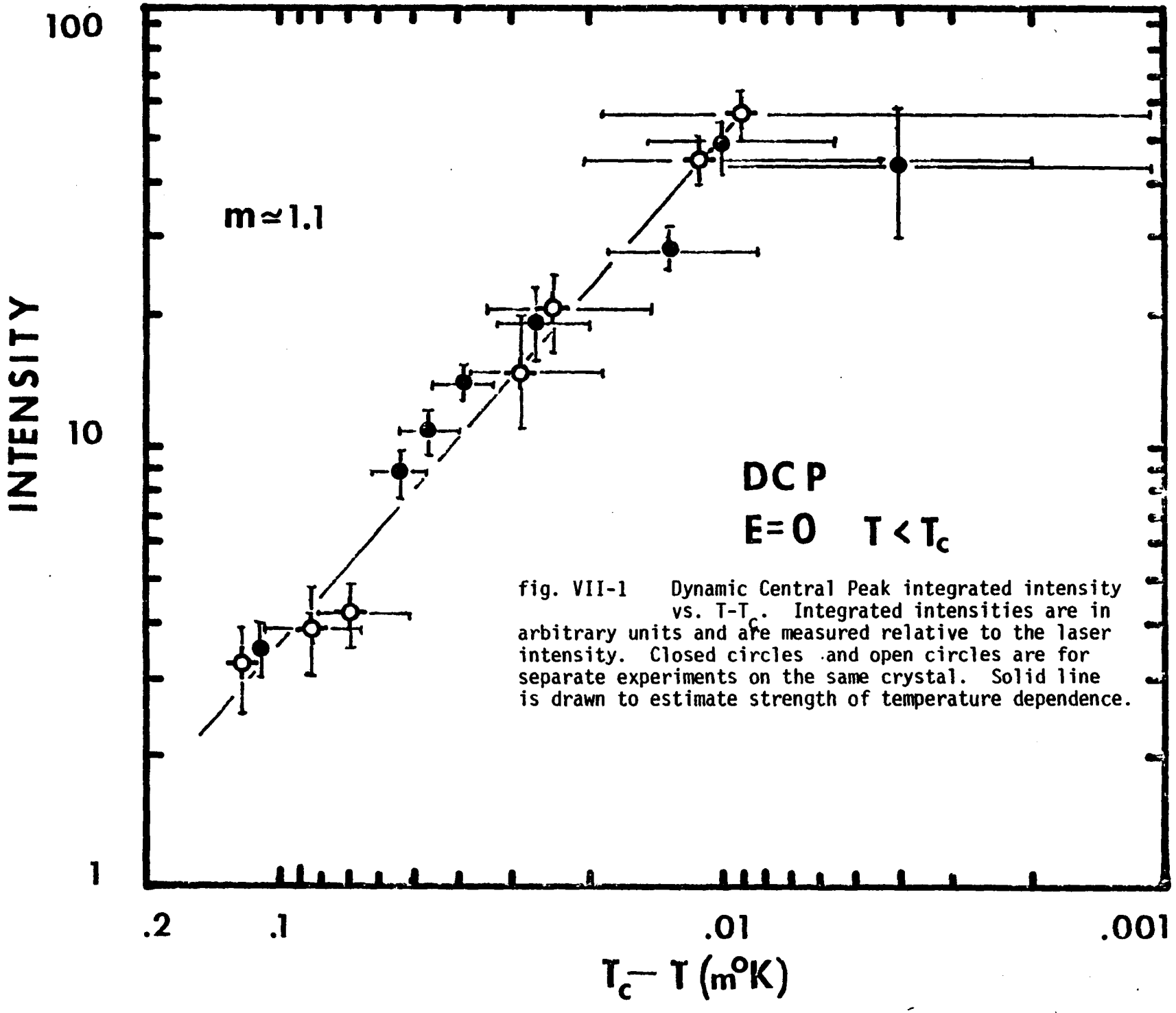

fig. VII-1 Dynamic Central Peak integrated intensity vs. $T-T_c$. Integrated intensities are in arbitrary units and are measured relative to the laser intensity. Closed circles and open circles are for separate experiments on the same crystal. Solid line is drawn to estimate strength of temperature dependence.

(c) Relative Intensity of the DCP and Xy Shear Mode

In a separate experiment, the Brillouin spectra of KDP was measured in the ferroelectric phase close to T_c with the FPP. The experimental procedure and data analysis were performed in the same manner as discussed in chapter VI for measurements of the SCP. From these measuremetns the integrated intensities of the Brillouin components, $2\bar{I}_B$ (corresponding to the T.A. phonons), and the combined intensity of the SCP and DCP ($I_c = I_S + I_D$) are obtained. (The FPP cannot separate the SCP and DCP). Again, these intensities are measured relative to a constant laser intensity. In Figure 2 the intensity of the Brillouin components in the ferroelectric phase are plotted as a function of $T_c - T$. Figure 3 is a plot of the SCP plus DCP intensity in the ferroelectric phase as a function of $T_c - T$.

Analysis of the experiments utilizing the FPS to measure the DCP intensity (78AS, 78AV discussed above) also yields values for the intensity ratio α of the SCP and DCP where $\alpha = \frac{I_S}{I_D}$. Figure 4 is a plot of α as a function of $T_c - T$. The error associated with α results from the error in I_S and I_D and is typically 20%. A smooth curve was drawn through the data points. This curve serves to calibrate the relative weights of the SCP and DCP. (It should be recalled that α is a sample dependent parameter since it is related to the defect-induced SCP). Having determined α the relative intensities of the DCP and Xy shear mode can be found from

$$\frac{I_D}{2\bar{I}_B} = \frac{1}{1+\alpha} \quad \frac{I_c}{2\bar{I}_B}$$

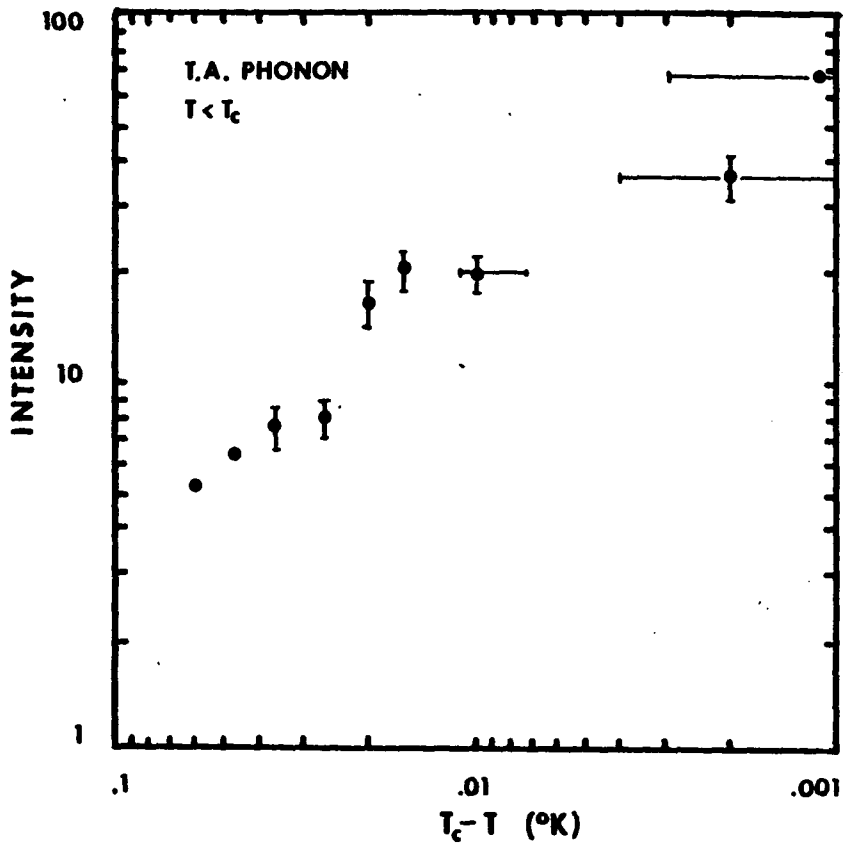

fig. VII-2 Integrated Intensity of the T.A. Phonon measured with FPP Interferometer in the Ferroelectric Phase close to T_c. Integrated Intensities are in arbitrary units and are measured relative to the laser intensity.

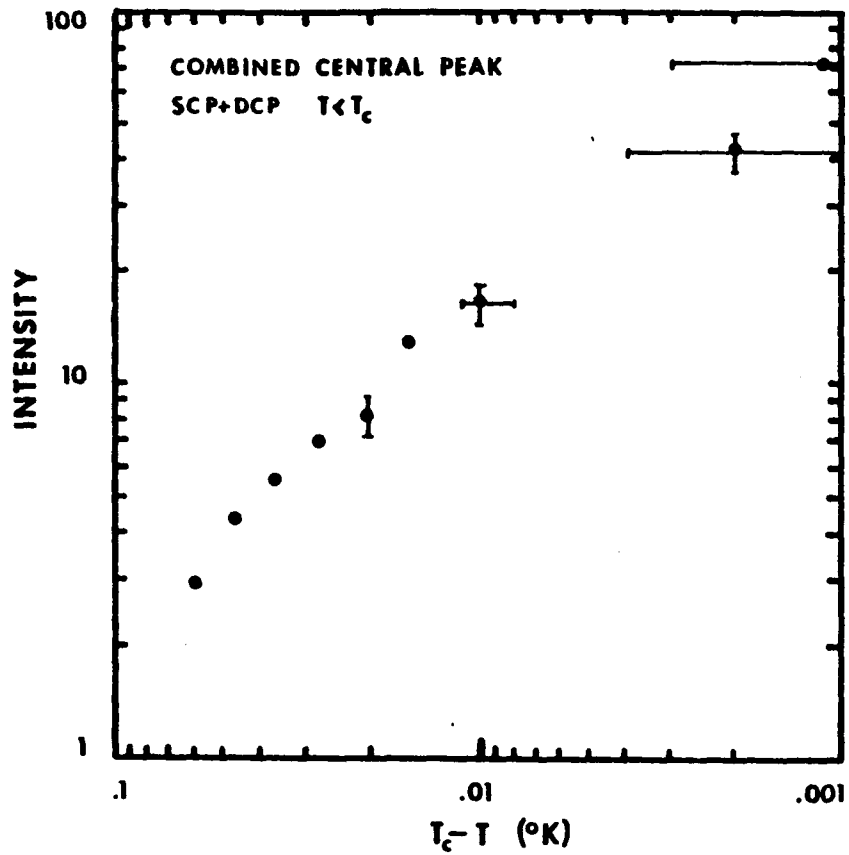

fig VII-3 Combined Static and Dynamic Central peak intensities measured with FPP interferometer in the ferroelectric phase close to Tc. Integrated intensities are in arbitrary units and are measured relative to the laser intensity.

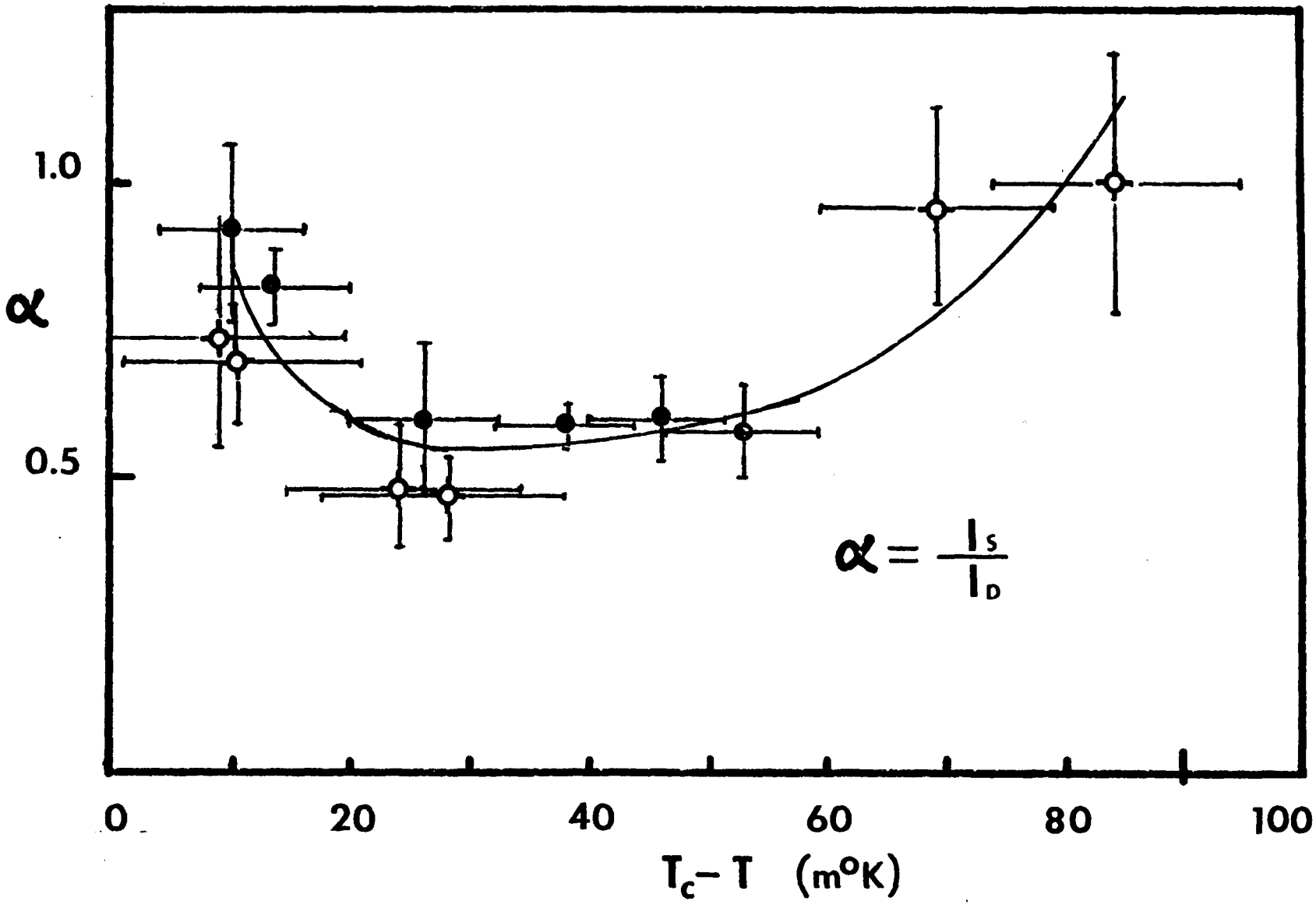

fig. VII-4 Relative integrated intensities of the static and dynamic central peaks, in the ferroelectric phase, close to T_c as measured by the FPS. Closed circles and open circles indicate separate experiments on the same crystal.

Table I lists the results of this experiment for $\frac{I_D}{2I_B}$:

Table I

$T_c - T$	α	$I_D/2I_B$
0.010	0.90±.2	4.5±.9
0.016	0.65±.1	4.0±.8
0.020	0.60±.1	3.3±.7
0.027	0.55±.1	5.7±1.1
0.036	0.55±.1	4.8±1.0
0.047	0.57±.1	4.4±.8
0.060	0.68±.1	3.4±.7

Errors in $\frac{I_D}{2I_B}$ are due to errors in α, I_C, and $2I_B$ and are estimated to be approximately 20%.

(d) DCP Linewidth

The computer fit of experiments 78AS and 78AV yields the DCP linewidth (fullwidth at half maximum, FWHM) as a function of $T_c - T$. Figure 5 is a plot of the DCP linewidth, $\Delta\nu_{FWH}$, vs $T_c - T$. For $0 \leq T_c - T \leq 0.1°K$, the linewidth lies in the range $55MHz \leq \Delta\nu_{FWHM} \leq 85$ MHz. Error bars for $\Delta\nu_{FWHM}$ and $T_c - T$ were obtained in the same manner as those for I_D. Except for the one data point closest to T_c, the linewidth exhibits a small decrease as T_c is approached.

4) Electric Field Dependence

In order to investigate the effect of an electric field on the

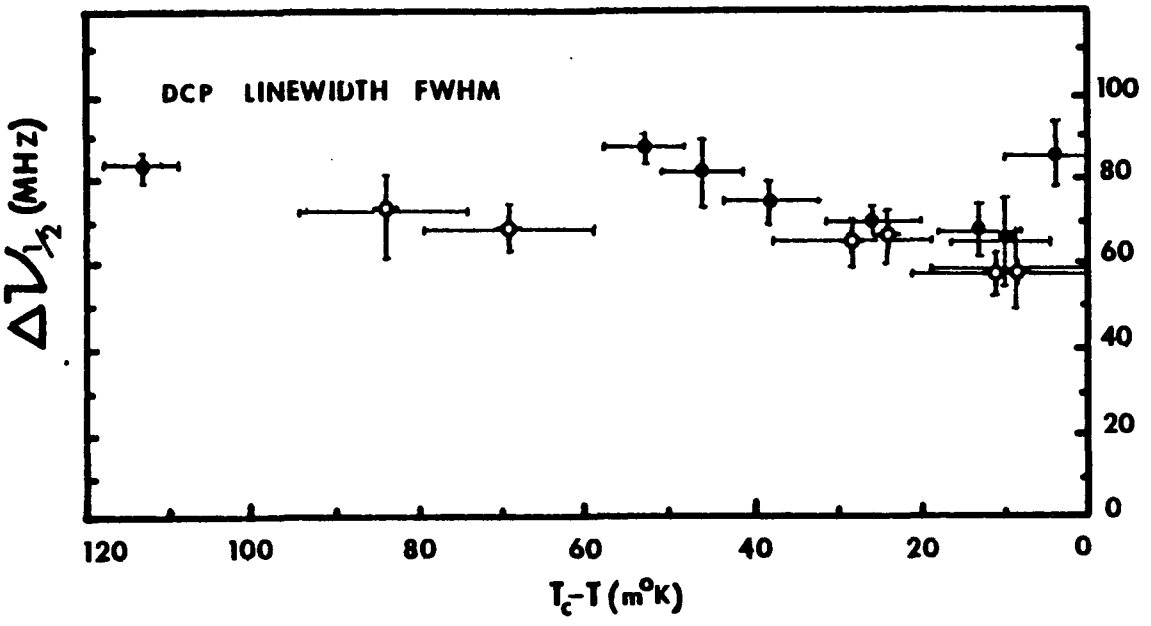

fig. VII-5 Dynamic Central Peak linewidth (full width at half maximum) measured in the ferroelectric phase close to Tc with E=0. Closed circles and open circles indicate seperate experiments on the same crystal.

DCP, the crystal was cooled to a temperature just above T_c. The transition temperature was determined in a previous run (78BF) with ±0.009°K precision. This was done by noting the temperature at which the DCP first appears upon cooling through the transition with E = 0. At a constant temperature, a voltage was applied to the silver paint electrodes on the z faces of the crystal. The application of an electric field to the crystal will cause a change in the crystal's temperature due to the electrocaloric effect. Therefore the crystal was allowed to come to thermal equilibrium with the temperature bath for 3-5 minutes. A safer waiting time would be 15-20 minutes. [88]

A plot of DCP intensity as a function of electric field is shown in Figure 6 for four temperatures close to T_c. The spectra were analyzed by the computer-assisted curve-fitting procedure, as discussed in chapter VI, for the spectral density (1). The DCP appears in the paraelectric phase with the application of an electric field. As the electric field is increased, the DCP intensity first increases and then decreases. The peak intensity increases as the temperature approaches T_c. There was no apparent electric field dependence to DCP linewidth.

C. Conclusion

In summary, the temperature and electric field dependence of the DCP has been characterized. The intensity, for E = 0, increases as T_c is approached from below the transition. This temperature dependence is well described by $I_D \sim (T_c - T)^{-m}$ with $m \simeq 1.1$. The intensity of the DCP is found to be typically five times greater than the combined intensity of the two Brillouin components associated with the Xy mode.

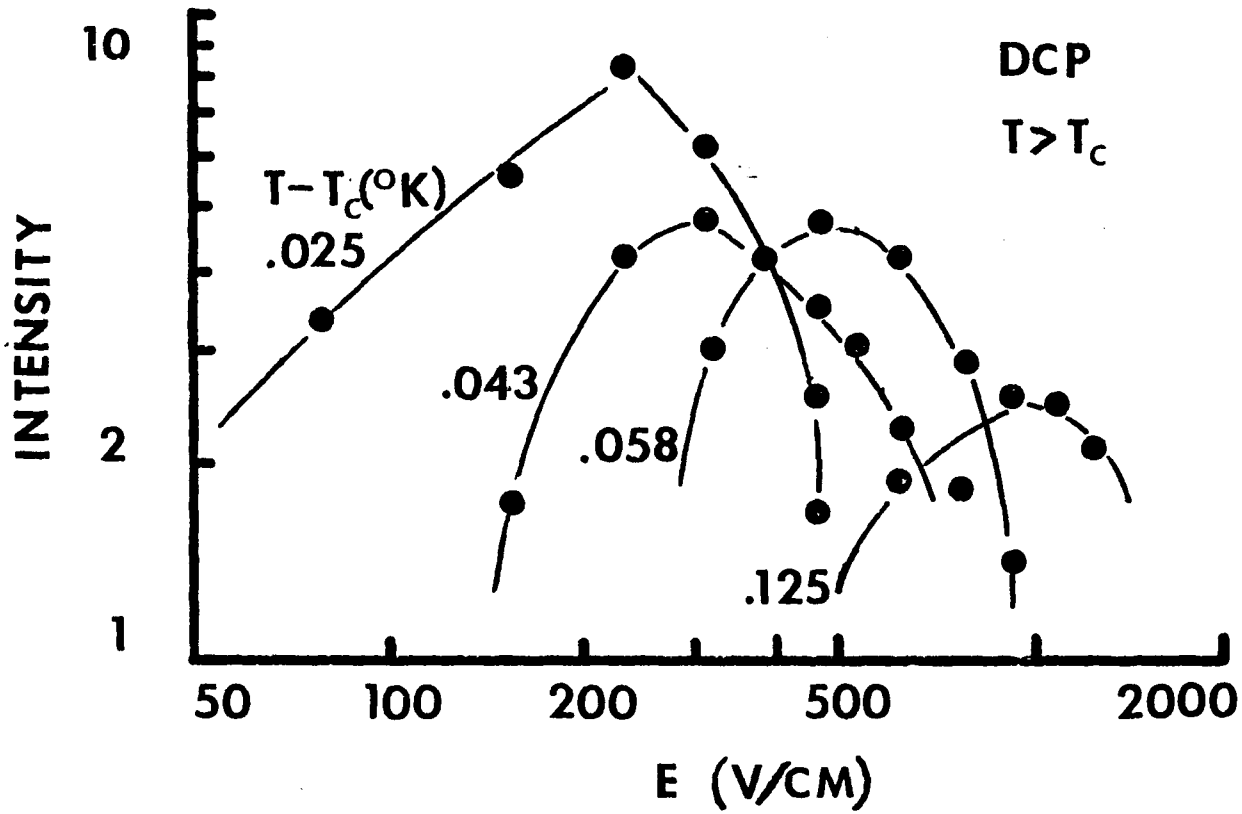

fig. VII-6 Integrated intensity of the dynamic central peak for $T > T_c$ in the presence of an electric field. Measurements were made with the FPS. Intensities are in arbitrary units and are relative to the laser intensity. Solid lines connect data points corresponding to a constant temperature.

The linewidth of the DCP was found to be in the range 55 MHz $\lesssim \Delta\nu \lesssim$ 85 MHz exhibiting little temperature dependence. However, a pronounced electric field dependence to the DCP intensity has been observed for the first time. These features will be discussed and interpreted in the following chapter.

Chapter VIII - Dynamic Central Peak - Interpretation

I. Introduction

The presence of a dynamic central peak in the ferroelectric phase close to the transition temperature is understood to result from the interaction of the thermal diffusion mode and the ferroelectric soft mode due to the temperature dependence of the spontaneous polarization.[5] In this chapter the temperature and electric field dependence of the DCP intensity and linewidth, as presented in chapter VII, are interpreted. The analysis of the intensities can be most easily accomplished via thermodynamic fluctuation theory which leads to predictions that can be evaluated using the extensive thermodynamic data available for KDP. A two-coupled mode picture (where the thermal diffusion mode and ferroelectric soft mode are coupled via the spontaneous polarization) leads to a prediction for the DCP linewidth that can be compared with experiment.

II. Intensity Analysis

A. DCP Intensity, E = 0

The intensity of light scattered by thermodynamic fluctuations in condensed matter is conveniently represented by the Rayleigh ratio (differential cross section per unit volume) as developed in Chapter II:

$$R = \frac{\pi^2}{\lambda^4} V \langle (\hat{e}_s \cdot \delta\varepsilon_q^{\alpha\beta} \cdot \hat{e}_o)^2 \rangle \qquad (1)$$

where λ is the wavelength of the incident light in the medium, V is the scattering volume, $\hat{e}_o$ and $\hat{e}_s$ are unit polarization vectors of the incident and scattered light, and $\delta\varepsilon_q^{\alpha\beta}$ is the qth Fourier component of the fluctuation in the $\alpha\beta$ component of the dielectric tensor.

The relevant dynamical variables for this problem, that induce $\delta\varepsilon_q^{\alpha\beta}$, are the polarization P_3, the X_y shear strain x_6, and the entropy S. If the

frequency ranges of the dynamical modes are well separated, $\delta\varepsilon_q^{\alpha\beta}$ can be separated into distinct contributions from each mode and the total intensity for that mode can be predicted from equation (1).

The mean square fluctuation in the dielectric constant, occurring at constant stress σ and electric field E, associated with the entropy is:

$$< (\delta\varepsilon_q^{\alpha\beta})^2> = (\frac{d\varepsilon_q^{\alpha\beta}}{dS})^2_{\sigma,E} <S_q^2> \qquad (2)$$

where $<S_q^2>$ is the mean square entropy fluctuation. Equation (2) reduces, via standard thermodynamic relations, to:

$$< (\delta\varepsilon_q^{\alpha\beta})^2 > = \frac{1}{V} (\frac{d\varepsilon_q^{\alpha\beta}}{dT})^2_{\sigma,E} \quad \frac{kBT^2}{\rho C_{\sigma,E}} \qquad (3)$$

where $C_{\sigma,E}$ is the specific heat per unit mass.

Since entropy fluctuations occur very slowly compared to the characteristic time of P_3 and x_6, we assume that the spontaneous polarization P_3 and shear strain x_6 remain in thermodynamic equilibrium with S. Then,

$$(\frac{d\varepsilon_q^{\alpha\beta}}{dT})_{\sigma,E} = (\frac{\partial\varepsilon_q^{\alpha\beta}}{\partial T})_{x,P} + (\frac{\partial\varepsilon_q^{\alpha\beta}}{\partial x})_{T,P} (\frac{dx}{dT})_{\sigma,E} + (\frac{\partial\varepsilon_q^{\alpha\beta}}{\partial P_3})_{T,x} (\frac{dP_3}{dT})_{\sigma,E} \qquad (4)$$

Equation (4) expresses the optical coupling to the thermal diffusion mode. The first term on the right hand side of eq (4) represents both direct and indirect (due to thermal expansion) components to the temperature dependence of $\varepsilon_q^{\alpha\beta}$. The two new terms represent additional indirect optical coupling via the temperature dependence of the spontaneous polarization (pyroelectric effect) and the temperature dependence of the spontaneous strain (thermal dilation effect).

The 'normal term', $(\frac{\partial\varepsilon_q^{\alpha\beta}}{\partial T})_{x,P}$, is only expected to occur in diagonal polarization, although anisotropy of the thermal expansion coefficient may induce depolarized scattering.[97] Its value above and below the transition can be estimated from the refractive index measurements of Yamazaki and Ogawa,[98]

$$(5)\qquad \left(\frac{\partial \varepsilon}{\partial T}\right)_{x,P} = \begin{cases} 1\times10^{4}\ (^{\circ}K^{-1}) & T>T_c \\ 4\times10^{4}\ (^{\circ}K^{-1}) & T<T_c \end{cases}$$

The second and third terms of eq (4) vanish in the paraelectric phase since the time average vablues of $x_6(T)$ and $P_3(T)$ are both zero for $T > T_c$. In the ferroelectric phase, the polarization contribution can be expressed in terms of the pyroelectric coefficient $\tilde{p}^{\sigma,E}$ and the electroptic coefficient ρ_{63}^{x}. The spontaneous strain term is expresssed by the thermal dilatation coefficient $\tilde{q}^{\sigma,E}$ and the elastooptic coefficient ρ_{66}^{P}. The complete temperature dependence of the dielectric constant, in the ferroelectric phase, can then be expressed as:

$$\frac{d\varepsilon}{dT} = \begin{cases} \left(\frac{\partial \varepsilon}{\partial T}\right)_{x,P} & \text{Normal Optical Coupling} \\ n_o^4 \rho_{63}^{x} \tilde{p}^{\sigma,E} + n_o^4 p_{66}^{P} \tilde{q}^{\sigma,E} & \text{"New Indirect Optical Coupling"} \end{cases} \qquad (6)$$

The pyroelectric and thermal dilatation coefficients have been determined theoretically from the Helmholtz free energy in chapter III and are given by eqs 22 and 23. Figure 1 is a plot of these three contributions to the temperature dependence of the optical dielectric constant in the ferroelectric phase as estimated from the Benepe-Reese free energy. Note that it is the polarization term that dominates the dielectric constant temperature dependence. Retaining only the polarization contribution, the Rayleigh ratio for the thermal diffusion mode can be expressed as:

$$R_{VH}(T.D.) = \frac{\pi^2}{2\lambda^4} n_o^8 \rho_{63}^{x} (\tilde{p}^{\sigma,E})^2 \frac{k_B T^2}{\rho C_{\sigma,E}} \qquad (7)$$

The solid line in Fig (2) is the Rayleigh ratio, determined by eq(7) and the Benepe-Reese free energy. Values for the specific heat are taken from Reese and May.[99] Also shown in Fig 2 are the experimental data whose intensity has been scaled to coincide with the data point at $T_c - T = 0.028^{\circ}K$. Hence the Rayleigh ratio (2) yields a good description for the temperature

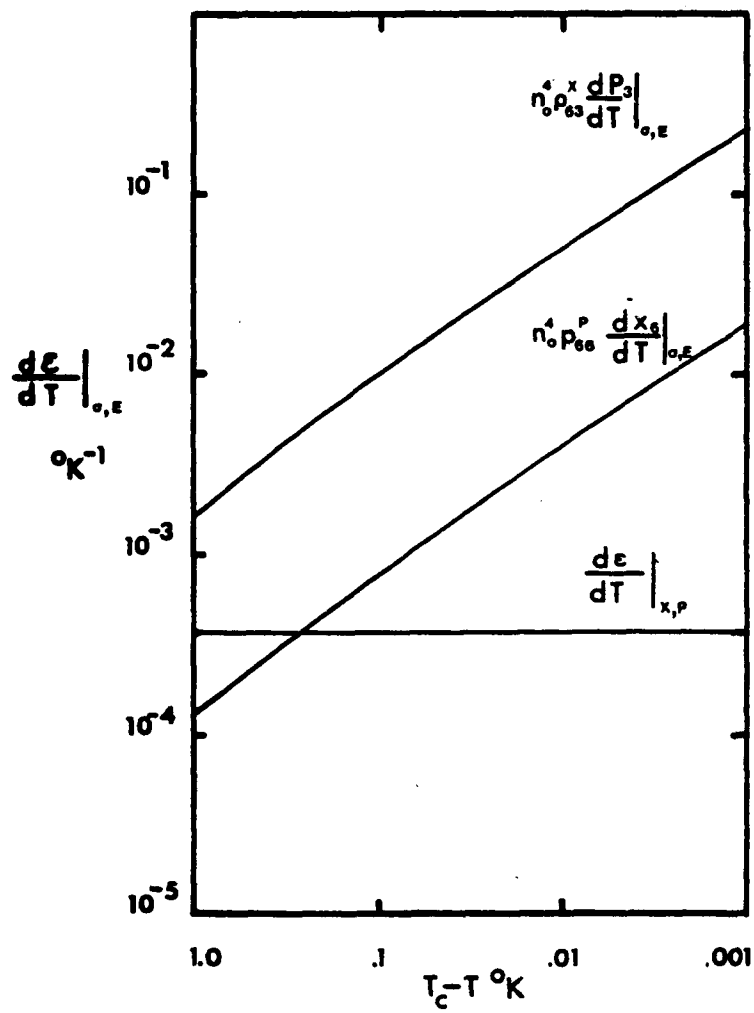

fig. VIII-1 Estimates to the temperature dependence of the optical dielectric constant showing the 'normal temperature dependence' plus the two new indirect terms resulting from the temperature dependence of spontaneous polarization and strain in the ferroelectric phase. Note that it is the polarization term that dominates near T_c.

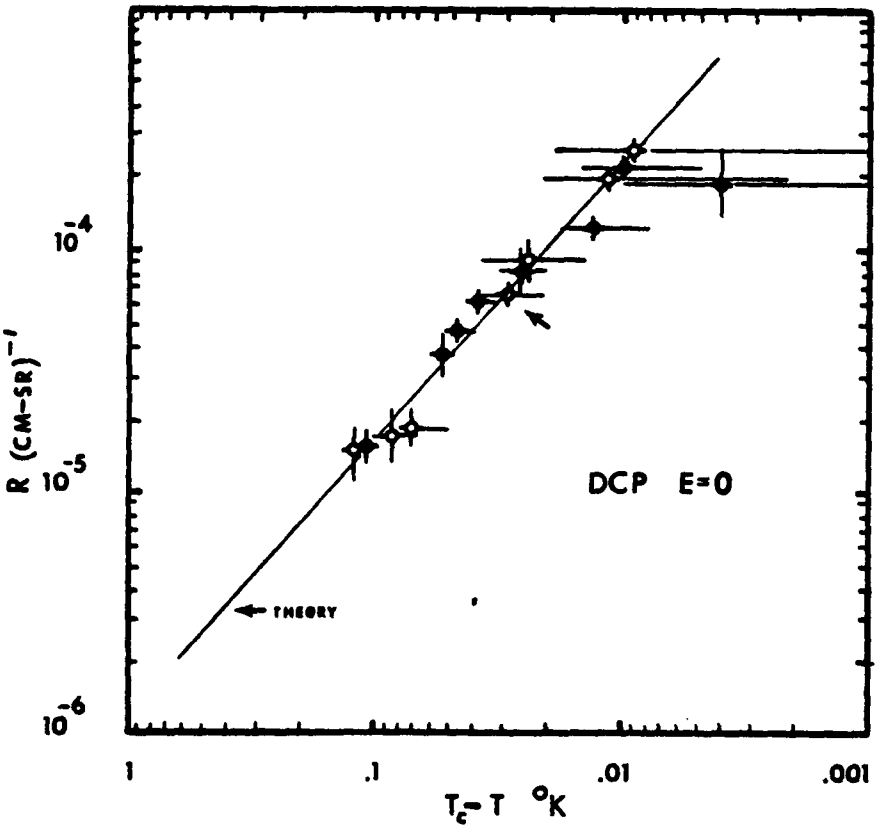

fig. VIII-2 Solid line indicates thermodynamic prediction for the scattering cross section per unit volume expressed by equation 7. Integrated intensity data of fig. VII-1 have been rescaled to match the prediction at $T=Tc+0.028$ °K indicated by arrow.

dependence of the thermal diffusion mode.

B. Relative Intensities of DCP and X_y Shear Mode

In chapter VII an experimental determination of the intensity ratio of the DCP and T.A. acoustic phonon was made and its values were tabulated in Table I. A theoretical estimate of this ratio can be made from the thermodynamic analysis utilizing eq. (1) for the scattering cross sections per unit volume of the X_y shear mode and the thermal diffusion mode. The Rayleigh ratio for the thermal diffusion mode is given by (7). The Rayleigh ratio for the T.A. phonon in the ferroelectric phase is found to be: [100]

$$R(T.A.) = \frac{\pi^2}{4\lambda^4} n_o^8 (p_{66}^{E,S}) \frac{k_B T}{C_{66}^{E,S}} \tag{8}$$

The adiabatic Pockels' coefficient, $p_{66}^{E,S}$, can be expressed as: [101]

$$p_{66}^{E,S} = p_{66}^{P} + \rho_{63}^{X} a_{36} \left[\frac{\varepsilon^{X,S}}{4\pi}\right] \tag{9}$$

The Pockels' coefficient can then be estimated from the known values of p_{66}^{P}, ρ_{63}^{X}, and a_{36} along with the B-R free energy prediction for the susceptibility $\varepsilon^{X,S}$. The intensity ratio is

$$\frac{R\ (T.D.)}{2R\ (T.A.)} = \left(\frac{\rho_{63}^{X}}{p_{66}^{E,S}}\right) \frac{T\, C_{66}^{E,S}\, (\tilde{p}^{\sigma,E})^2}{\rho\, C_{\sigma,E}} \tag{10}$$

This intensity ratio has been evaluated using the B-R free energy and the specific heat data of Reese and May [99] (taking $T_p = T_c$). The results of this calculation, along with the experimental results of chapter VII, are shown in Table I.

In view of the manner in which these experiments were done and the associated error, the agreement between theory and experiment is viewed to be reasonably good.

TABLE I

$T_c - T$	$\frac{I_D}{2I_B}$	$\frac{R\ (T.D.)}{2R\ (T.A.)}$
0.010	4.5 ± .9	24.2
0.016	4.0 ± .8	18.2
0.020	3.3 ± .7	17.0
0.027	5.7 ± 1.1	18.4
0.036	4.8 ± 1.0	10.6
0.047	4.4 ± .8	9.0
0.060	3.4 ± .7	7.2

C. Electric Field Dependence to the DCP Intensity

Application of an electric field along the axis of the spontaneous polarization will cause a distortion of the phase transition. A small electric field ($E < E_{cr}$) will cause some rounding of the onset of the polarization. Furthermore, the polarization will now increase discontinuously at a temperature above the transition temperature. A large electric field ($E > E_{cr}$) will smooth the development of polarization so that, upon cooling, there will be no discontinuous jump. This jump in P will vanish when $E = E_{cr}$. These effects are illustrated in Fig. 3 of chapter III. Therefore, the polarization response to temperature fluctuations will have a marked electric field dependence. This is illustrated in Fig. 8 of chapter III where the pyroelectric coefficient $\tilde{p}^{\sigma,E}$ is plotted as a function of electric field for several temperatures close to T_c in the paraelectric phase. The Rayleigh ratio for the thermal diffusion mode, given by eq. (7), is seen to be proportional to $(\tilde{p}^{\sigma,E})^2$. Therefore, the electric field dependence of the scattering cross section is expected to be dominated by the electric field dependence of $\tilde{p}^{\sigma,E}$. It is assumed that the electric field dependence of the index of refraction and specific heat will be minor. This electric field dependency of $\tilde{p}^{\sigma,E}$ is to be compared with the experimental results presented in Fig. VII-6. There is good qualitative agreement between the experimental data and the thermodynamic results. Hence, the intensity of the thermal diffusion mode can be used as a probe to investigate the thermodynamic properties of KDP, via the pyroelectric susceptibility, which is related to the static isothermal dielectric susceptibility by

$$\tilde{p}^{\sigma,E} = -\varepsilon^{\sigma,T} \frac{P}{C}$$

The approach to the critical point at atmospheric pressure, as well as the approach to the line of second order phase transition for differing amounts of pressure, can be well monitored by the thermal diffusion mode intensity. As the point(s) of a second order transition are approached the intensity of the T.D. mode should increase to values greater than those achieved at atmospheric pressure and zero electric field.

III. Coupled Mode Analysis

A. Linewidth Renormalization

We have interpreted the DCP as the low frequency structure to the ferroelectric soft mode resulting from its coupling to the thermal diffusion mode. This coupling is due to the extreme temperature dependence of the order parameter, the spontaneous polarization P_s. The thermal diffusion mode can be represented by a relaxational response function leading to a two-coupled-mode picture with an effective bilinear coupling between the soft mode (A) and the thermal diffusion mode (B). The spectrum is given by (as formulated in Chap. IV):

$$I(\omega) \alpha \text{ Im} \sum_{i,j=A,B} P_i P_j \chi_{ij}(\omega) \tag{11}$$

where P_A and P_B are the optical coupling constants and χ_{ij} are solutions of the matrix equation

$$\begin{pmatrix} (\chi_A^\circ)^{-1} & \Delta^2 \\ \Delta^2 & (\chi_B^\circ)^{-1} \end{pmatrix} \cdot \begin{pmatrix} \chi_{AA} & \chi_{AB} \\ \chi_{BA} & \chi_{BB} \end{pmatrix} = \begin{pmatrix} 1 & 0 \\ 0 & 1 \end{pmatrix} \tag{12}$$

χ_A° amd χ_B° are the response functions of the uncoupled ferroelectric soft mode and entropy mode and are given by

$$\chi_A^\circ = (\omega_\infty^2 - \omega^2 \; i\omega\Gamma_A)^{-1} \tag{13a}$$

$$\chi_B^\circ = c\,(1 - i\omega\tau)^{-1} \tag{13b}$$

If we assume that $P_B = 0$ so that only the ferroelectric mode couples to the light, then

$$I(\omega) \sim P_A^2 \, Im \frac{\chi_A^0}{1 - \chi_A^0 \chi_B^0 \Delta^4} \tag{14}$$

which together with eqs (13) yields

$$I(\omega) \sim P_A^2 \, Im \frac{1}{\omega_\infty^2 - \omega^2 - i\omega\Gamma_A - \frac{c\Delta^4}{1 - i\omega\tau}} \tag{15}$$

This result is one of a number of equivalent expressions frequently used to represent the combined soft mode plus central peak spectrum (see Chap. II).

For the case of a heavily overdamped soft mode ($\Gamma_A >> \omega_\infty$) the spectrum of eq (15) separates approximately into two Lorentzians, the soft mode of width $\Gamma_s = \frac{\omega_\infty^2}{\Gamma_A}$ and intensity proportional to $\frac{1}{\omega_\infty^2}$, and the central peak of width $\Gamma_c = \left(\frac{\omega_0}{\omega_\infty}\right)^2 \frac{1}{\tau}$ and intensity proportional to $\frac{c\Delta^4}{\omega_0^2 \omega_\infty^2}$. The total intensity is proportional to $\frac{1}{\omega_0^2}$ where $\omega_0^2 = \omega_\infty^2 - c\Delta^4$ determines the static susceptibility. The high frequency susceptibility is given by ω_∞^2. The central peak linewidth is then

$$\Delta\nu_{FWHM}(DCP) = \eta^2 \left(\frac{1}{\pi\tau}\right) \tag{16}$$

with

$$\eta^2 = \left(\frac{\omega_0}{\omega_\infty}\right)^2 = \frac{1}{1 + \left(\frac{\delta}{\omega_0}\right)^2} \tag{17}$$

where $\delta^2 = c\Delta^4$.

Note that the DCP linewidth is not determined soley by the T.D. mode relaxation time but includes a linedth renormalization coefficient η^2. Because the modes are linearly coupled through the pryrolectric effect, we expect that

$$\delta = \delta_0 \, \tilde{\rho}^{\sigma, E} \tag{18}$$

At this point it is perhaps worthwhile to consider several possible interpretations of eq. (16).

1. Second Order Transition

For a second order transition, the central peak linewidth should approach zero at T_c, even if τ is temperature independent, since ω_o^2 goes to zero at T_c while ω_∞^2 remains non-zero due to the mode coupling.

2. First Order Transition

For a first order transition, the static susceptibility does not approach zero as T_c is approached from below. Therefore narrowing of the DCP, as discussed for a second order transition is not expected to occur. However, the DCP linewidth may or may not approach zero at T_c depending upon the relative magnitude of δ and ω_o very close to T_c^-. We can consider two cases:

a. $$\left[\frac{\delta}{\omega_o}\right]_{T\simeq T_c^-} << 1$$

In this case the linewidth renormalization coefficient, η^2, is given by

$$\lim_{T\to T_c^-} \eta^2 = 1$$

The renormalization coefficient is equal to 1 so that the DCP linewidth is indistinguishable from the thermal diffusion mode linewidth .

b. $$\left(\frac{\omega_o}{\delta}\right)^2_{T\simeq T_c} << 1$$

In this case the renormalization coefficient, close to T_c^-, can be approximated by:

$$\lim_{T\to T_c^-} \eta^2 = \left(\frac{\omega_o}{\delta}\right)^2$$

Although ω_o does not go to zero at T_c (for the first order transition) the anomalous behavior of δ, due to the pyroelectric effect, may cause a narrowing of the linewidth. These possible temperature dependences to the renormalization coefficient are illustrated below.

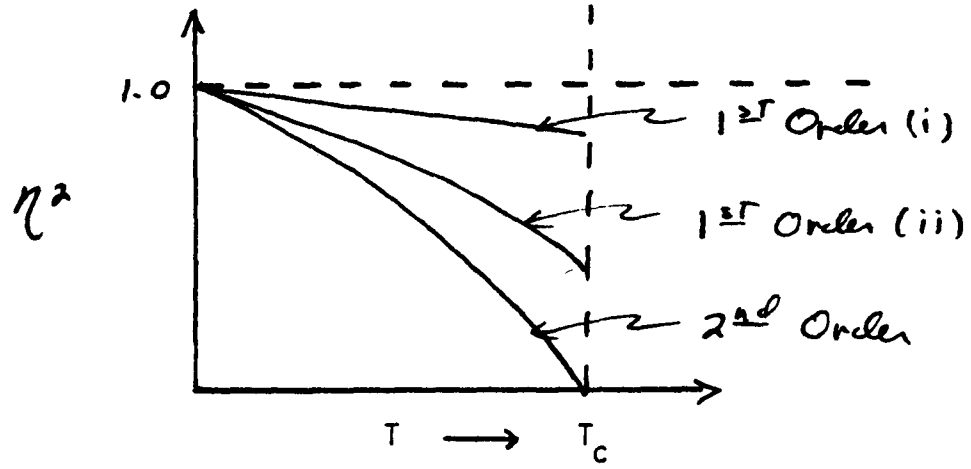

KDP undergoes a first order transition. Utilizing an intensity analysis of the DCP and ferroelectric soft mode, we have previously estimated that the smallest value of η^2 is $\eta^2|_{T=T_c^-} \simeq 0.99$.[5] This suggests that for KDP the applicable situation is that of case (a) for the first order transition. However, a quantitative evaluation of η^2 would be helpful in determining whether this renormalization resulting from pyroelectric coupling is inaccessible, in principle, for the first order transition at atmospheric pressure.

It is known that application of hydrostatic stress will force the transition to become second order, in which case the linewidth renormalization should become evident.[103,104,105]

B. Electric Field Effects and Linewidth Renormalization

Since the static dielectric susceptibility and the pyroelectric susceptibility both have a strong electric field dependence, I would expect that the renormalization coefficient, η^2, would exhibit a strong electric field

effect. In order to make some qualitative statements about this possible electric field dependence, I note that ω_o^2 is inversely proportional to $\varepsilon^{\sigma,T}$ and that δ is proportional to $\varepsilon^{\sigma,T}$. Taking

$$\omega_o^2 = \frac{\Omega_o^2}{\varepsilon^{\sigma,T}}$$

$$\delta = \delta_o \tilde{p}^{\sigma,T} = \delta_o'(E,T)\varepsilon^{\sigma,T}$$

where $\delta_o' = \delta_o \frac{P(E,T)}{C}$ I have

$$\eta^2 = \frac{1}{1 + \left[\frac{\delta_o'}{\Omega_o}\right]^2 (\varepsilon^{\sigma,T})^3} \tag{20}$$

Hence $\eta^2 = \eta^2(E,T)$ is seen to exhibit an electric field and temperature dependence (at ambient pressures) primarily determined by $\varepsilon^{\sigma,T}$. If we consider η^2 in the neighborhood of the critical electric field and critical temperature then we find

$$\lim_{\substack{E\to E_{cr} \\ T\to T_{cr}}} \eta^2(E,T) = 0$$

since $\varepsilon^{\sigma,T}$ becomes singular at the critical point. Whether or not this narrowing as a function of E and T is experimentally accessible is dependent upon the quantitative value of $\left[\frac{\delta_o'}{\Omega_o}\right]^2$.

It may be that $\left[\frac{\delta_o}{\Omega_o}\right]$ is so very small that this linewidth renormalization will occur only at the exact critical point. Preliminary experimental results have shown no pronounced electric field dependence to the DCP linewidth.

Since it is believed, for atmospheric pressure and E = 0, that the renormalization coefficient is $\eta^2 \simeq 1$, the DCP linewidth will be indistinguishable from the thermal diffusion mode linewidth. A discussion of the thermal diffusion mode linewidth is given in the following paragraphs.

C. Thermal Diffusion Mode Relaxation Time

The thermal diffusion mode relaxation time is given by the classical expression:

$$\frac{1}{\tau} = D_{th} q^2 \tag{21}$$

where the thermal diffusivity is

$$D_{th} = \frac{\lambda}{\rho C} \tag{22}$$

and the momentum transfer is

$$q = \frac{4\pi n}{\lambda_L} \sin \frac{\theta}{2} \tag{23}$$

λ - thermal conductivity
ρ - density
C - specific heat
n - index of refraction
λ_L - laser wavelength in medium
θ - scattering angle

Values used for the thermal conductivity and specific heat are given in Appendix B.

For 90° scattering at the laser wavelength $\lambda_L^\circ = 5145$ Å (in vacuum), the square of the momentum transfer is

$$q^2 = 6.71 \times 10^{10} \text{ cm}^{-2}$$

Table II catalogs the thermodynamic predictions for the thermal diffusivity D_{th}, thermal diffusion mode relaxation time τ, and dynamic central peak linewidth (FWHM), $\Delta\nu = \frac{1}{\pi\tau}$ as a function of temperature difference from the peak in the calorimetric anomaly in the ferroelectric phase. Figure 3 is a plot of $\Delta\nu$ as a function of T_p-T. The solid line is the thermodynamic prediction for $\Delta\nu$. The experimental points were plotted by matching the data point for T_c-T =0.028°K with the predicted linewidth and plotting the

Table II

T_p-T (^oK)	D_{th} $\frac{cm^2}{sec}$	τ ns	$\Delta\nu$ MHz
.203	$3.9X10^{-3}$	3.8	84
.183	3.7	4.0	80
.163	3.6	4.1	78
.143	3.5	4.3	74
.123	3.3	4.5	71
.103	3.2	4.7	68
.093	3.1	4.8	66
.083	3.0	4.9	65
.073	2.9	5.1	62
.063	2.8	5.2	61
.053	2.7	5.4	59
.043	2.6	5.6	57
.033	2.5	5.9	54
.023	2.4	6.2	51
.013	2.3	6.6	48
.003	2.0	7.5	42

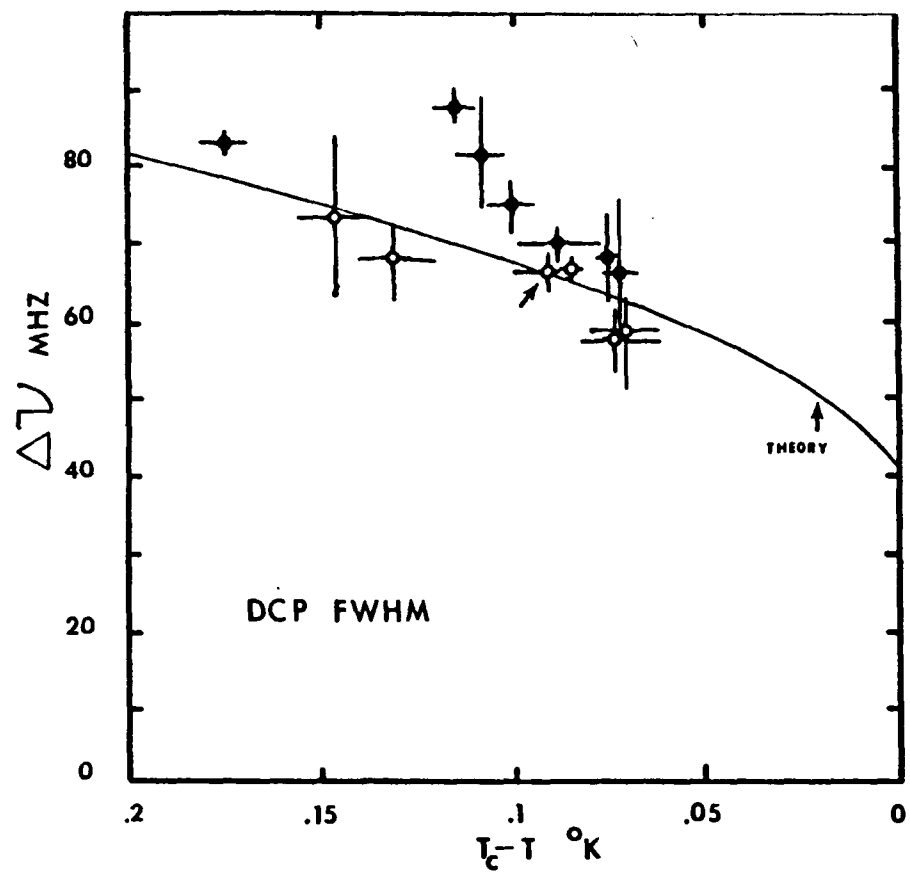

fig. VIII-3 Solid line shows thermal diffusion mode prediction for dynamic central peak linewidth ($\eta^2=1$) expressed by equations 16, 17, 21-23. Open and closed circles are the data points from fig. VII-5. The temperature of the data point indicated by the arrow has been shifted so that it agrees with prediction. All other points havebeen plotted relative to this point.

other data points relative to its temperature. The one data point at $T_c - T = 0.004°K$ which shows a large deviation from the predicted values (see Fig. VII-5) is not shown in Fig. 3. Notice that the linewidth is expected to narrow as T_c is approached from below, due to the anomaly in the specific heat. Since the measurements of Reese and May indicate that the anomaly in the dielectric constant occurs 0.1°K lower than the anomaly in the specific heat, it is difficult to pinpoint the exact transition temperature, as measured in the light scattering experiment, in Fig. 3. It is perhaps safe to say that T_c lies in the range $T_p - 0.1 \leq T_c \leq T_p$.

The predictions of eq. (21), as shown in Figure 3, yield excellent agreement with the experimental data when consideration is given to the difficulty in determining the exact transition temperature relative to the specific heat data.

IV. Conclusion

In conclusion, we have shown that the dynamic central peak that we have observed in ferroelectric KDP can be viewed as the low frequency structure of the ferroelectric soft mode induced by its coupling to the slowly relaxing thermal diffusion mode via the strongly temperature-dependent spontaneous polarization. This anlysis has succeeded in explaining the temperature dependence of the width and the temperature and electric field dependence of the intensity of this new feature.

IX. Conclusion

In this thesis, Brillouin and high resolution Rayleigh scattering measurements of the central peak in KDP have been presented. These experiments (along with those of other workers) have established the presence of two central peaks; a static central peak and a dynamic central peak. The static central peak exhibits no intrinsic linewidth and appears in both the paraelectric and ferroelectric phases within a few degrees of the transition temperature. Experimental evidence presented here (and by others) strongly suggest that this component is due to defect-induced inhomogeneous static distortions in the X_y shear strain. It has recently been shown that this central peak can be removed by suitable annealing and is therefore an extrinsic property of the crystal. An interesting aspect of the static central peak, reported here, is that the electric field dependence of it s intensity exhibits the Tricritical behavior of the first order transition via the isothermal elastic constant $C_{66}^{E,T}$.

A dynamic central peak has been observed in the ferroelectric phase of the shorted crystal and in both phases in the presence of an electric field. This central peak is interpretted as the low frequency structure of the ferroelectric soft mode induced by temperature fluctuations. Measurements of the temperature and electric field dependence of the dynamic central peak intensity have been presented here and agree well with the predictions of thermodynamic fluctuation theory. Linewidth measurements are in good agreement with predictions determined by

the thermal diffusivity. Restrictions on our scattering geometry have prevented us from verifying the q^2 linewidth dependence expressed by equation VIII-21. The linewidth renormalization, which is expected close to T_c, has not been seen and is believed to be inaccessible at atmospheric pressure due to the first order nature of the transition. However, application of hydrostatic pressure can drive the transition to become second order, in which case the linewidth renormalization should become evident. This would provide crucial verification of the coupled mode analysis. Further electric field measurements at atmospheric pressure should also be performed using annealed crystals so that the DCP linewidth can be more easily measured without interference from the SCP.

Appendix A

Temperature Rise and Thermal Gradients Induced by the Laser near T_c in KDP

I. Introduction

In this appendix I will consider the thermal effects of the laser beam as it passes through the KDP crystal. In particular, I am interested in determining the maximum temperature rise of the focal volume induced by the laser and obtaining a relation between the actual temperature of the focal volume and the temperature determined by the thermometer.

Since the quasielastic features appearing near T_c are severely temperature dependent, it is important to establish whether there exists any significant temperature gradients across the focal volume and thereby determine whether the experiment is probing a homogeneous volume element. Some of the results of these calculations will be compared to experiment.

The calculation proceeds essentially from the discussion by Lax.[105] An earlier calculation for the time dependent problem has been done by Gordon et al.[106] Their results, under appropriate simplifications, reduced to the results given here.

II. Formulation of the Problem

a. Thermodynamic Geometry.

Since the intent of this calculation is to obtain an order of magnitude estimate of the temperature distribution in the crystal and sample cell, I will set up the problem in a manner that fully exploits the cylindrical symmetry. The KDP crystal is represented by an infinite cylinder of radius r_0 and is surrounded by a bakelite housing of inner radius r_0 and outer radius r_b. The crystal and housing are immersed in a 2-methylbutane bath placed in a brass sample cell of radius r_c maintained at the bath temperature T_0. The laser beam passes down the axis of the crystal. A schematic diagram

of this configuration is given in figure 1. The platinum resistance thermometer is of cylindrical shape and 2 cm in length. Its center is taken to be a distance r_p from the optic axis.

b. Laser Beam as a Heat Source

The intensity profile of the laser beam can be expressed in cylindrical coordinates as:

$$I(r,z) = I_0 f(r,z) \tag{1}$$

where I_0 is the intensity amplitude and $f(r,z)$ is the intensity profile at z. The power of the laser beam is given by

$$P(z) = I_0 \int_0^{2\pi} d\varphi \int_0^{\infty} dr\, r\, f(r,z) \tag{2}$$

Heating of the crystal by the laser beam results from the absorption of energy by the crystal. This absorption is characterized by α, the attenuation constant of the laser beam in the crystal. The laser beam then constitutes a heat source whose energy per unit volume per second is given by

$$G(r,z) = \alpha e^{-\alpha z} I_0 f(r,z) \tag{3}$$

Since KDP is transparent, $\alpha z \ll 1$ and we have:

$$G(r,z) = \alpha I_0 f(r,z) \tag{4}$$

I then consider two approximations for $f(r,z)$:

(a) Rectangular intensity profile. In this case the laser beam, of diameter w_0, has a uniform intensity distribution. I can express f as:

$$f(r) = \begin{cases} 1 & r \le w_0/2 \\ 0 & r > w_0/2 \end{cases} \tag{5}$$

(b) Gaussian intensity profile. This approximation more accurately reflects the true situation. The intensity profile is given by:

$$f(r) = e^{-4r^2/w_0^2} \tag{6}$$

The intensity falls to e^{-1} of its maximum value at a radius $r = \frac{w_0}{2}$. These intensity profiles are shown in figure 2. The laser power for both profiles

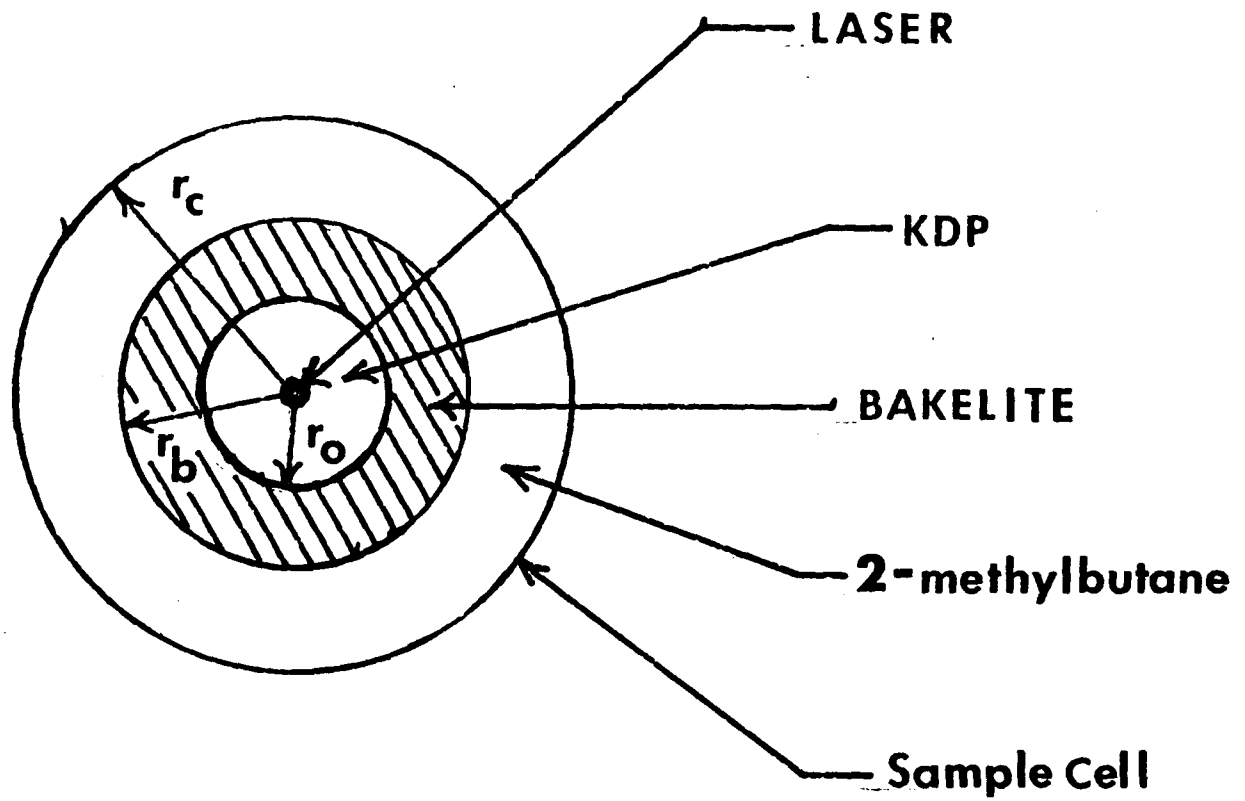

fig A-1 Model for laser heating calculation with cylindrical symmetry.

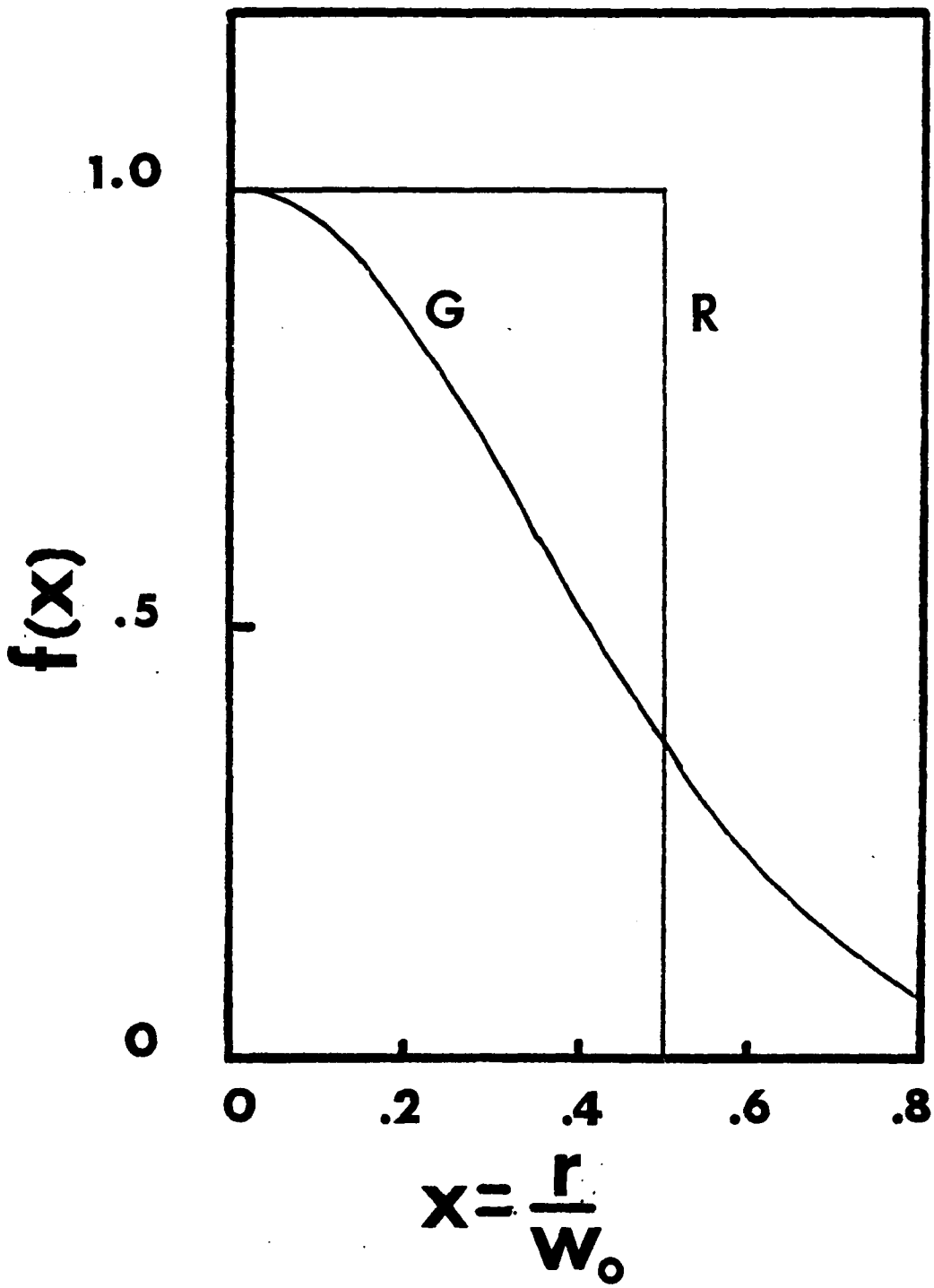

fig. A-2 Laser intensity profile along radial direction. R indicates rectangular profile and G indicates gaussian profile.

is found from (2) to be:

$$P = \frac{\pi}{4} I_0 w_0^2 \tag{7}$$

In the following, the rectangular profile will be denoted by R, and the Gaussian profile will be denoted by G.

c. Heat Equation

(1) Calculation of the Heat Flux $\underset{\sim}{J}$.

The temperature distribution is governed by the heat equation:

$$c \frac{\partial T}{\partial t} = -\nabla \cdot \underset{\sim}{J} + G \tag{8}$$

where

c - heat capacity

T - temperature

$\underset{\sim}{J}$ - heat flux

The heat flux $\underset{\sim}{J}$ is given by

$$\underset{\sim}{J} = -\lambda \nabla T \tag{9}$$

where λ is the thermal conductivity of the material in which the temperature gradient occurs. I am interested in the steady state solution, so $\frac{\partial T}{\partial t} = 0$. Hence, the equations for the heat flux $\underset{\sim}{J}$ and temperature T are:

$$\nabla \cdot \underset{\sim}{J} = G \tag{10}$$

$$\nabla^2 T = -\frac{1}{\lambda} G \tag{11}$$

In order to determine $\underset{\sim}{J}$, we can exploit the cylindrical symmetry of the problem and use the divergence theorem:

$$\int_V d^3r \, \nabla \cdot \underset{\sim}{J} = \int_S \underset{\sim}{J} \cdot d\underset{\sim}{S} \tag{12}$$

Hence,

$$\int_S \underset{\sim}{J} \cdot d\underset{\sim}{S} = \int_V d^3r \, G(r) \tag{13}$$

where G(r) is given by (3)

I then have the following solutions for the two cases:

(a) R:

$$\underset{\sim}{J} = \begin{cases} J_0 x \, \hat{x} & x \leq 1/2 \\ J_0 \frac{1}{4x} \hat{x} & x > 1/2 \end{cases} \tag{14}$$

(b) G:

$$\underset{\sim}{J} = J_0 \frac{1}{4x} \left[1 - e^{-4x^2} \right] \hat{x} \tag{15}$$

where I have introduced the dimensionless variable $x \equiv \frac{r}{w_0}$ and have $J_0 \equiv \frac{2\alpha P}{\pi w_0}$. Notice that in the limits $x \ll 1$ and $x \gg 1$ both expressions yield the same result for $\underset{\sim}{J}$. Plots for $\frac{|\underset{\sim}{J}|}{J}$ as a function of x for the two laser profiles are given in figure 3.

(2) Temperature Distribution T(x)

The temperature distribution can be found by integration of (9).

(a) Temperature profile. I would first like to establish the temperature profile in the crystal. Integration yields the following results:

$$(R) \qquad \frac{\Delta T}{\theta} = \begin{cases} -4x^2 & 0 \leq x \leq 1/2 \\ -\left[1 + 2 \ln(2x) \right] & 1/2 \leq x \leq x_0 \end{cases} \tag{16}$$

$$(G) \qquad \frac{\Delta T}{\theta} = -\mathrm{Ein}(4x^2) \tag{17}$$

where $\Delta T = T(x) - T(0)$

and

Ein(z) is a tabulated exponential integral given in Abramovitz and Stegun, Handbook of Mathematical Functions, Dover Publications, Inc., N.Y. p 228. Plots for both laser profiles are given in figure 4. From the plots one can see that the temperature gradient over the focal volume, for P = 100 mW, is

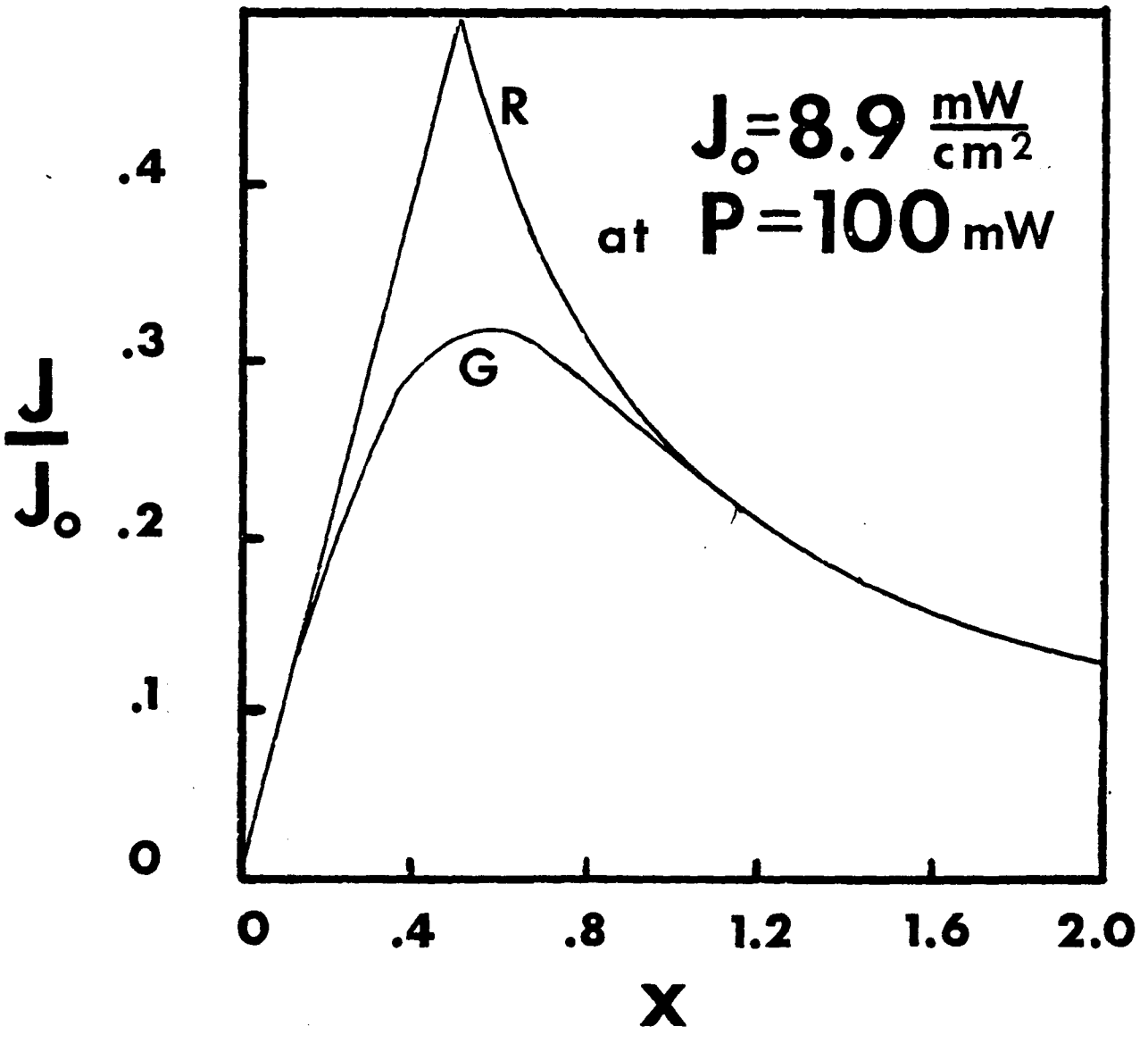

Fig. A-3 Heat flux for R and G laser profiles as a function of radial distance from optic axes. For a laser power of P = 100mW and a Henuation coefficient x for KDP, I estimate that Jo = $8.9 \frac{mW}{cm^2}$

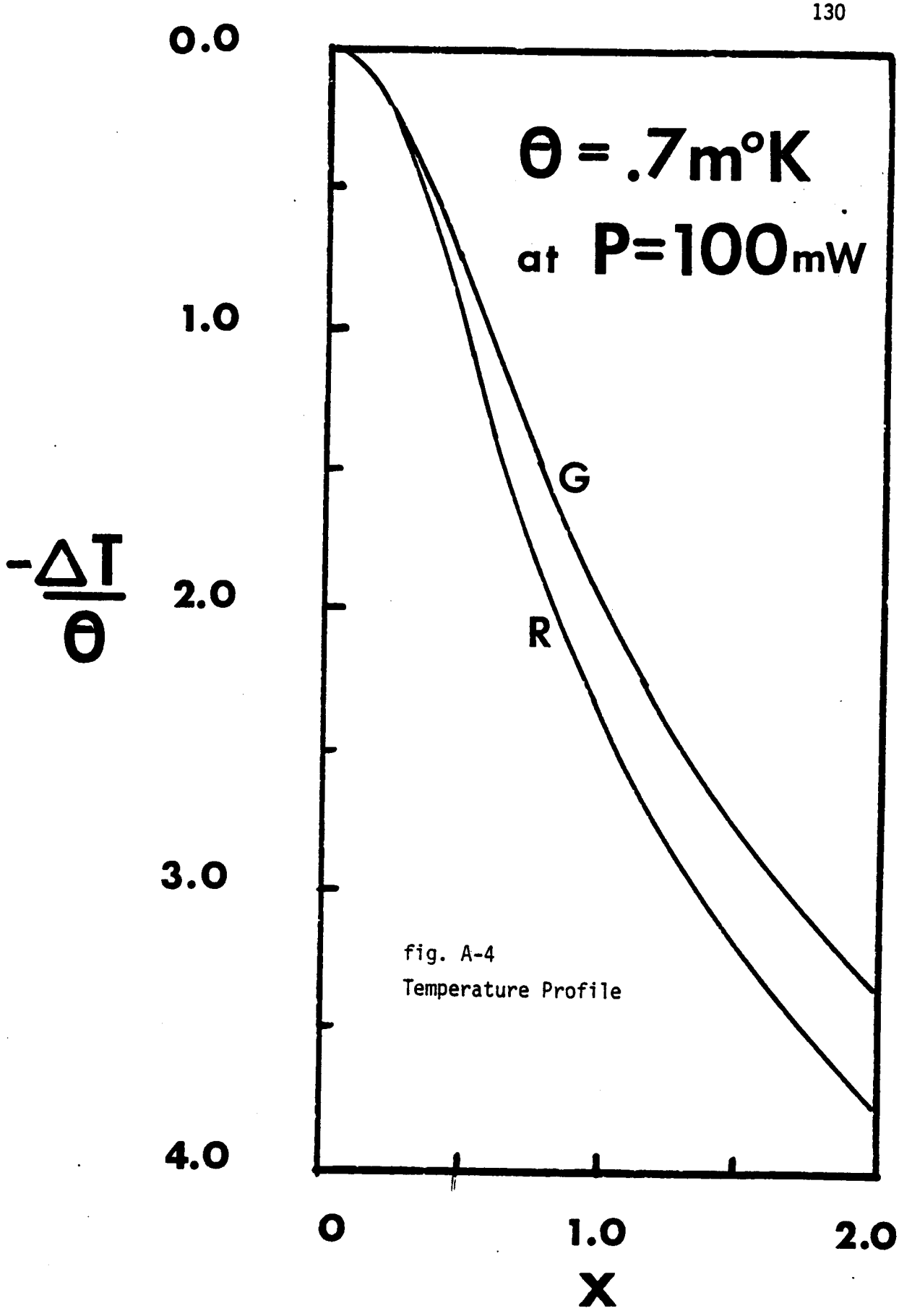

fig. A-4
Temperature Profile

less than $1m^0$ K. (Numerical values for the parameters of the calculation are given at the end of this section).

(b) Maximum temperature rise of the focal volume. The maximum temperature occuring on the optic axis as a result of the laser beam can be found by integrating (9) from the origin to the sample cell wall. The sample cell wall is taken to be at the bath temperatire T_0, and λ_1, λ_2, and λ_3 are the thermal conductivities of the KDP, bakelite, and 2-methylbutane respectively. Denoting the maximum temperature rise by $\theta_0 = T(0) - T_0$ I find

$$\theta_0 = \begin{cases} \dfrac{\alpha P}{2\pi\beta_R} & R \\ \dfrac{\alpha P}{2\pi\beta_G} & G \end{cases} \qquad (18)$$

where

$$\frac{1}{\beta_R} = \frac{1}{\lambda_1}\left(\frac{1}{2} + \ln(2x_0)\right) + \frac{1}{\lambda_2}\ln\left(\frac{x_b}{x_0}\right) + \frac{1}{\lambda_3}\ln\left(\frac{x_c}{x_b}\right)$$

$$\frac{1}{\beta_G} = \frac{1}{\lambda_1}Ein(4x_0^2) + \frac{1}{\lambda_2}\left[Ein(4x_b^2) - Ein(4x_0^2)\right] + \frac{1}{\lambda_3}\left[Ein(4x_c^2) - Ein(4x_b^2)\right]$$

Evaluating this expression I find $\beta_R = 1.410 \frac{mW}{cm\text{-}oK}$, $\beta_G = .719 \frac{mW}{cm\text{-}°K}$

and

$$\Theta_o = \begin{cases} 16\ m°K & R \\ 31\ m°K & G \end{cases}$$

where $T(0) = T_o + \theta_o$

(c) Relation between T_c and temperature measured by thermometer. A more important question to be addressed is: Given the laser power during the experiment, what is the relation between the actual transtion temperature T_c of the focal volume and the temperature, T_c^{PRT}, measured by the thermometer? To answer this question I integrate (9) from the origin to x_p where the thermometer is located. Integration reveals the following relations:

$$T_c^{PRT} = T_c - m_R P \qquad (R) \qquad (19a)$$

$$T_c^{PRT} = T_c - m_G P \qquad (G) \qquad (19b)$$

I find that

$$m_R = .25 \frac{m°K}{mW} \qquad m_G = .50 \frac{m°K}{mW} \qquad (20)$$

This result is compared to experiment. The crystal was cooled down through its transition temperature while observing the Brillouin components. T_c^{PRT} was taken to be the measured temperature at which the C_{66} elastic constant softened to zero. The temperature was measured by the platinum resistance thermometer. This was repeated for several different laser powers. A plot of T_c^{PRT} vs P was made and is shown in fig. A-5.

The experimental result of $m_{exp} = .91 \frac{m°K}{mW}$ compares reasonably well

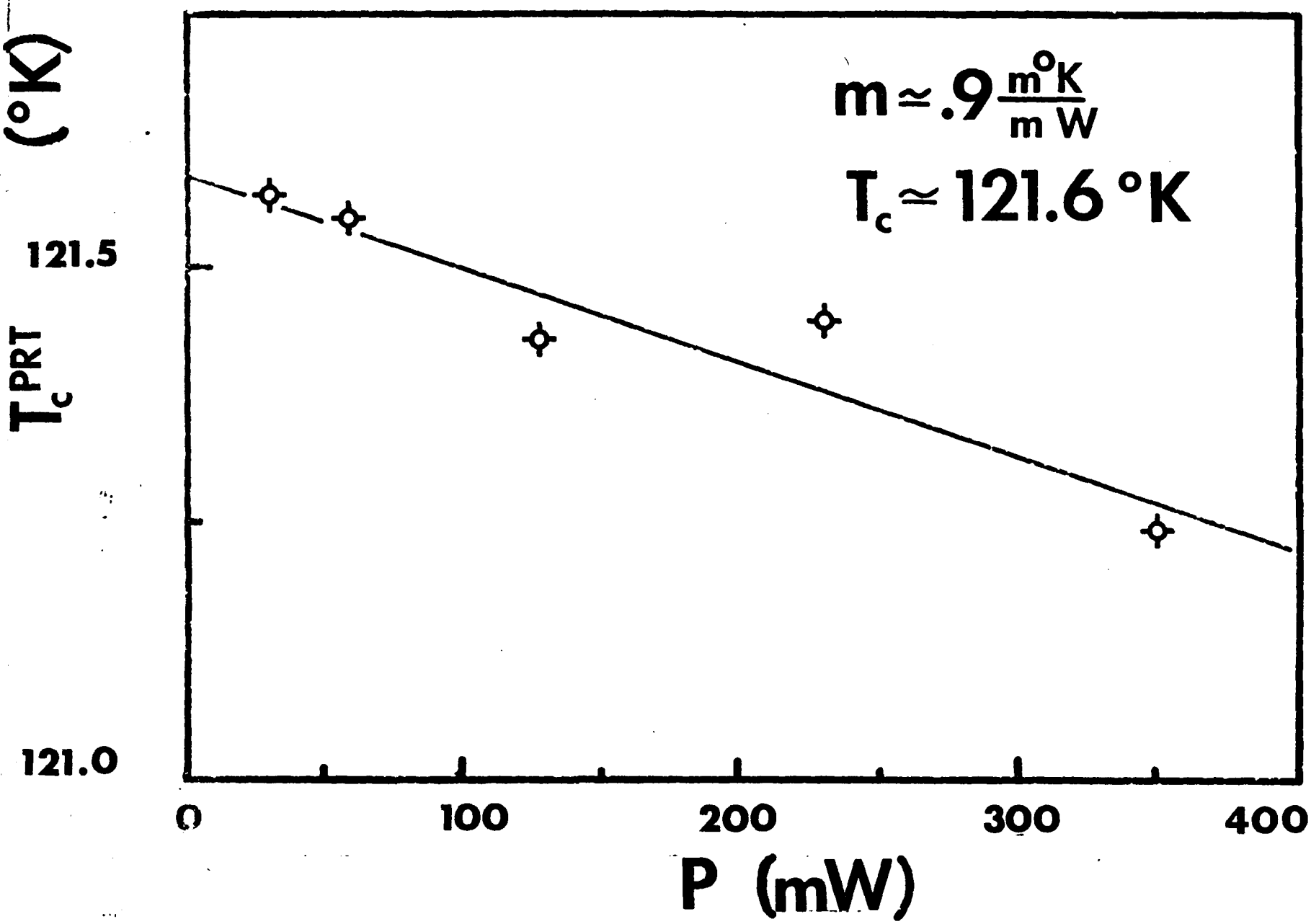

fig. A-5 Transition temperature measured by the PRT as a function of incident laser power. The transition was detected by monitoring the motion of the Brillouin components.

with the theoretical predictions of equations (19) and (20) (m_R and m_G), in view of the gross approximations made in the calculation. As expected, the Gaussian laser profile yields better agreement. Hence, the calculation provides a reasonable estimate of laser induced temperature gardients in the focal volume, showing them to be less than 1m°K for laser power of P = 100mW.

(d) Parameters for Laser Heating Calculation

(1) Sample Cell Geometry

The calculation was done for the following sample cell geometry (see fig. 1):

beam dia. w_o = .01 cm

r_o = .50 cm	x_o = 50
r_b = 1.0 cm	x_b = 100
r_c = 1.2 cm	x_c = 120
r_p = 2.0 cm	x_p = 200

(2) Attentuation coefficient α.

The attenuation coefficient α was estimated from the transmission data taken by Cleveland Crystals. The transmission data was corrected for reflection losses at the surface. I estimated that

$$\alpha = 1.4 \times 10^{-3} \text{ cm}^{-1}$$

(3) Thermal Conductivity λ.

(a) KDP. The thermal conductivity of KDP near T_c is taken from the data of Ysutaka Suemune.[111] The value used is $\lambda_1 = 16 \frac{\text{mW}}{\text{cm-°K}}$.

(b) Bakelite. The room temperature thermal conductivity of bakelite (paper base phenolic) was obtained from Almac Plastics Inc., Long Island City, New York. $\lambda_2 = 2.93 \frac{\text{mW}}{\text{cm-°K}}$

(c) 2-methylbutane. The thermal conductivity of 2-methylbutane at 0°C was found to be $\lambda_3 = 1.19 \frac{mK}{cm\text{-}°K}$.
(Tables on the Thermophysical Properties of Liquids and Gases, N.B Varguftik, Hemisphere Publishing Corporation, Washington-London 1975, p.261.)

(4) Constants of the calculation. The following constants, appearing in the calculation are for a laser power of P = 100 mW and the above parameters.

Heat Flux: $J_o = \frac{2\alpha P}{\pi w_o} = 8.9 \frac{mW}{cm^2}$

Temp. change: $\theta = \frac{\alpha P}{4\pi\lambda} = .7\ m°K$

Appendix B Thermodynamic Parameters

In this appendix I have collected values for the physical quantities used in the dynamic central peak calculations of Chapter VIII.

(1) Index of Refraction

Measurements of the ordinary and extraordinary index of refraction (for KDP) and their temperature dependence were made by M. Yamazaki and T. Ogawa [98] for several wavelengths over the temperature range of 100 to 300 K. The results of their measurements, taken from reference (107), are shown in figure 1. From this data, I have estimated the 'normal' contribution to the temperature dependence of the optical dielectric constant ($\varepsilon = n^2$) to be $\frac{d\varepsilon}{dT} \simeq 4 \times 10^{-4}\ ^\circ K^{-1}$ in the ferroelectric phase. I have assumed that this quantity is essentially constant over the temperature range, neglecting possible anomolous contributions due to an anomaly in the thermal expansion coefficient near T_c.[108]

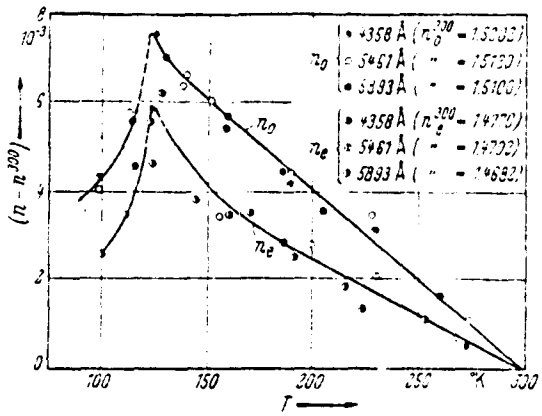

... KH_2PO_4 (KDP). $(n - n^{300})$ vs. T. n^{300}: refractive index at 300 °K [66 Y].

(2) Electrooptic Coefficient $\rho_{63}^{x,T}$

The isothermal electrooptic coefficient at constant strain, defined by $\rho_{63}^{x,T} = -\frac{1}{\varepsilon_0^2}\left(\frac{\delta \varepsilon^{xy}}{\delta P_3}\right)_{x,T}$ is reported in ref. (109) to be $\rho_{63}^{T} = -20.9 \times 10^{-8}\ \frac{cm^2}{esu}$.

(3) Elastooptic Coefficient p_{66}^{P}

The isothermal elastooptic coefficient (or Pockels coefficient) was

measured by Brody and Cummins. [101] They measured the intensity of the X_y shear mode Brillouin components near the phase transition and observed an anomaly in the $p_{66}^{E=0}$ elastooptic coefficient. p_{66}^{P} is defined as:

$$p_{66}^{P,T} = -\frac{1}{\varepsilon_0^2}\left(\frac{\partial \varepsilon^{xy}}{\partial X_6}\right)_{P,T}$$

From their data they deduce the value; $p_{66}^{P} = -0.0345$.

4) Heat Capacity

High resolution measurements of the heat capacity in the vicinity of the transition were reported by Reese and May. [99] Their measurements were made on polycrystalline samples. (Measurements on single crystals were reported in a later publication which included heat capacity measurements in the presence of an applied electric field. [110]) The heat capacity measurements, taken from reference (99) are shown in fig. 2 and tabulated in table I. Measurements of the static dielectric constant were also made which indicate that the temperature of the dielectric anomaly occurs about 0.1°K below the temperature of the calorimeter anomaly which occurs at T_p. This difference was not observed in the single crystal samples.

5) Thermal Conductivity

Thermal conductivity (λ) measurements were made by Y. Suemune. [111] His results for KDP in the vicinity of the transition temperature are reproduced in figure 3. In these measurements the temperature gradients vary from 0.2°K/cm to 3.0 K.cm over a thermocouple separation of about 0.4 to 0.6 cm. Therefore, these measurements are unable to resolve any anomalous behavior in λ with 0.1°K of the transition where the DCP appears. As the transition is approached from above, λ is seen to decrease in manner de-

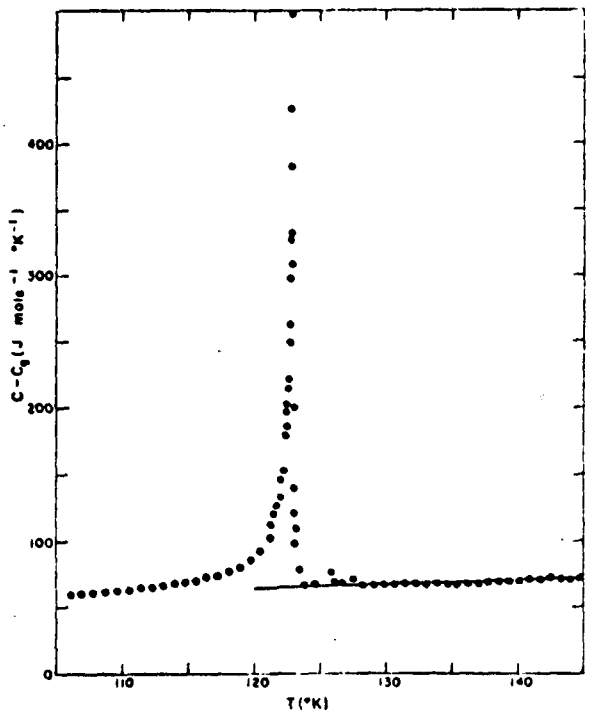

(a)

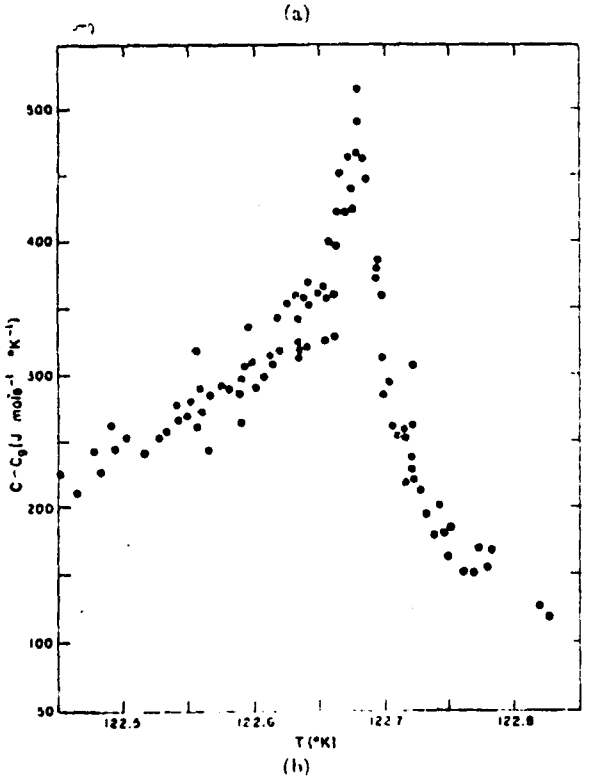

(b)

The heat capacity of KDP. With the exception of the points in the immediate neighborhood of the transition the points shown in Fig. 2(a) were taken with temperature intervals of approximately 1°K. The points shown in Fig. 2(b) were taken with smaller intervals, typically between 0.05°K and 0.01°K. The points shown in Fig. 2(a) were taken from Series I, those shown in Fig. 2(b) were taken from both Series I and Series III. Note the change in origin between Fig. 2(a) and Fig. 2(b). The solid line in Fig. 2(a) shows the expression chosen to represent C_a, the lattice heat capacity.

TABLE I. A summary of the experimental data near the transition is given by averaging the data in temperature bins of varying sizes. The average temperature and average heat capacity for the points falling within the bin and the rms deviation of the data within each bin are given. The data from Series I and Series III have been treated separately.

T (°K)	C (J/mole °K)	Root mean square deviation (J/mole °K)
	SERIES I	
120.459	101	1.4
120.944	110	0.7
121.211	112	1.6
121.554	123	0.9
121.730	133	3.6
121.836	130	2.0
121.934	142	3.0
122.044	151	3.1
122.140	163	7.3
122.230	176	4.0
122.333	191	1.7
122.403	214	5.0
122.457	228	5.6
122.508	255	3.5
122.546	273	4.6
122.570	269	12.6
122.592	290	7.5
122.615	318	3.3
122.638	334	11.1
122.656	336	7.5
122.676	432	8.1
122.683	505	10.2
122.695	371	5.8
122.719	243	8.3
122.747	191	6.1
122.776	174	9.2
122.817	133	4.5
122.859	111	3.1
122.909	102	4.7
122.963	92.0	2.9
123.035	87.8	4.5
123.115	82.3	0.1
123.236	73.8	2.1
123.343	75.0	2.1
123.433	77.4	2.0
123.687	74.5	0.3
124.199	80.9	8.2
	SERIES III	
122.365	195	4.4
122.477	229	7.9
122.533	260	6.4
122.558	283	9.6
122.584	291	5.1
122.594	311	6.2
122.604	281	12.4
122.617	340	7.6
122.625	350	...
122.634	350	12.6
122.644	364	2.9
122.654	392	15.3
122.662	394	17.5
122.675	458	8.9
122.684	450	6.8
122.692	375	7.8
122.698	296	11.0
122.704	264	14.2
122.714	233	10.4
122.723	230	14.4
122.738	182	4.3
122.758	155	3.7
122.825	118	...

fig 2

termined by the temperature dependence of the specific heat. In going through the transition, λ sharply increases due to the reduction in phonon-phonon scattering resulting from the hydrogen ordering. Consideration of the first three data points in the ferroelectric phase yields an estimate for the slope of $\Delta\lambda/\Delta T \simeq 0.75 \left(\frac{mW}{K\text{-}cm}/^{o}K\right)$ for $0 < T_c \leq T - 4°K$. Hence λ is estimated to change by $0.08 \frac{mW}{°K\text{-}cm}$ over the temperature range of the DCP, or by approximately 0.5% (assuming no anomalous behavior at T_c.) Therefore, the value of λ , for the DCP temperature range, is taken to be essentially constant at $\lambda = \lambda_{min} = 15 , 6 \frac{mW}{°K\text{-}cm}$.

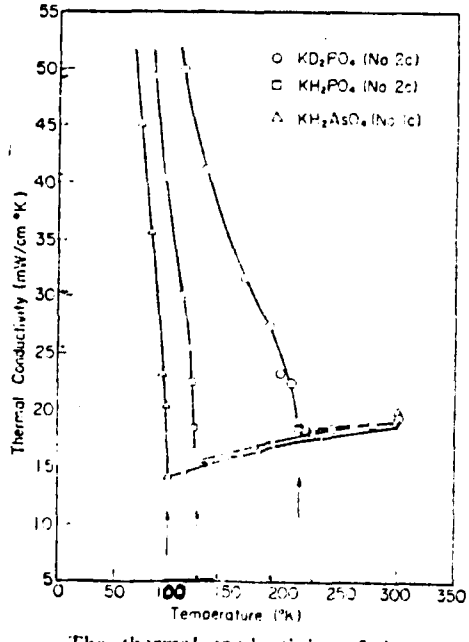

The thermal conductivity of the crystals KH_2PO_4 (No. 2c), KD_2PO_4 (No. 2c) and KH_2AsO_4 (No. 1c) in the vicinity of the Curie temperatures at which the order-disorder of hydrogen atoms occurs. Abrupt changes appear at the transitions. The gradual decrease persists down to about 100°K for KH_2AsO_4. The arrows indicate the Curie temperatures, respectively.

fig B-3

FOOTNOTES

1) T. Riste, E. J. Samuelson, K. Otnes, and J. Feder, Solid State Commun. 9, 1455 (1971)

2) T. Riste, E.J. Samuelson, and K. Otnes in Structural Phase Transition and SoftModes, edited by E.J. Samuelson, E. Anderson, and J. Feder (Universitetsfurlaget, Oslo, 1971), 395

3) N. Lagakos and H.Z. Cummins, Phys. Rev. B 10, 1063 (1974)

4) N. Lagakos, Ph.D. thesis (New York University, 1975, unpublished)

5) M. D. Mermelstein and H.Z. Cummins, Phys. Rev. B 16, 2177 (1977)

6) R. Blinc, Ferroelectrics, 19, 1 (1978)

7) G. Shirane and J.D. Axe, Phys Rev. Lett. 27, 1803 (1971)

8) S. M. Shapiro, J. D. Axe, and G. Shirane, Phys. Rev. B 6, 4332 (1972)

9) J. Topler, B. Alefeld, and A. Heidemann, J. Phys. C: Solid State Physics, 10, 635 (1977)

10) J.D. Axe and G. Shirane, Phys. Rev. B 8, 1965 (1973)

11) R. A. Cowley, J.D. Axe, and M. Iizumi, Phys. Rev. Lett. 36, 806 (1976)

12) B. I. Halperin and C.M. Varma, Phys. Rev. B 14, 4030, (1976)

13) J. B. Hastings, S. M. Shapiro, and B.C. Frazer, Phys. Rev. Lett. 40, 237 (1978)

14) E. F. Steigmeier, G. Harbeke, and R. K. Wehner, in reference (2) 409

15) E. F. Steigmeier, H. Auderset and G. Harbeke, Solid State Commun. 12, 1077, (1973)

16) E.F. Steigmeier, H. Auderset and G. Harbeke, in Anharmonic Lattices, Structural Transitions and Melting, edited by T. Riste (Nordhoff, Leiden, 1974) 153

17) K. B. Lyons and P. A. Fleury, "Phonon Interactions and the Dynamic Central Peak in $SrTiO_3$, Near the Structural Phase Transition," preprint 1977

18) P.A. Fleury and K.B. Lyons, in Proceedings of the International Conference on Lattice Dynamics, edited by M. Balkanski (Flammarion Sciences, Paris, 1977) 731

19) K.B. Lyons and P. A. Fleury, Phys. Rev. Lett.. 37, 161 (1976)

20) D. J. Lockwood, J.W. Arthur, W. Taylor, and T. J. Hosea, Solid State Commun. 20, 703 (1976)

21) P.A. Fleury and K. B. Lyons, Phys. Rev. Lett. 37, 1088 (1976)

22) K. B. Lyons and P. A. Fleury, "Light Scattering Investigations of the Ferroelectric Transition in Lead Germanate" preprint 1977

23) R.A. Cowley, J. Phys. Soc. Jap. Suppl. 28, 239 (1970)

24) L.N. Durvasula and R.W. Gammon, Phys. Rev. Lett. 38, 1081 (1977)

25) E. Courtens, Phys. Rev. Lett. 41, 1171 (1978)

26) T. Tagi, H. Tanaka, and I. Tatsuzaki, Phys. Rev. Lett. 38, 609. (1977)

27) H. Tanaka T. Yagi, and I. Tatsuzaki, J. of the Phys. Soc. of Jap. 44, 1257 (1978)

28) R. Blinc, P. Cevc, and M. Schara, Phys. Rev. 159, 411 (1967)

29) K.A. Muller, W. Berlinger, C. H. West, and P. Heller, Phys. Rev. Lett. 32, 160 (1974)

30) K.A. Muller in reference (2), 85

31) J. Slak, R. Blinc, V. Tutar and S. Zumer, Ferroelectrics 12, 281, (1976)

32) R. Blinc, Ferroelectrics 19, 1 (1978)

33) R. Blinc and J. L. Bjorkstam, Phys. Rev. Lett. 23, 788 (1969)

34) G. J. Adriaenssens, and J.L. Bjorkstam, Phys. Stat. Solids A18, 129 (1973)

35) K.A. Muller, N.S. Dalal, and W. Berlinger, Phys. Rev. Lett. 36, 1504 (1976)

36) K. A. Muller and W. Berlinger, Phys Rev. Lett. 37 37, 916 (1976)

37) R. Blinc, Ferroelectrics, 16, 33 (1977)

38) C.N.W. Darlington, W. J. Fitzgerald and D.A. O'Conner, Phys. Lett. 54A, 35 (1975)

39) C.N.W. Darlington and D.A. O'Conner, J. Phys. C. 9, 3561 (1976)

40) K. Hanisch and M. Drosg, Phys. Lett. 58A, 415 (1976)

41) C.N.W. Darlington and D.A. O'Conner in reference (18) 750

42) W. Rehwald, Adv. in Phys. 22, 721 (1973)

43) E. M. Alexander and R.W. Gammon, Ferroelectrics 17, no. 1-2, 439 (1977)

44) O. J. Adrianenssens and J. L. Bjorkstam, Phys Static Solids, A18 129, (1973)

45) N.E. Tornberg and R.P. Lowndes, J. Phys. C: Solid State Phys. 10, L549 (1977)

46) A. Widom, N.E. Tornberg, and R.P. Lowndes, J. Phys. C: Solid State Phys. 11, L433 (1978)

47) V. T. Hochli, H. E. Weibel, and L. A. Boatner, Phys. Rev. Lett. 41, 1410 (1978)

48) C. W. Garland, and N. B. Novotny, Phys. Rev. 177, 971 (1969)

49) G. J. Coombs and R. A. Cowley, J. Phys C6, 121 (1973)

50) R. A. Cowley and G.J. Coombs, J. Phys C6, 143 (1973)

51) F. Schwabl, Phys. Rev. Lett. 28, 500 (1972)

52) F. Schwabl, Solid State Comm. 13, 181 (1973)

53) F. Schwabl, in reference (16) 87

54) C.P.Enz., Phys. Rev. B 6, 4695 (1972)

55) R. Silberglitt, Solid State Comm. 11, 247 (1972)

56) I. Ohnari and S. Takada, "Central Peak and Thermal Diffusion Mode near Structural Phase Transition-Hydrodynamic Approach" preprint 1978

57) J. Feder, Solid State Comm. 9, 2021 (1971)

58) P. Heller, Int. J. Magnetism 1, 53 (1971)

59) J. A. Krumhansl and J. R. Schrieffer, Phys. Rev. B. 11, 3535 (1975)

60) S. Aubry, J. of Chem. Phys. 62, 3217 (1974)

61) T. R. Koehler, A. R. Bishop, J. A. Krumhansl, and J. R. Schrieffer, Solid State Comm. 17, 1515 (1975)

62) T. Schneider and E. Stoll, Phys Rev. Lett. 31, 1254 (1973)

63) R. Blinc, B. Zeks, and R. A. Tahin-Kheli, Phys. Rev. B18, 338 (1978)

64) J. D. Axe, S.M. Shapiro, G. Shirane, and T. Riste, in reference (16) 23

65) A. P. Levanyuk, V.V. Ospipov, and A.A. Sobyanin, in Theory of Light Scattering in Condensed Matter, edited by B. Bendow, J.L. Birman, and V. M. Arganovick (Plenum Press, New York, 1976) 628

66) H. Schmidt and F. Schwabl, Phys. Lett. 61A, 476 (1977)

67) H. Schmidt and F. Schwabl, in reference (18) 748

68) K.H. Hock and H. Thomas, Phys. B27, 267 (1977)

69) E. Courtens, Phys. Rev. Lett. 39, 561 (1977)

70) E. Courtens, Phys. Rev. Lett. 37, 1584 (1976)

71) L. D. Landau and E. M. Litshitz, Statistical Physics (Addison-Wesley, Reading, Mass. 1958) 430

72) A.F. Devonshire, Advances Physics 3, 86 (1954)

73) J. W. Benepe, and W. Reese, Phys. Rev. B3, 3032 (1971)

74) F. Jona and G. Shirane, Ferroelectric Crystals (The MacMillan Co., New York, 1962) Chapter III

75) J. West, Z. Krist, 74, 306 (1930)

76) J. C. Slater, J. of Chem. Phys. 9, 16, (1941)

77) H. B. Silsbee, E. A. Mehling, and V. H. Schmidt, Phys. Rev. 133 A165, (1964)

78) R. Blinc, J. Phys. Chem. Solids, 13, 204, (1959)

79) P.G. deGennes, Solid State Comm. 1 , 132, (1963)

80) R. Brout, K.A. Muller, and H. Thomas, Solid State Comm. 4, 507 (1966)

81) K.K. Kobayashi, J. of the Phys. Soc. of Jap. 24, 497 (1968)

82) W. Cochran, Adv. In Physs. 10, 401 (1961)

83) S. Takada, I. Ohnari, H, Kumosawa, and Y. Ohmura, Prog. of Theo. Phys., 53, 936 (1975)

84) E. M. Brody and H.Z. Cummins, Phys. Rev. B 9, 179 (1974)

85) T. Mitsui, I. Tatsuzaki, and E. Nakamura, An Introduction to the Physics of Ferroelectrics, (Gordon and Breach Science Publishers, 1976) 74

86) B. J. Berne and R. Pecora, Dynamic Light Scattering (John Wiley and Sons Inc., 1976)

87) Vallade, Phys. Rev. B. 12, 3755 (1975)

88) Stukov, Korzheuv, Baddur, and Koptsik, Sov. Phys. Solid State, 13, 1569 (1972)

89) E. V. Sidnenko, V.V. Gladkii, Sov. Phys. Cryst. 18, 83 (1973)

90) M. W. Dowley, "Single Frequency Operation of Ion Lasers," (Coherent Radiation Technical Bulletin, 106, 1971)

91) J. P. Hohimer, R. C. Kelly, and F. K. Tittel, Applied Optics 11, 626 (1972)

92) E. M. Brody, Ph. D. Thesis, (The John Hopkins University, 1969) unpublished

93) M. Born and E. Wolf, Principles of Optics (Pergamon Press, 1970) 327

94) R. L. Reese, I. J. Fritz, and H. Z. Cummins, Phys. Rev. B 7, 4165 (1973)

95) A. B. Western, A. G. Baker, R. J. Pollina, and V. H. Schmidt, Ferroelectrics 17, 333 (1977)

96) H. Z. Cummins, Ferrolectrics 16, 23 (1977)

97) H. W. Willemsen, R. L. Armstrong, and P.P.M. Meincke, Phys. Rev. B, 14, 3644 (1976)

98) M. Yamazaki and T. Ogawa, J. Opt: Soc. Am. 56, 1407 (1966)

99) W. Reese and L. F. May. Phys. Rev. 162, 510 (1967)

100) H. Z. Cummins and P. E. Schoen, in Laser Handbook, edited by F. T. Arechi and E. O. Schulzdubois (North Holland Pub. Amst.)

101) E. M. Brody and H. Z. Cummins, Phys. Rev. Lett. 23, 1039 (1969)

102) V. H. Schmidt, A. B. Western, and A. G. Baker, Phys. Rev. Lett. 37, 839, (1976)

103) Bastie, Vallade, Vettier, and Zeyer, Phys. Rev. Lett. 40, 337, (1978)

104) A. B. Western, A. G. Baker, C. R. Bacon, V. H. Schmidt, "Pressure Induced Tri-critica Point in the Ferroelectric Phase Transition of KH_2PO_4", preprint 1978

105) M. Lax, J. of Applied Physics, 48, 3919 (1977)

106) J. P. Gordon, R.C.C. Leite, R. S. Moore, S. P. S. Porto, and J. R. Whinnery, Journal of Applied Physics, 36, 3 (1965)

107) Landolt-Bornstein, Ferro and Antiferroelectric Substances, edited by X. Hellwege (Springer-Verlag, Berlin, 1969) Group 3, Vol.3 1969, fig 1155, p. 428

108) ibib. fig. 1109, p. 419

109) ibid. Group I. Volume 1, 1960 p. 143

110) W. Reese. Phys. Rev., 181, 905 (1969)

111) Y, Suemune, J. of the Phys. Soc. of Jap., 22, 735 (1967)